MPHIL

Applications and Limitations of Infrared Thermography in Turbine Cooling Visualisation

Gribanov, Ilya

Award date:
2014

Awarding institution:
University of Bath

Applications and Limitations of Infrared Thermography in Turbine Cooling Visualisation

Volume 1 of 1

Ilya Gribanov

A thesis submitted for the degree of Master of Philosophy

University of Bath

Department of Mechanical Engineering

March 2014

[page intentionally left blank]

Table of Contents

Acknowledgements

The author would like to acknowledge and thank the following groups and individuals for help and support during this study:

University of Bath Technicians Vijay Rajput and Colin Brain for the help with setting-up of the data acquisition equipment and design of data acquisition software. Post-doc Simon Pickering for designing the frame-grabbing program for the IR camera and helping with code preparation to open the raw IR files in MATLAB. University academic, administrative and directive staff for the continuous support and guidance provided to me both on the technical aspect of this thesis and overall progress guidance. Dr Stuart MacGregor for his support and guidance leading to development and completion of this work. Last, but not least – the author's family for their continuous all-round support during all stages of this work.

Abstract

Fierce international competition for efficient power plants and vehicle propulsion systems has fuelled evolution of gas turbines over the last eight decades of production. Power output can be increased with Turbine Entry Temperature (TET), which can typically be 500K higher than the melting point of turbine components. Safe engine operation in such extreme conditions is partly ensured by coating turbine components with a film of coolant air. An additional 1% in coolant air flow can raise TET by 100K at a 1% penalty in engine efficiency. Determining coolant quantities for optimum cooling is therefore key to maximising engine thrust, efficiency, and component life.

Experiments conducted on models at engine-representative conditions can aid the development of more efficient cooling methods, in addition to the validation of Computational Fluid Dynamic modelling codes. Thermal visualisation techniques will also aid in this assessment (e.g. Thermochromic Liquid Crystals, or Infrared Thermography).

The focus of this study is the assessment of applications and limitations of Infrared Thermography in turbine cooling flow visualisation. A model of a turbine blade leading edge with showerhead film cooling has been constructed and operated at an engine-representative Reynolds number in a low-speed wind tunnel. The coolant gas has been pre-heated prior to ejection and an Infrared camera was used to acquire coolant jet thermal imprints over the model surface in order to assess cooling effectiveness for different Blowing Ratio values. A perpendicular fine nylon mesh was used to capture coolant plumes at different circumferential locations above the cylinder surface to assess the extent of jet lift-off and interaction with cold mainstream flow. MATLAB software was used to develop camera calibration and data processing codes. The results have been used to assess the experimental technique for accuracy and consistency, as well as ability to make accurate heat transfer, or cooling effectiveness measurements.

Nomenclature

B	Blue light component
C_p	Pressure Coefficient
d	Cylinder diameter
G	Green light component
h	Hue
I	Intensity
p	Pressure
R	Red light component
Re	Reynolds number
S	Saturation
T	Temperature
T_{aw}	Adiabatic wall temperature
T_B	Temperature of the visualised body
T_C	Internal camera case temperature
T_{mesh}	Temperature measured on the mesh

Greek Symbols

ϵ	Directional emissivity
η_{aw}	Adiabatic wall cooling effectiveness
η_{gas}	Gas effectiveness
θ	Viewing angle
μ	Dynamic viscosity
v	Kinematic flow velocity
ρ	Density
ϕ	Angular circumferential location measured from SL

Subscripts

o	Total, stagnation conditions
m	Mainstream gas
c	Coolant gas
s	Surface condition

Abbreviations

BL	Boundary Layer
BR	Blowing Ratio
$CAWE$	Calculated Adiabatic Wall Effectiveness
CC	Combustion chamber
CCD	Charge-coupled device
CFD	Computational Fluid Dynamics
CGE	Calculated Gas Effectiveness
EMP	Electron-microscope photograph
HP	High Pressure
HT	Heat Transfer
IR	Infrared
IRI	Infrared Intensity
IRT	Infrared Thermography
LP	Low pressure
LPT	Low pressure turbine
MFR	Momentum Flux Ratio
$NETD$	Noise Equivalent Temperature Difference
NGV	Nozzle guide vane
PSP	Pressure Sensitive Paint
RGB	Red-green-blue additive colour model
SL	Stagnation Line
SP	Separation Point
TET	Turbine Entry Temperature
TLC	Thermochromic Liquid Crystal
$2D$	Two-dimensional
$3D$	Three-dimensional

List of Tables

Table of Figures

1 Introduction

In this introductory chapter the background and historical development of gas turbines will be outlined. It will highlight the need for efficient turbine blade cooling, which forms the motivation for this work – analysis of limitations and applications of Infrared Thermography in turbine cooling visualisation. Such analysis is necessary to assess the current thermography technologies and design an improved visualisation technique that could aid development of enhanced turbine cooling systems.

1.1 Background

In 1930 Sir Frank Whittle (figure 1-1) has patented his “Improvements relating to the propulsion of aircraft and other vehicles”. These registered ideas led to production of the first jet engine and a beginning of a new era in for propulsion of vehicles. Driven by the military arms race between the world’s most powerful nations, as well as fierce commercial competition between engine manufacturers, the jet engine has evolved to suit a wide range of vehicles over the last 80 years of production.

Figure 1-1 - Sir Frank Whittle 1907-1996

The jet engine, or a gas turbine may come in many variations (e.g. turbojet, turbofan, turboshaft and turboprop). A modern gas turbine is the most

common propulsion unit for airborne vehicles. In addition to this it has been widely used to power marine, submarine and even some road vehicles. They are also used in the production of electricity in power generation plants, as well as stationary power units on oilrigs and gas platforms.

1.2 Operating Principles of the Gas Turbine

A simple gas turbine has an air compressor, which draws large quantities of air into the engine and substantially increases its pressure and temperature. Modern gas turbines (e.g. Rolls-Royce Trent XWB) are capable of achieving compression ratios of around 50:1 [1]. During this process the air pressure is increased by a factor of 50, while its temperature typically increases by approximately 700K (to 1000K) as a direct result of compression only. The air from the compressor is then fed into a combustion chamber, where fuel is introduced to the compressed air and subsequently ignited. The temperature of the air and fuel mixture is increased substantially. After combustion, the products enter the turbine. For modern engines the Turbine Entry Temperature (TET) is of the order of 2000K [2]. This mixture drives the turbine before exiting the engine as a turbine exhaust jet.

The engine compressor and the turbine are connected by a mechanical spool, or shaft. Together with the combustion chamber they are known as the engine core. The more gas is burned in the engine, the more it accelerates the turbine, which in its turn accelerates the compressor by the mechanical spool to draw even more air into the engine.

1.3 Useful Work done by a Gas Turbine

Useful work can be yielded from the turbine in the form of a propeller (e.g. turboshaft and turboprop designs) or generate electricity by driving an alternator. Some modern ships use the power turbine to drive an alternator to power electric motors that drive propellers. Other vessels use gas turbines to

power a duct pump, which generates a water jet to propel the ship. Regardless of the specific gas turbine design, the engine core is governed by the same basic operating principle outlined above.

The exhaust jet from the turbine however can also be accelerated to such a level that it would give sufficient propulsive thrust levels in its own right (e.g. turbofan and turbojet designs). Figure 1-2 illustrates a schematic drawing of a basic turbojet engine:

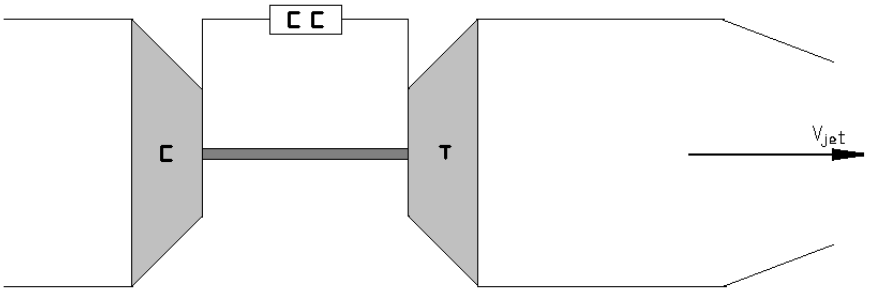

Figure 1-2 - Schematic drawing of a simple turbojet engine

More mechanically complex forms of gas turbines exist with several turbine stages. One or more of those stages could be used to drive the compressor. The other stage or stages could be used to drive the load, which again can vary from an aircraft engine fan to a cruise ship propeller. Figure 1-3 illustrates a schematic drawing of a gas turbine with two turbine stages:

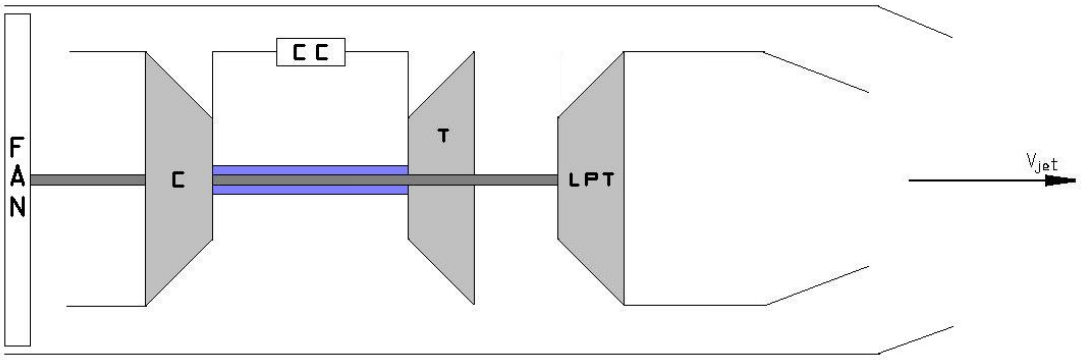

Figure 1-3 - Schematic drawing of a two-shaft turbofan engine

1.4 Gas Turbine Evolution

Due to the large range of operational requirements, gas turbines vary in size, structural complexity and maximum power output. The first turbojet engines were able of producing around 7kN (1600lb) of thrust, compared with approximately 440kN (100000lb) thrust produced by modern turbofan engines. An increase in the maximum power output is directly proportional to the TET of a gas turbine. Principally this is because of two reasons:

1) Increasing the TET causes the pressure ratio across the core turbine smaller in relation to the pressure rise of the core compressor and thereby increases the power available from the LP turbine [3].
2) Increasing TET also increases the engine cycle efficiency, provided that the pressure ratio increases by an appropriate amount [3].

Early designs were able to produce compression ratios of the order of 5:1 and had TET of 1000K, today these values have increased to approximately 50:1 and 2000K respectively. This technological evolution of gas turbines has in part happened as a result of advances in materials science and improvements in turbine blade manufacturing methods.

Maximum TET values are applicable to a maximum power output, such as a take-off condition of an aircraft and cannot be sustained for very long periods, such as an extended aircraft cruise. During cruise conditions, the TET for a modern aircraft engine would be typically of the order of 1450K.

Modern gas turbine blade materials have a much lower melting point than their maximum allowable Turbine Entry Temperatures. A typical melting point value would be around 1500K, which is 500K less than the fluid temperature entering the first turbine stage of a modern turbofan during take-off. Thus an even more important improvement in gas turbine operation is associated with adaptation and improvement of turbine blade cooling, in addition to the effective sealing of turbine stages.

1.5 Turbine Blade Evolution

Thermal fatigue, oxidation and creep can reduce life of a turbine blade. Thermal fatigue occurs as a result of an engine being heated and cooled (started, operated and stopped) over a given number of cycles. Oxidation is a chemical process and its rate and tendency very much depends on the chosen material for a gas turbine blade. Creep occurs as a result of prolonged and gradual extension of turbine blades under stress at high temperatures.

Figure 1-4 [3] illustrates the evolution of TET at take-off between 1940 and 2010. It can be seen that metallurgical advances, such as production of more resilient materials and the improvement of turbine blade manufacturing techniques have resulted in blades that are able to operate at higher temperatures and stress levels than those of early gas turbines.

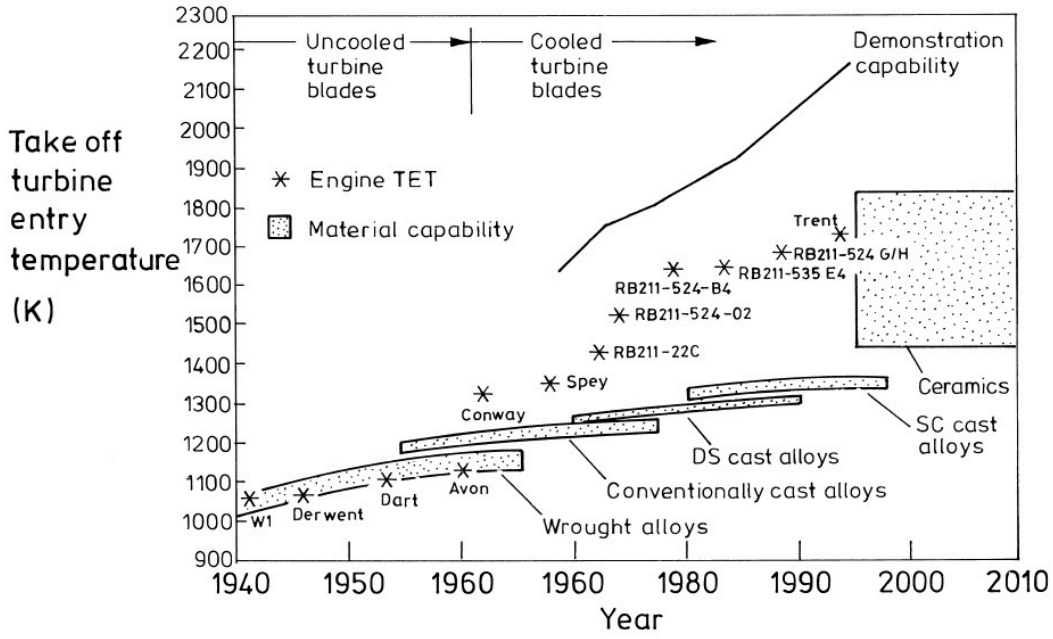

Figure 1-4 - Evolution of TET at take-off

Early blades were forged, this resulted in high levels of creep stress and made difficult the implementation of efficient cooling systems. Improved creep performance has been achieved by using blades that have been cast. The introduction of casting processes has allowed the inclusion of cooling

passages inside the turbine blades. The next improvement has been made by producing directionally solidified blades, where the metal blade was formed from crystals elongated in the direction of the span. A modern and an even more effective production method however is the casting of each blade as a single crystal.

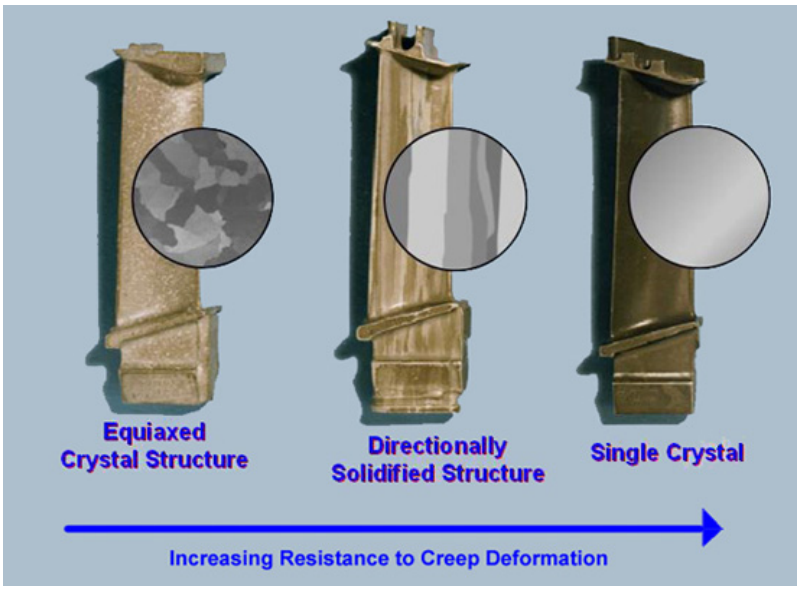

Figure 1-5 - Evolution of turbine blade crystal structure

Turbine blades manufactured with the three different crystal structures are illustrated in figure 1-5 [4]. Creep, oxidation or thermal fatigue limit the life of a turbine blade. Creep is the continuing and gradual extension of materials under stress at a high temperature. A rule of thumb for blades limited by creep is that turbine blade life is halved (at a given level of cooling technology and material) for each 10 K rise in temperature of the metal [3]. It is therefore crucial to design effective cooling systems that would maintain a stable design temperature of turbine blades, especially while they operate at a maximum power output when they are in contact with fluids, which are 500K hotter than the melting point of the blades.

1.6 Thesis Motivation

As it has been outlined in this chapter, the recent technological advance in gas turbine design is largely due to the development of efficient turbine blade cooling. The current development trend shows that turbine cooling will continue to be an important factor in gas turbine design and development in the future.

Development of more efficient turbine blade cooling methods can aid in achieving more efficient gas turbines in the future. This will mean an increase in maximum engine power output or a reduction in fuel consumption. In the current global economic environment with soaring oil prices, this of course implies both reduced operational expenses, as well as pollution levels.

Turbine blades can be cooled in many different ways and as a result various different factors that govern this process can be adapted and changed to achieve more effective, as well as more efficient cooling.

Various technologies are currently used, or can be potentially implemented to analyse how effective, or efficient a turbine blade cooling design is. Various cooling designs and imaging techniques will be explored in the next chapter, while the basic need for continuous development in turbine cooling design has been outlined in this chapter.

The requirement of efficient turbine blade cooling forms the motivation for this thesis, which will focus on analysis of limitations and applications of Infrared Thermography in turbine cooling. Such analysis is necessary to assess the current thermography technologies and design an improved visualisation technique that could aid development of enhanced turbine cooling systems.

2 Turbine Cooling and Contactless Thermography

This chapter contains a literature review of various turbine cooling methods, as well as imaging techniques that are used for analysis of turbine cooling effectiveness. The review is followed by a comparison of the techniques and concluded by selection of Infrared Thermography for the experimental purposes of this thesis.

The focus of this work is analysis of limitations and applications of Infrared Thermography in turbine blade cooling. This technique will be assessed in detail in order to design an improved method of thermal imaging that could be applied to aid development of more efficient turbine cooling systems.

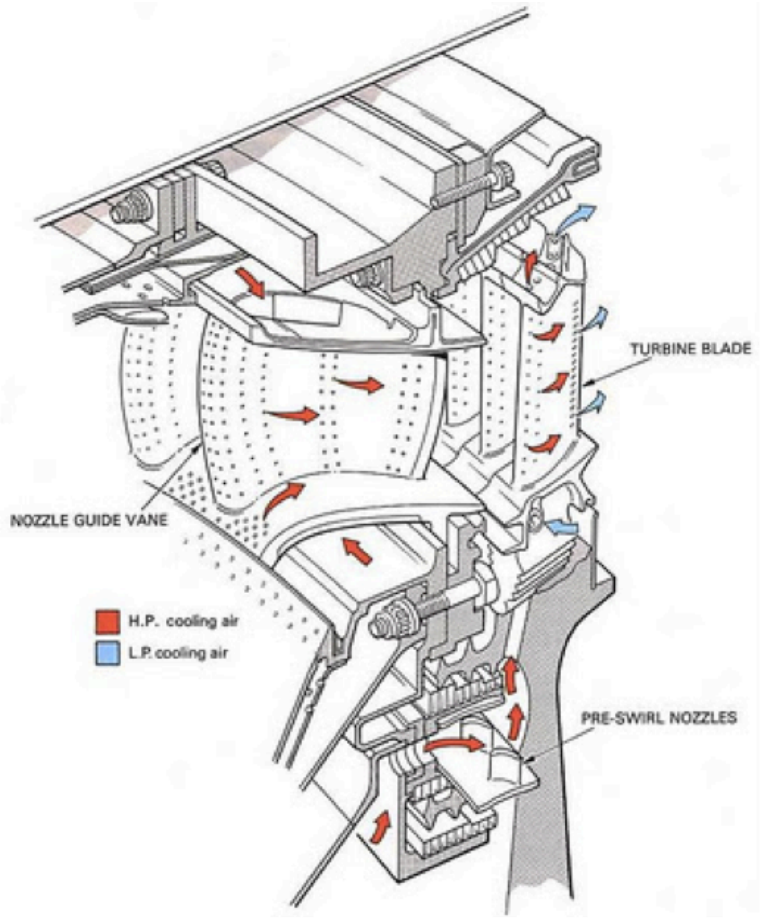

Figure 2-1 - Modern NGV and Turbine Blade Cooling Arrangement

2.1 Turbine Cooling Background

Figure 2-1 demonstrates an example of a modern nozzle guide vane (NGV) and turbine blade cooling arrangement. As it can be seen, the NGVs and turbine blades have a number of small holes around their surface. The coolant flow travels inside of each of the NGVs and turbine blades through a labyrinth of small channel and passes through these holes, which are often referred to as ejection holes, at a pressure of around 3800kPa. Since the gas stream pressure at the turbine inlet is over 3600kPa, the cooling pressure margin is small and maintaining this margin is critical to component operation [5]. As the coolant flow exits the ejection holes it forms a cool film of air around the component's outer surface, shielding it from the hot gas stream. It can also be noted from the diagram that rotor and stator surfaces that are in contact with hot gas stream also have coolant ejection holes. Their locations, dimensions and geometries, as well as pressures with which the coolant exits the holes are selected by the engine designers to ensure optimal cooling.

The exact amount of air, which is drawn from the compressor and used for cooling purposes normally, varies between 15% and 25% of the air mass flow through the compressor [6]. Similarly turbine entry temperature is a compromise between engine performance and turbine life. A balance between TET and cooling air quantities exists, as cooling air reduces engine efficiency and thrust output [6]. Although larger quantities of air would ensure more heat transfer from turbine components to the cooling air, effective turbine cooling comes at a thermodynamic cost. Bleeding the HP compressor reduces the pressure and quantity of air available for combustion in the combustion chamber thus limiting the overall power output of the turbine. Coolant gas incurs pressure losses in the feed, delivery and turbine blade inner passages. In addition to this, viscous mixing of coolant with the mainstream gas after ejection will reduce thermodynamic efficiency of the turbine. The TET can typically be raised by 100 K for each additional 1% of coolant flow with a resultant loss of 1% in turbine efficiency [7].

A gas turbine is often the most expensive equipment on a vehicle and major resources are invested into continuous development of efficient cooling systems. Maintaining a controlled TET is therefore crucial in prolonging the life of the gas turbine components. The total cost to replace a single first vane is on the order of thousands to tens of thousands of dollars, of which a significant fraction is required to manufacture or repair film-cooling holes in the vane [8]. Generally a replacement or repair is required because the leading or trailing edges have burned away while the main body of the aerofoil remains intact [8]. Cooling systems research is hence considered to be very competitive in general, while leading or trailing edge cooling research provides possible improvement to the most critical turbine aerofoil locations.

2.2 Turbine Blade Cooling Methods

It has in fact always been the practice to pass a quantity of cooling air over the turbine disc and blade roots. The term ‘cooled turbine’ is applied to turbines where a substantial quantity of coolant is applied to the nozzle and rotor blades themselves [9]. The majority of the increase in turbine entry temperature has resulted from improvements in turbine cooling technology.

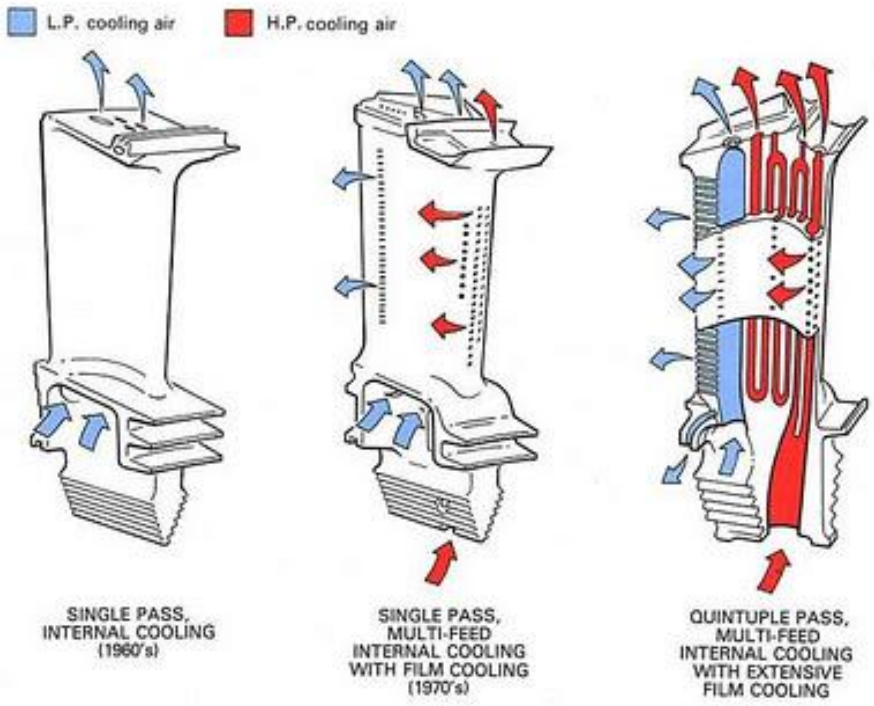

Figure 2-2 - Development of HP turbine blade cooling

Figure 2-2 [5] demonstrates the development of turbine blade cooling technology over the last 50 years. Early blade cooling designs included simple coolant channels to allow the air to pass inside the turbine blade from its root to its tip. This method is known as convection cooling, where the blade acts as a single-pass cross-flow heat exchanger, in which compressed air, flowing radially through the coolant channels, removes the heat convected to the blade from the mainstream hot gas, flowing axially [6].

Improvements in manufacturing methods have enabled more complex cooling systems with provision for external film cooling, as well as multi-feed cooling system with differentiated air supply, where the air would be ejected from the turbine blade at different pressures in order to ensure most effective cooling and interaction minimise turbine efficiency reduction due to interaction of coolant and hot gas stream in the turbine. The ability of casting the blade with a labyrinth of coolant passages effectively turns the blade into a multi-pass heat exchanger. Cooling systems that have attracted the most attention in the past are considered in the next sections.

2.2.1 External Liquid Cooling

Several liquid cooling system variations exist, however apart from the use of external (spray) cooling for thrust boosting in turbojet engines, they have not proved to be practical [9]. An example of external liquid cooling is spray cooling, often referred to as sweat cooling, in which a cooling liquid exits through a porous wall upstream of a rotor blade leading edge and cools the surface. A technology patented in 1958 describes an external liquid cooling method, where liquid-emitting nozzles are incorporated into the trailing edges of the stator guide vanes (figure 2-3), upstream of turbine rotor blades [10].

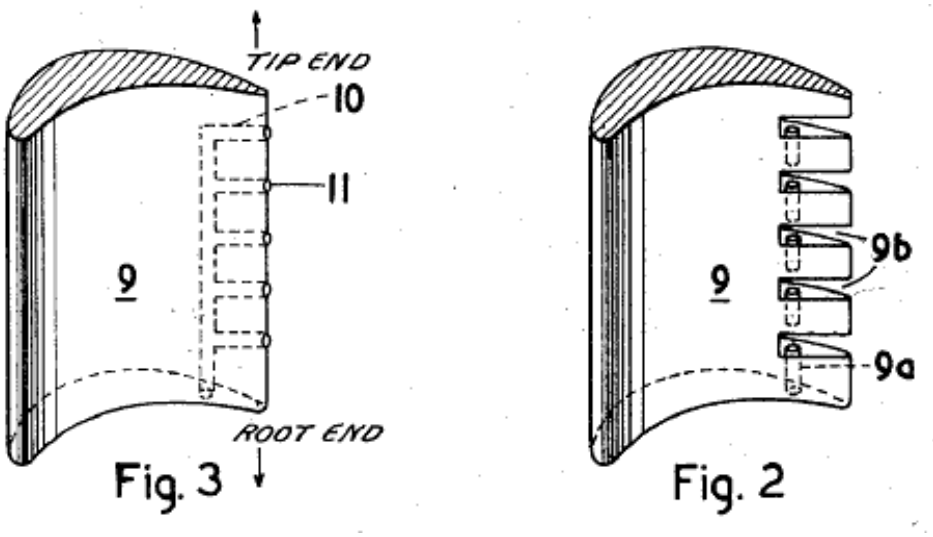

Figure 2-3 - Liquid-emitting nozzles incorporated into NGV

These nozzles are located specifically to direct jets of coolant liquid directly on to the leading edges of the turbine blades. Water is suggested as a potential coolant, however liquid fuel may also be used and combusted further downstream of the turbine to provide thrust boosting.

2.2.2 Internal Liquid Cooling

Other forms of liquid cooling (primarily internal cooling) have been explored experimentally, but none have been implemented in production due to the difficulties associated with channeling the coolant to and from the turbine blades [9]. Historically, only internal, forced convection, air cooling has been used for internally cooling mass-produced gas turbines.

2.2.3 Internal Convection Gas Cooling

As previously stated, modern gas turbine blades are internally cooled by forced convection. The compressed cooling air circulates through the internal labyrinth of coolant passages inside a turbine blade, the surface of which has roughness elements, which are designed to enhance heat transfer between the blade metal and the coolant gas.

2.2.4 Impingement Cooling

In certain areas of a turbine blade, a method known as impingement cooling may be used. Impingement cooling is achieved by directing a jet of coolant onto a hot surface. The jet exits an impingement orifice and collides with a surface, achieving very high rates of heat transfer at the stagnation point.

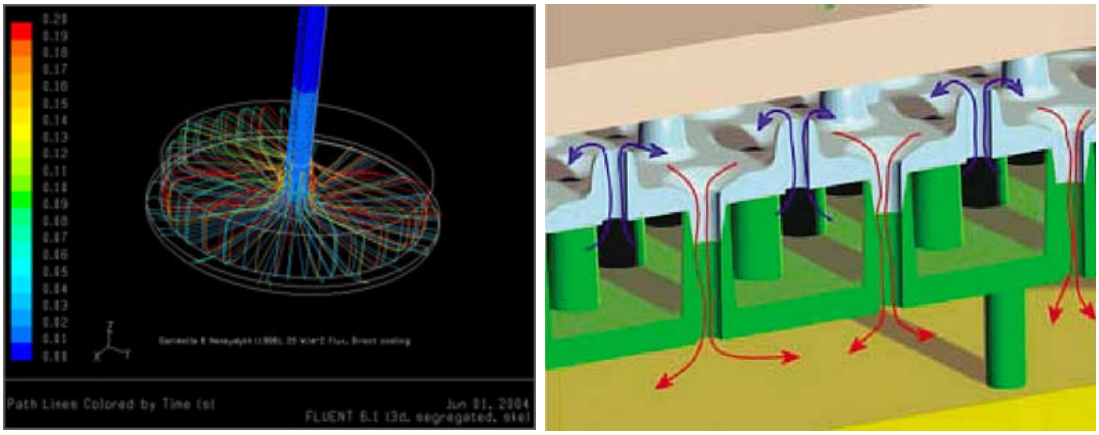

Figure 2-4 - Jet impingement (left); multiple impingement jets (right)

Figure 2-4 (left) [11] illustrates a CFD model of jet impinging on a surface, it can be seen that the heat tends to spread along the surface following the impingement. At a given radial distance away from the jet centerline along the surface, the flow tends to separate from the surface. Inside a gas turbine blade coolant gas is circulated similarly to representation in figure 2-4 (right) [12], where cool gas (blue arrows) is impinged onto a hot wall, gains thermal energy and leaves to an outlet convection passage as a warmer gas (red arrows).

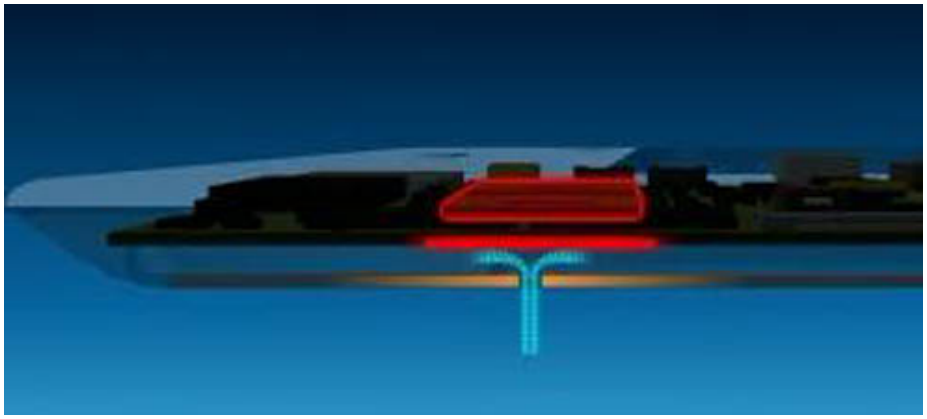

Figure 2-5 - Intel laptop processor being cooled by an impingement jet

This technology is widely used to cool electronics, an example of which is shown in figure 2-5 [13] where an Intel laptop processor is being cooled by an impingement jet in order to lower its temperature and minimize the feeling of “hot laps” of the user.

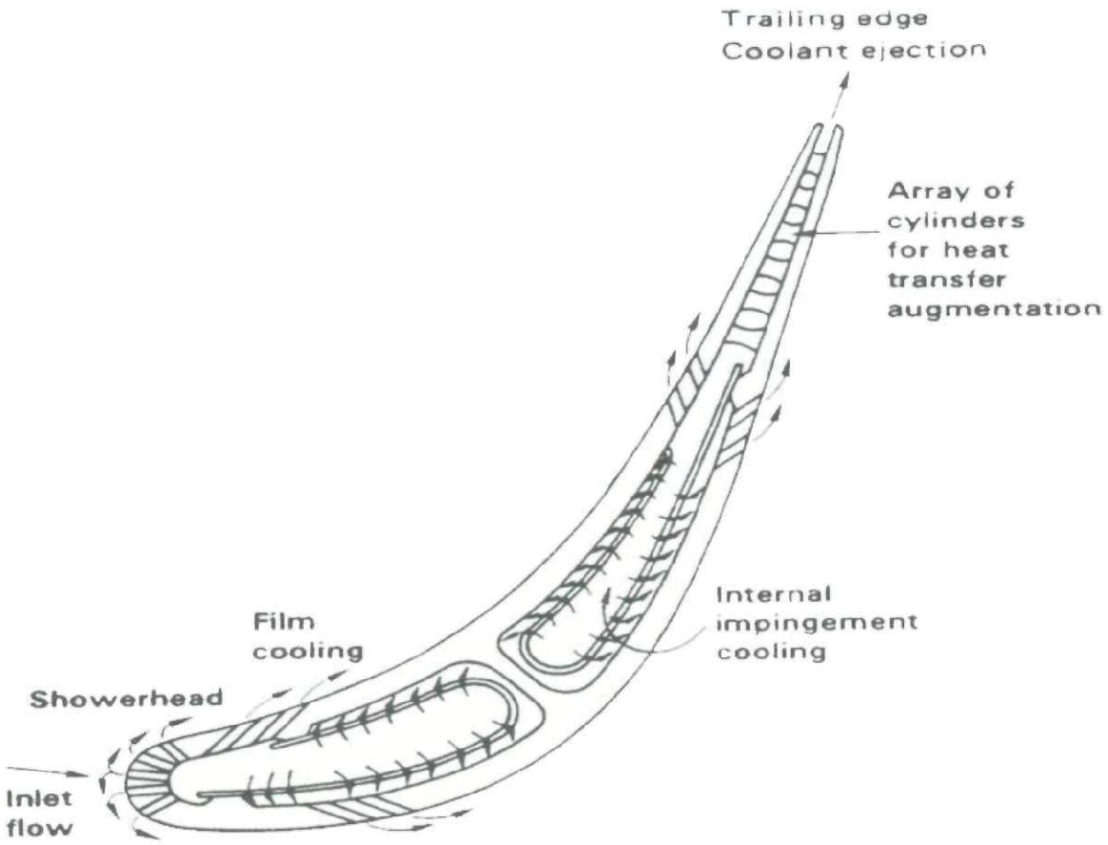

Figure 2-6 - Turbine cooling techniques

In a modern internally cooled gas turbine blade, impingement cooling techniques are used to cool the outer shell of a turbine blade. As can be seen from figure 2-6 [14], compressed air is drawn in from the forced air convection coolant passages and fed through multiple series of small impingement holes into cavities adjacent to the outer shell of the blade. These multiple impingement jets are directed normal to the blade curvature and cool some of the hottest regions of the blade from the inside. In the example shown, impingement cooling is used both over the suction and pressure surfaces of the blade, however the extent to which it is used and the location within a blade varies greatly for different engine types and blade designs.

2.2.5 Transpiration Cooling

Transpiration or effusion cooling is achieved by forcing the coolant air to effuse out of the blade through very small pores in the blade material. This method ensures the most economical use of cooling air than in traditional film cooling through series of ejection holes due to the following reasons:

i) More heat is absorbed from the turbine blade outer wall as the area of coolant-wall interaction is maximised

ii) Heat is absorbed more uniformly across the turbine blade surface as the ejection pores are spread more uniformly and densely than traditional ejection holes

iii) For the same reason, more effective film-cooling is established with more uniform film of the effusing coolant flow, which insulates the entire outer blade surface from hot mainstream gas and reduces the rate of heat transfer to the blade [9]

Transpiration cooling technology is described in various patents [15,16], whereby a transpiration cooled turbine blade has a number of structural struts covered with porous laminated material. Advances in available materials and manufacturing techniques may ensure its widespread application in the future.

2.2.6 External Film Cooling

The highly compressed air that is used to cool a turbine blade internally can successfully be used to shield the outer blade surface from hot mainstream gas and therefore lower the blade surface temperature. As previously discussed this is achieved by introducing a thin film of coolant air through multiple coolant ejection holes around the outer surface of many engine components. The coolant ejection holes are precision-drilled by electrochemical or laser drilling to form any complex shapes necessary to

ensure the most effective introduction of a coolant film to the outer surface of an engine component. A great deal of research effort around the world has been put into coolant ejection holes to determine most effective cooling methods. This has considered the shape, size, location and configuration of the holes (relative position and orientation of each hole on the blade surface).

2.3 Turbine Blade Leading Edge Cooling Research

Methods for turbine blade cooling have been extensively discussed over the previous sections. The area of a turbine blade that is exposed to greatest temperatures and requires most effective cooling is the turbine blade leading edge. A modern turbine blade leading edge is usually cooled by forced air convection and impingement cooling internally. Some of the coolant air is allowed to exit to the outer blade surface through a number of coolant ejection holes to cool the blade externally via film cooling.

Accurate thermal design of gas turbine components requires detailed knowledge of heat transfer rates and component temperatures. The design process is made difficult due to the high degree of uncertainty in local heat transfer measurements and hence the local material temperatures. Numerical tools together with experimental results achieved in *near-engine* conditions aid in determining the best thermal design of engine components.

Increasing the cooling effectiveness through selection of optimal coolant exit hole parameters can optimise turbine cooling. Another way of improving the cooling effects would be to determine the optimal amount of coolant required in order to limit the amount of air from the compressor that should used for this purpose.

The following section of this chapter will concentrate on a review of research papers, which describe successful attempts of experimentally visualising and analysing turbine blade cooling effectiveness.

2.3.1 Showerhead Configuration

The arrangement of coolant ejection holes along the leading edge of a turbine blade is sometimes referred to as a showerhead configuration. Showerhead is used to protect the stagnation point area from extreme temperatures and is complicated because of strong curvature effects [17]. Variations in size, shape, number and locations of these holes exist for different turbine blades.

2.3.2 Effect of Ejection Hole Geometry

Hole geometry is known to influence film cooling effectiveness. For instance an expanding coolant exit hole tends to yield better film cooling [18,19,20]. This fact has been attributed to reduced mixing of the coolant with the mainstream hot gas. The reason for this result is a reduction in coolant momentum due to hole expansion, which results in reduction of the coolant jet's ability to detach from the surface that needs cooling. A reduction in the coolant momentum compared with the momentum of the hot mainstream gas is essentially a reduction in coolant-mainstream momentum ratio.

2.3.3 Blowing Ratio Parameter

A Blowing Ratio (BR) parameter (also known as coolant-to-mainstream mass flux ratio) is often used to assess the effect of coolant injection rates on turbine blade cooling effectiveness [19]. The local blowing ratio varies circumferentially around the surface of a cylinder in cross flow and can be related to the coolant-to-mainstream pressure ratio as defined in figure 2-7.

$$BR_{\phi} = \sqrt{\frac{\left(p_{oc} - p_{s\phi}\right)}{\left(p_{om} - p_{s\phi}\right)}}$$

Figure 2-7 - Blowing Ratio definition

Blowing Ratio value is known to affect the jet trajectory after ejection. For a typical gas turbine blade, the coolant-to-mainstream pressure ratios vary from 1.02 to 1.10, while the corresponding Blowing Ratios vary approximately from 0.5 to 2.0 [21].

2.3.4 Effect of Coolant-Mainstream Momentum Ratio

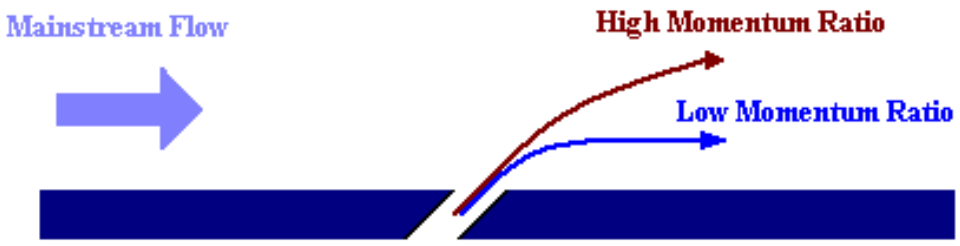

Figure 2-8 - Effect of coolant-mainstream momentum ratio on jet lift-off

Coolant ejection rate and coolant-to-mainstream density ratio have an effect on coolant-mainstream momentum ratio and hence jet lift-off and film cooling. The effect of varying coolant-mainstream momentum ratio (also known as (coolant-to-mainstream) Momentum Flux Ratio, or (MFR)) on the jet tendency to lift-off can be seen in figure 2-8. Goldstein *et al.* [18] conducted flow visualisation experiments with a dense coolant (Freon vapour – approximately 3.5 times denser than mainstream) and found that coolant jet remains attached to the surface at significantly higher Blowing Ratio values than when coolant of the same density as mainstream is used. Using a denser-than-mainstream coolant therefore ensures more effective cooling.

In fact the coolant is denser than the mainstream in most practical applications as it is generally much colder than the mainstream. Difference in densities may also arise from the difference in chemical composition of the two fluids. The coolant-to-mainstream density ratio for a typical gas turbine blade varies between 2.0 and 1.5 [21].

MFR and BR are defined respectively as:

$$MFR = \frac{\rho_c v_c^2}{\rho_m v_m^2} \qquad \text{and} \qquad BR = \frac{\rho_c v_c}{\rho_m v_m}$$

Since the same gas is used as mainstream and coolant in this work (air in the laboratory room) and their temperatures differ very modestly, the coolant-to-mainstream density ratio is assumed to equal unity. Therefore both local MFR and local BR values at a specific circumferential location around a cylinder surface in the wind tunnel mainstream flow are assumed to depend on local velocities only. Mainstream velocity at a cylinder wall surface can be expressed as:

$$p_{om} = p_{s\phi} + \frac{1}{2}\rho_m v_{s\phi}^2$$

$$v_{s\phi} = \sqrt{\frac{2\left(p_{om} - p_{s\phi}\right)}{\rho_m}}$$

Similarly the coolant velocity at a cylinder wall surface can be expressed as:

$$p_{oc} = p_{s\phi} + \frac{1}{2}\rho_c v_{c\phi}^2$$

$$v_{c\phi} = \sqrt{\frac{2\left(p_{oc} - p_{s\phi}\right)}{\rho_c}}$$

Therefore local MFR and local BR parameters can be expressed in terms of known variables as:

$$MFR_\phi = \frac{p_{oc} - p_{s\phi}}{p_{om} - p_{s\phi}} \qquad \text{and} \qquad BR_\phi = \sqrt{\frac{p_{oc} - p_{s\phi}}{p_{om} - p_{s\phi}}}$$

And for the purposes of this study, MFR and BR are approximately related as:

$$MFR_\phi \approx \left(BR_\phi\right)^2$$

2.3.5 Gas Effectiveness Parameter

Various studies have used non-dimensional effectiveness parameters for quantitative analysis of coolant jets [19,20,22]. Generally adiabatic wall effectiveness is used for analysis of coolant jets on a test surface (such as a cylinder model wall), while gas effectiveness is used for analysis of coolant jets on a nylon mesh. The parameters are defined in figure 2-9 below:

$$\eta_{aw} = \frac{T_{aw} - T_m}{T_{cg} - T_m} \qquad \eta_{gas} = \frac{T_{mesh} - T_m}{T_{cg} - T_m}$$

Figure 2-9 - Adiabatic Wall Effectiveness (left), Gas Effectiveness (right)

2.3.6 Effect of Ejection Hole Inclination Angle

An inclination of the coolant holes into the mainstream flow direction is found to further reduce the tendency of jet lift-off [20]. Modern turbine blade coolant holes are often given both a spanwise and streamwise inclination (compound angle orientation). Inclination also increases the hole length, which has an improved effect on convective cooling of the inner surface of the hole [22]. The number of coolant hole rows also has an effect on cooling.

2.3.7 Turbine Blade Leading Edge Model

A study by Reiss and Bolcs [20] has constructed a turbine blade leading edge model to experimentally compare cooling effectiveness of three different showerhead geometries (figure 2-10) [20].

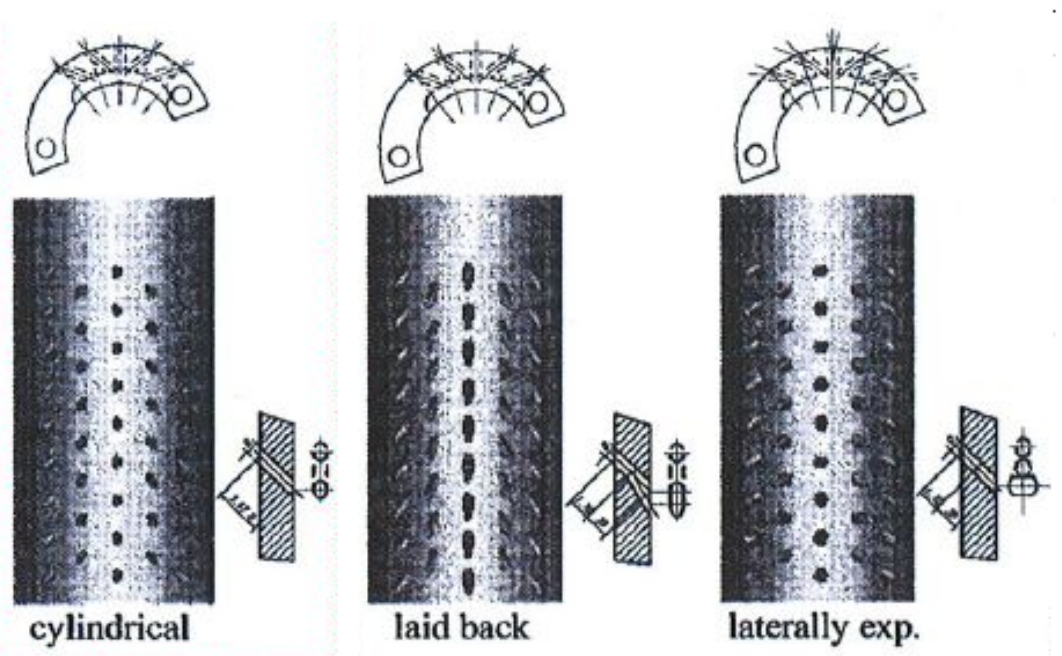

Figure 2-10 - An overview of showerhead geometries

These studies used a cylindrical model with five rows of coolant ejection holes (at 0, $\pm 20°$, and $\pm 40°$ from the stagnation line) in free jet airflow. The coolant gas was fed into a plenum chamber inside the cylinder before it was ejected through the coolant ejection holes. The transient total temperature in the plenum was measured with fast-response thermocouples. The circumferential distribution of coolant total pressure over the cylinder outer surface was acquired with series of pressure taps. Both the mainstream and coolant temperatures were recorded with fast-response thermocouples. Hot mainstream (60-65℃) and cold coolant (approximately -15℃) were used in this study.

The coolant jets in this study have only been visualised on the cylinder surface, but for a range of coolant injection rates and hole geometries. Cylinder surface was coated with narrow-band thermochromic liquid crystal (TLC) and recorded with a CCD Mini Camera. The nature and practical applications of TLCs is reviewed later in this chapter (section 2.6).

2.3.8 Hot Coolant Imitation Gas and Ambient Mainstream

Mee *et al.* [22] conducted low-speed wind tunnel experiments on a cylinder model, representing the leading edge of a turbine blade. Contrary to Reiss and Bolcs [20], this group used a heated "coolant" air supply, which was ejected through the coolant holes into the mainstream flow at ambient conditions. The flow to the film is a small fraction of the tunnel mainstream flow and by choosing to heat the films in an unheated tunnel, rather than vice versa, a dramatic reduction in heater power consumption was achieved. In this experiment only one row of holes (with three coolant exit holes) was used.

2.3.9 Perpendicular Nylon Mesh

Mee *et al.* [22] set a TLC-coated fine nylon mesh at perpendicular to the cylinder surface downstream of the holes. The mesh was viewed with a CCD video camera to record net temperature contour plots produced by the coolant jets off the cylinder surface. Temperature distributions across the cylinder surface were not recorded in this study.

The nylon mesh consisted of thin (<0.2mm diameter) black fibres woven into an approximately hexagonal shape. A choice of a fine mesh was made to ensure the net is non-intrusive, so far as the incident flow is concerned. The University of Oxford Turbomachinery Research Group has conducted these experiments, and hence the mesh is referred to as an Oxford mesh in this thesis. Sangan *et al.* [7] conducted a comparison of the Oxford mesh with four other mesh profiles. The Oxford mesh was most porous and predictably caused least pressure drop across the mesh. Nets with smaller diameter apertures have resulted in coolant imprints of higher gas effectiveness values. This was has been attributed to increased mesh interaction with film trajectory, forcing the coolant closer to the blade model surface.

The thermal conductivity of the nylon fibres and the temperature gradients along them were such that conductive heat transfer along the net was

negligible compared with the heat convected from the flow. Video images of the mesh can be digitised into components of hue, saturation and intensity using a PC-based image-capturing system.

Mee *et al.* [22] found that the spanwise extent of the films decreases when the holes were moved away from the stagnation line (i.e. when the cylinder model was rotated). It was noted that a fine nylon TLC-coated mesh could be successfully used to the measure temperature of a heated jet. This technique allowed qualitative visualisation of the coolant jet trajectories, as well as quantitative gas-effectiveness measurements.

2.3.10 Kidney Vortex

Mee *et al.* [22] was also able to capture images of kidney shape vortices on the nylon mesh. It is believed that as a coolant jet travels through a coolant hole passage, the sidewall boundary layer causes vorticity in the coolant flow (jet shear-layer vortices). This vorticity is then subjected to further turning upon interaction with the crossflow after the coolant is ejected through the ejection hole. This leads to formation of a counter-rotating vortex pair with distinctive kidney-shaped cross-sections (figure 2-10 [19]).

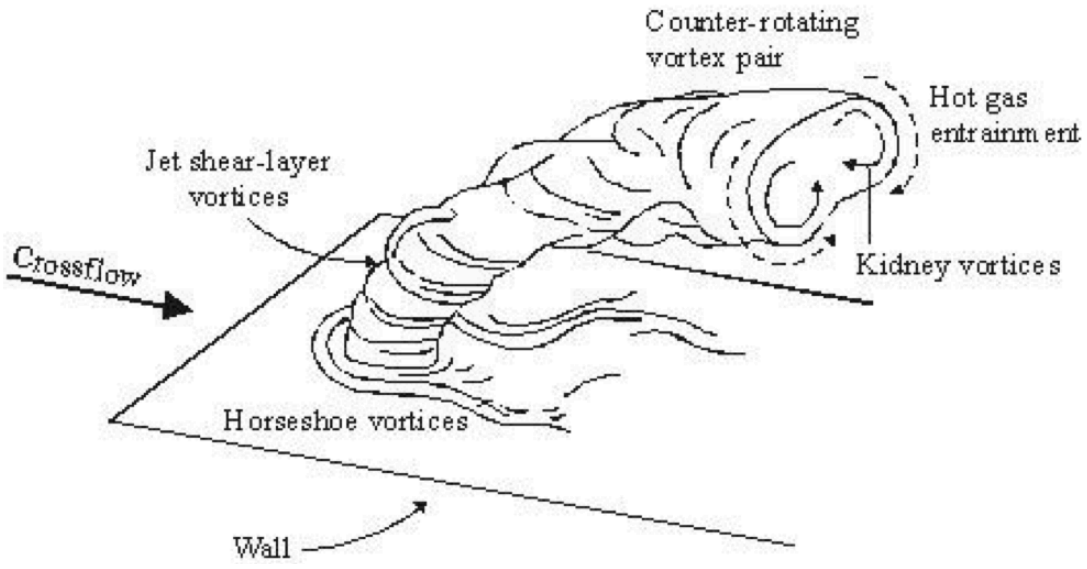

Figure 2-11 - Formation of the Kidney Shape Vortex

Coat and Lock [19] have used a similar TLC-covered fine nylon mesh to measure coolant gas temperature contours in perpendicular to the flow. The coolant (air heated between 30℃ and 60℃) has been ejected from a TLC-covered flat plate into a low speed wind tunnel air with ambient conditions. This study was also able to capture distinct images of kidney vortices, expected during ejection from cylindrical holes.

A study by Haven and Kurosaka [23] has outlined that these vortices increase the tendency of a jet to lift off the surface and hence decrease film-cooling effectiveness. Six different hole geometries were compared to conclude that formation of kidney vortices, as well as the jet tendency to lift-off can be influenced by changing geometry of the ejection holes alone.

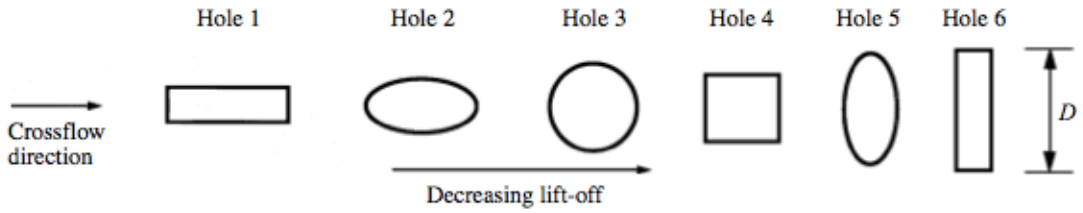

Figure 2-12 - Trend of jet lift-off with hole geometry

Figure 2-11 [23] summarises the results of this study and shows that the jet's tendency to lift-off reduces with increasing aspect ratio of the ejection holes.

2.3.11 The University of Oxford Research Group

The work of the University of Oxford turbomachinery research group has been sponsored by Rolls-Royce Plc. and included review of thermal problems specific to the jet engine. This included studies of internal and external cooling simulations of various gas turbine components. The group has used transient method of measuring Heat Transfer coefficients and Adiabatic Wall Temperature with Thermochromic Liquid Crystals that finds its beginnnings in early 1980s [24]. Scale models of engine components manufactured from transparent plastic such as Perspex (PMMA) provided poor thermal conductivity and good optical access. A mesh heater was used to heat the

mainstream flow. The translucent nature of the mesh heater allowed camera views of a plate cooled by impingement jets (simulating internal impingement cooling of a turbine blade) to be taken through the heater [24]. In this particular study the group has processed the images to extract data from the mesh background, which is the reverse process of analysing gas effectiveness on an Oxford mesh [22]. Heat transfer to a pedestal cylinder and adjacent walls in fully developed passage flow (simulating internal cooling flow around a cooling passage within a turbine blade) was studied where complex secondary flows such as a horseshoe vortex around a cylinder were analysed [25]. A horseshoe vortex was determined to enhance heat transfer to the wall in a localised region around the pedestal cylinder. Such vorticity is expected to be observed on a turbine blade leading edge surface around an ejecting coolant flow as seen in figure 2-10. Other studies of the group included Heat Transfer coefficient analysis on ribs, fins and film-cooled plates (simulating combustor liners, as well as turbine blade pressure and suction faces).

2.3.12 University of Texas at Austin Research Group

The University of Texas at Austin Gas Turbine Research Group has conducted a number of studies funded by Pratt & Whitney in the United States. Cutbirth and Bogard [26] studied showerhead cooling on a scaled Pratt & Whitney turbine vane model and it was found that the upstream coolant jets from the leading edge showerhead region influence the angle at which downstream jets are blowing at the pressure side of the aerofoil. Showerhead cooling was also found to create additional turbulence and lower adiabatic wall effectiveness along the aerofoil pressure side [26].

A Computational Fluid Dynamics (CFD) study [27] simulating leading edge cooling of a turbine aerofoil with two rows of ejecting holes (at $0°$ and $25°$ from Stagnation Line) obtained laterally averaged adiabatic effectiveness values in good agreement with a parallel experimental study of the same research group [28] (although peak effectiveness values have been overpredicted).

Steep temperature gradients have been reported on the side of the coolant jet furthest from the coolant hole exit where severe mainstream crossflow is preventing the coolant from penetrating into the lateral direction. The group has described mainstream turbulence, aerofoil surface curvature and Blowing Ratio parameter as some of the most dominating effects on film-cooling performance in gas turbines [8,27]. The source of mainstream turbulence is primarily the combustor upstream of the turbine [8].

Harrington *et al.* [29] have performed an experimental and computational study of film cooling adiabatic effectiveness on a flat plate with full coverage film cooling (simulating combustor liner). Realistic engine conditions were simulated with a large density coolant and high mainstream turbulence. It was found that high mainstream turbulence decreased effectiveness by 12-14% for BR values 0.65-1.0. This effect was even larger for lower BR values (30% at BR=0.25), as coolant jets were penetrating less into the mainstream and were largely attached to the plate. For separated coolant jets at higher BR, the increased dispersion caused by a highly turbulent mainstream was found to have a beneficial effect of returning coolant to the test plate surface [29].

More recently, Nathan *et al.* [30] studied adiabatic film cooling effectiveness on a Perspex turbine vane model with leading edge showerhead film cooling. Additional coolant ejection hole rows were present on both pressure and suction sides of the aerofoil. Additionally, a separate identical conductive metal model was tested in this study with both internal and external cooling under engine-representative Biot number to assess the overall cooling effectiveness of the turbine vane model. This allowed to analyse hot spots across the model surface which result in the course of a combination of internal and extrenal cooling methods. The hot spots were reported to represent hot spots in a real turbine vane and be the common places of vane failure. A substantial increase in overall cooling effectiveness with increasing momentum flux ratio was reported and attributed to increasing adiabatic film effectiveness, as well as increasing impingement cooling internally and increasing convective cooling within the coolant holes. The drop in overall cooling effectiveness between the rows of coolant holes was much less than

the drop in adiabatic cooling effectiveness due to the significant conduction effects. Continuous improvement of adiabatic film cooling up to the maximum MFR=6.7 was observed. Coolant jets were seen to detach at MFR higher than 0.76. In the showerhead region a substantial increase in Adiabatic Cooling Effectiveness was noticed between MFR=2.9 and MFR=4.7. Jets began to merge at higher MFR values, resulting in blockage of mainstream flow from penetrating between coolant holes and consequentially a substantial increase in Adiabatic Cooling Effectiveness [30].

Dyson *et al.* [31] studied adiabatic wall and overall effectiveness over the leading edge region of a turbine blade model. Liquid Nitrogen coolant (at 200K) with ambient mainstream was used to maintain constant coolant to mainstream density ratio of 1.5. The conductive model used internal impingement cooling, as well as external film cooling through three rows of cylindrical holes. The pitch was varied from 7.6d to 11.6d for BR ranging from 0.5 to 3.0. Increasing BR resulted in increased impingement cooling internally and increased convective cooling through the holes. In contrast to expectations, a modest decrease in overall effectiveness (4%) was reported for a 26% increase in pitch at p/d=9.6. However, a significant reduction in overall effectiveness (16%) occurred for a 53% increase in pitch at p/d=11.6. The decreased sensitivity of pitch variation in the region between coolant holes is due to the overall effectiveness contribution of internal cooling [31].

Albert *et al.* [32] studied adiabatic effectiveness and the overall cooling effectiveness for a generic blade leading edge using three rows of shaped (forward-diffused) coolant holes centered about the stagnation line for BR values 1.0 to 4.0. Laterally averaged adiabatic effectiveness was reported to increase with BR up to the maximum value of 4.0 for up to x/d=10. The study showed the importance of accurate model horizontal alignment, as a modest $\pm 3°$ change in incidence of the stagnation line row could result in up to 20% deviation in laterally averaged adiabatic cooling effectiveness. Additionally the study reported an increase in laterally averaged adiabatic cooling effectiveness of at least 20% for shaped holes over cylindrical holes [32].

2.3.13 Texas A&M University Research Group

Mehendale and Han [33] conducted experiments on a blunt body with a semi-cylinder leading edge and four rows of ejection circular holes at $\pm 15°$ and $\pm 40°$ from the stagnation line. Film effectiveness was found to decrease with increasing mainstream turbulence, but this effect reduced with increasing BR. A later study by Mehendale and Han [34] used the same equipment to analyse the effect of mainstream Reynolds number on leading edge film effectiveness for several coolant hole shapes and spacings, film hole row locations, Blowing Ratio values, as well as mainstream turbulence levels. Film effectiveness was found to increase with mainstream Reynolds number at all BR values and turbulence levels. This was attributed to jet deflection and jet entrapment within the boundary layer due to the higher momentum near the surface of the higher Reynolds number mainstream flow. Contrary to Re=100000, mainstream turbulence was not found to affect the film effectiveness distributions at lower Re of 40000 and 25000 because of a thicker boundary layer [34].

Li *et al.* [35] has assessed the effect of coolant density on leading edge showerhead cooling. The coolant to mainstream density ratios were varied (1.0, 1.5 and 2.0) for BR from 0.5 to 2.1. A larger density ratio was reported to make more coolant attach to the surface and increased film protection for all four tested different coolant hole geometries (cylindrical and shaped both with/without compound angle). The density ratio effect was found to be more profound for cylindrical holes than for shaped holes. The observation of higher cooling effectiveness for a heavier coolant was in agreement with earlier results published by Goldstein *et al.* [18]. This effect was attributed to heavier coolant having lower momentum, being less susceptible to lift-off and having a lower tendency to interact and mix with mainstream [35].

Ahn *et al.* [36] measured detailed film cooling effectiveness distributions in the leading edge region of a gas turbine blade with three showerhead rows for different blade rotational speeds and BR values. Increasing BR resulted in coolant gas spreading towards the blade tip, faster coolant jet decay, but

more uniform film distribution across the blade surface and hence higher spanwise averaged cooling effectiveness. Blade rotational speed was found to influence and alter the film cooling flow path direction and distribution at all averaged BR values (0.5, 1.0 and 2.0) [36].

2.3.14 Other Gas Turbine Research Groups

Many research groups across Europe, Asia and North America, have also studied various factors that influence gas turbine cooling. Lu *et al.* [37] used Thermochromic Liquid Crystals to study influence of hole geometry on leading edge cooling effectiveness. A semi-cylinder leading edge with three rows of coolant holes and a flat afterbody was used to model the turbine blade showerhead for 5 different hole geometries. Film effectiveness was found to peak at an averaged BR=1.5. Higher cooling effectiveness values was achieved with shaped holes than circular holes [17,37]. Liu *et al.* reported that shaped holes produced higher film coverage than circular holes at higher BR [38]. Film cooling performance of cylindrical and laid-back holes were assessed to investigate the influence of hole shape and pitch (5d and 8d) for average BR values between 0.7 and 2 [38]. Increasing BR caused spanwise deviation of jet trajectory and gradual lift off (due to strong exit momentum), but more surface area has benefited from film protection for higher BR (due to large jet flux). Smaller pitch resulted in higher laterally averaged effectiveness due to larger proportion of film covering area.

Schulz [39] used Infrared Thermography to study film-cooling effectiveness for cylindrical and shaped holes for a range of Blowing Ratios (0.5-1.5). Higher cooling effectiveness was obtained for higher BR, while better surface coverage and average laterally-averaged film-cooling effectiveness was obtained at lower BR values.

Yuen and Martinez-Botas [40] studied film cooling effectiveness on a flat Perspex plate with a single cylindrical hole for different streamwise (inclination) angles ($30°$, $60°$ and $90°$) and BR values between 0.33 and 2.

The injection hole inclination angle was found to affect cooling effectiveness (approximately 20% higher effectiveness was achieved at $30°$, than at $60°$ and $90°$) for x/d between 0 and 13. L/d parameter (hole length to diameter ratio) was also found to affect the adiabatic cooling effectiveness values. This was attributed to a long hole delivering a fully developed pipe flow at the hole exit, in contrast to a short hole leading to larger effective injection angles which would, in turn, result in jet lift off at a smaller BR [40]. An L/d value of 4 has been reported in a different study as short, but engine representative [41]. Coolant hole length tends to be longer at the stagnation line of a turbine blade and decreases in length further downstream along the blade surface. L/d can be increased by inclining a hole to the surface. These parameters are often determined by manufacturing constraints. Coolant takes heat from the blade material en-route through the holes and this is also a factor that is considered by a turbine blade designer when choosing an inclination angle for a specific coolant hole [17]. Most coolant holes are angled at $25° - 35°$, which promotes keeping the coolant jets attached to the surface. In some cases, however, steeper angles of injection are used due to manufacturing or geometrical constraints [8]. The surface angle of the holes may be oriented with the mainstream flow direction, or inclined at some angle with respect to the mainstream flow direction. Coolant holes that are directed at a nonzero angle from the mainstream flow direction are generally referred to as a compound angle holes [8].

2.4 Turbine Disc Cooling and Sealing

Historically, internal and external turbine blade cooling methods have captured most of the research attention. However research into turbine disc cooling and sealing is a growing area of interest among academic groups around the world and is of fundamental importance to turbine cooling.

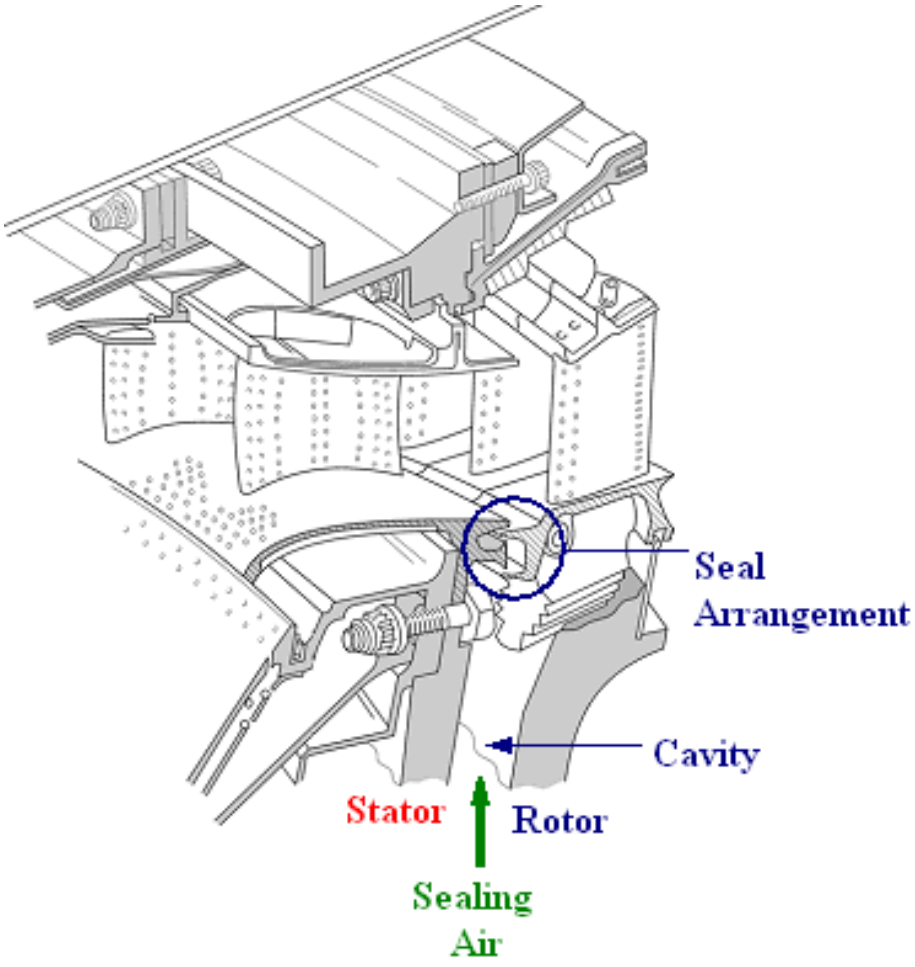

Figure 2-13 - A typical stator-rotor turbine stage

Figure 2-13 [42] illustrates a typical turbine stage with an upstream stator with vanes and a downstream rotor with blades forming the mainstream annulus. For mechanical reasons, the rotor disc rotates at a small clearing distance away from the stator disc. During turbine operation, hot mainstream gas is drawn into this clearance (a process known as ingestion). The ingress air enters the wheel-space cavity between rotor and stator discs where it circulates before exiting back through the clearance as egress air. A curious reader is referred to studies [43,44] for more information on ingress.

Hot ingress air has a detrimental effect on the stator and rotor metal structural components. Cool sealing air (pumped from the engine compressor) is fed into the cavity to limit ingress. Various seal arrangements around the turbine and stator rims are installed to limit this effect. A double seal in this particular example separates the wheel-space and the annulus. Sealing the wheel-space from hot air ingress essentially reduces the surface temperature of rotor and stator discs. Cooler discs imply greater heat transfer from the turbine blades to the disc and hence ingress prevention aids blade cooling.

The research and experimental techniques used and developed in this study are not limited to analysis of turbine blades and are widely applicable to ingress research. The subject of turbine disc cooling and sealing is however beyond the immediate scope of this project, and is not covered in detail in this thesis. A curious reader is referred to previous studies [45,46,47] for research done in turbine disc cooling and sealing.

2.5 Turbine Blade Protective Coatings

Gas turbine components operate under extreme conditions, and are susceptible to hot corrosion, oxidation, thermal fatigue and wear of even the most resilient alloys. This reduces life of the components and increases engine running costs.

Several types of coatings, including transpiration and thermal barrier coatings can aid in protecting turbine blade surfaces. They are often used in conjunction with turbine blade cooling to enhance the effects. Turbine blade protective coatings are however beyond the immediate scope of this project, and are not covered in detail in this thesis.

2.6 Thermochromic Liquid Crystals

Different designs and applications of turbine cooling methods have been reviewed in this chapter. A range of cooling techniques has been examined, but only external film-cooling techniques will be further analysed in this project due to time constraints. Analysis of cooling effectiveness in this study will be limited to the leading edge as to a turbine blade section that is subjected to the most extreme conditions and requires most effective cooling.

Previous studies have recorded temperature changes of a turbine blade model surface, and used a perpendicular mesh to analyse coolant jet structure above the coolant ejecting surface. The following sections will provide a review of the range of methods available for this analysis. This particular section assesses the use of thermochromic liquid crystals.

2.6.1 General Uses of Thermochromic Liquid Crystal

Encapsulated thermochromic liquid crystal (TLC) is a commonly used means of accurately and practically measuring surface temperature of solid bodies. TLC is easily applied by spray-painting and is ready to use when dry. The crystal colour changes to accurately reflect the surface temperature.

Hence the “global” temperature distribution over the entire sprayed surface can be visualised simultaneously. This is the prime advantage of TLC over alternative intrusive temperature measuring devices, such as thermo-couples, which can only provide a “local” temperature measurement at one surface location at any given time. Furthermore, such devices can result in error due to local disturbances, which is not experienced in the use of TLC.

Heat transfer between enclosed solid walls and internal flows can be effectively studied through transparent surfaces, such as glass, or plastic (acrylic, or polycarbonate). The crystals are commercially available, although relatively expensive (approximately £500-600 per 250g can).

2.6.2 Colour Changing Ability of TLC

Early TLC was able to reflect only one colour (usually yellow) to produce a single isotherm [48]. Modern TLC can reflect a range of colours that correspond to specific temperature values [49]. A temperature point, at which the crystal begins to reflect light, is often referred to as *activation temperature*. A temperature point, at which the crystal becomes colourless, is often referred to as *clearing-point temperature*. The temperature range between these two temperature points is commonly referred to as *bandwidth.* The bandwidth may be wide, such as $50°C$ (for *wide-band crystals*), or narrow like $1°C$ (*for narrow-band* crystals) to allow for results of better accuracy.

Frequency of the reflected light from TLC increases with increasing temperature. As such the colours can be seen to pass through the entire visible light spectrum (from red to violet with increasing temperature). This selective light reflection property of TLC is indebted to its *helical molecular structure*. Its illumination by white light results in reflection of light with wavelength equal to the pitch of the helical structure [49].

Temperature indication ability of a thermochromic liquid crystal occurs, when the crystal is in its liquid crystal, or near liquid state. In the solid state, the TLC has the structure of any regular crystalline solid. Upon heating, the crystal molecules go into a state, which has a high degree of orientational and positional order. When it reaches a temperature, which corresponds to a transition between solid and liquid states, molecules lose their positional order while retaining their orientation order (essentially becoming liquid, but retaining its crystalline solid optical properties) [48].

2.6.3 TLC Signal Quantifying Parameters

The TLC signal is generally quantified by either *intensity* or *hue* and can be calibrated using an isothermal surface of known controllable temperature (described in a later paragraph in detail). After calibration, the hue field

produces the surface temperature distribution (thermography), where the peak intensity is related to a particular temperature. One of the proposed representations of Hue was developed by Hay and Hollingsworth [50] and is shown in Figure 2-14 below:

$$h = \arctan\left[\frac{\sqrt{3}(G-B)}{2R-G-B}\right]$$

Figure 2-14 - Representation of Hue

where R, G and B stand for the Red, Green and Blue light components respectively.

As it is known, three light components are required in equal proportions to form a ray of white light, as can be seen in Figure 2-15:

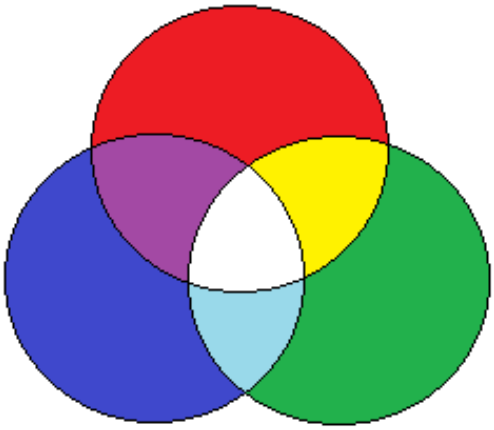

Figure 2-15 - R, G and B Component Mixing to Produce Different Colours

Mixtures of the three base light components in different proportions would result in the formation of other colours. Farina *et al.* [51] suggested a representation of intensity of a given colour as shown in Figure 2-16:

$$I = \frac{R+G+B}{3}$$

Figure 2-16 - Representation of Light Intensity

Hence every colour has a unique value of each of the base components, which can be measured by an RGB camera and transferred into a useful single quantity to describe the colour, such as Hue, or Intensity. An alternative *Saturation* parameter was proposed by Anderson and Baughn [52]. Representation of saturation of a given colour is given in Figure 2-17:

$$S = \frac{\max(RGB) - \min(RGB)}{\max(RGB)}$$

Figure 2-17 - Representation of Saturation

This parameter is essentially a measure of the spread between R, G and B component values and an indicator of the brightness.

2.6.4 Application of TLC onto a Surface

A variety of different types of TLC can be mixed into one solution and applied onto a test surface. Each crystal solution will separately react to its unique activation temperature allowing to visualise a larger range of surface temperatures. Prior to TLC application the surface can also be covered with a thin layer of black paint or ink (approximately 5*μm*) to enhance the crystal colour visibility by increasing the contrast of colours.

The thickness of the crystal layer is of crucial importance. A layer that is too thin would display poor colour and would be difficult to read. While a layer that is too thick would result in undesirable temperature variation across the crystal film, providing inaccurate readings and result in a significant effect on the solid wall heat transfer. A suitable thickness of a TLC layer (typically $15 - 55\,\mu m$) would result in a display of sufficient colour intensity, while having the same surface temperature and heat transfer as the underlying surface.

While it is difficult to directly measure the layer thickness during the process of its application onto the solid wall, the thickness can be assessed and quantified by an electron-microscope photograph (EMP), after it is applied.

2.6.5 Damage from Solvents and UV Radiation

To reduce the irreversible damage and subsequent crystal degradation from solvents and ultra-violent light radiation, microencapsulation is performed [48]. In this process the TLC is shielded in polymer spheres the diameter of $5 - 50\mu m$, the spheres are then mixed with an adhesive binder [51].

2.6.6 Effect of Indirect View

The terms *direct* and *indirect view* of the TLC refer respectively to viewing of the crystals directly and viewing of the crystals through a medium of some form. When the temperature distribution within an enclosed space is to be studied, the TLC must be viewed through a transparent medium, such as a polycarbonate wall. The polycarbonate medium is believed to alter the spectral content of the RGB colour components and consequently shift the hue. Hence it is necessary to carry out indirect-view calibrations for indirect-view experiments. The thickness of the medium must be identical both for the calibration and the actual experiment. The same thickness of TLC and black paint layers must also be maintained in both instances [53].

2.6.7 Effect of Hysteresis

TLCs can give a different hue for the same temperature reading depending on whether they are cooled from above the clearing-point temperature, or heated from below the activation temperature [49]. This difference is known as *hysteresis*. An investigation on a R24C10W TLC has shown evidence of hysteresis, which was characterised by a decrease in the TLC reflectivity and a shift in temperature at which the peak RGB component values occurred [54]. The combination of these effects result in a shift in hue toward lower temperatures when cooled compared with the result when heated. It was also noted that the extent of hysteresis increased when the crystal was heated to a higher temperature, prior to cooling.

2.6.8 Effect of Crystal Aging

Repeated heating of the crystal above its clearing-point temperature has been reported to cause permanent changes to the TLCs [48]. This effect is often referred to as *aging* of the crystals. In particular, a permanent decrease in reflectivity and a shift in temperature at which the peak red and green components occurred have been reported. This change has been related to exposure to high temperatures and it has been noted that the magnitude of this effect was greater for smaller bandwidth crystals.

2.6.9 Crystal Calibration

Prior to use in experimentation it is necessary to calibrate the TLC. Detailed explanation of test surface preparation, as well as subsequent application of TLC can be found in Appendix section 6.1. A prepared test surface with TLC (copper block) is positioned onto a foil heater (figure 2-18). A K-type thermocouple is threaded into the centre of the copper block to provide an accurate reading of the block temperature. The copper block is covered with a transparent polycarbonate block and surrounded by a thermal insulator.

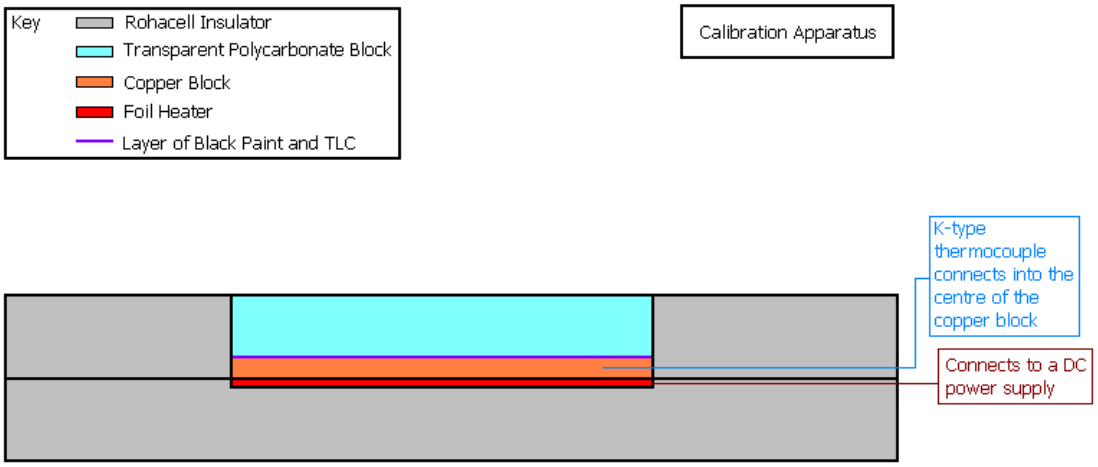

Figure 2-18 - TLC Calibration Apparatus

Figure 2-19 illustrates the calibration apparatus set-up. The block assembly is vertically positioned directly in front of a digital video camera. The camera is connected to the data processing computer.

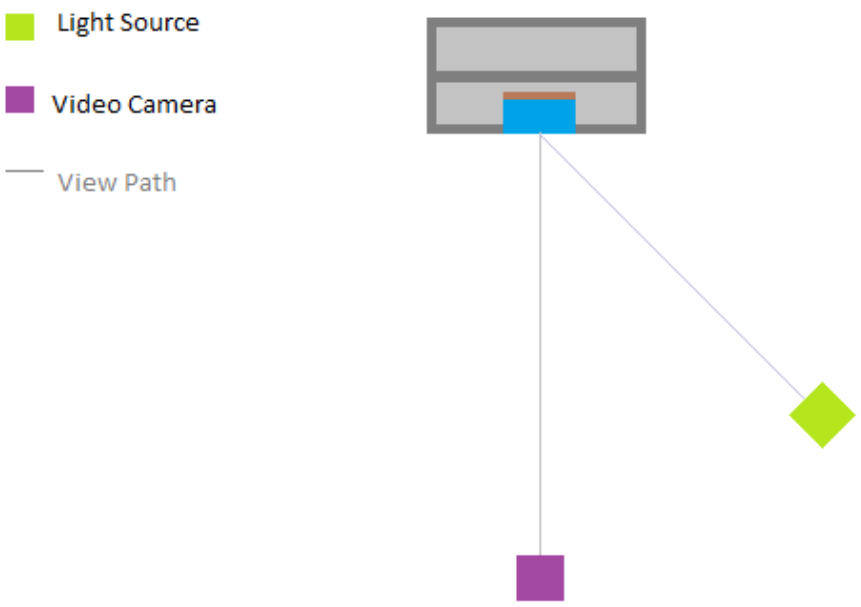

Figure 2-19 - Calibration Apparatus Arrangement (Plan View)

A light source is set-up at an angle to the camera (which can be varied, but is normally around 25°). This set-up minimises the light reflection from the crystals and is referred to as an *indirect-view calibration*.

2.6.10 Normalising a Signal to a Set of Reference Colours

Since colours that appear white under natural light may appear different under an artificial light source, the “white balance” must remain constant during filming. For this purpose, a plain sheet of white paper is placed in front of the camera in a dark room (under artificial light source illumination) for the camera to take its colour as a white benchmark. White balancing is achieved in the camera by focusing on the white background and adjusting the red and blue gains such that their outputs are equal to the green output [52].

2.6.11 Effect of Light Source

It is known that the perceived colour of a TLC depends on the viewing and lighting arrangement, the spectrum of the primary and background light, in addition to the optical properties of the view path (direct view vs. indirect view). Anderson and Baugh [48] used a GE cool white fluorescent light. Although this source of illumination produces white light and appears to have a negligible effect on the TLC temperature, its prime disadvantage is the high UV output [55]. A Spectrum EB-74 UV shield was used on the fluorescent bulb to minimise this effect. Their experimental set-up was then covered with a large black drape in order to reduce the effect of the background incandescent room light.

Since background light may have a different spectral composition from the primary illumination source, the perceived colour will tend to shift toward the colour of the background light. This effect is reduced when light intensity of the primary illumination source is dominant, however running an experiment in a dark room with only the primary light source is still advised for better quality results. A significant fraction of light reaching the camera is reflected by the capsule surfaces of the microencapsulated TLC as gloss (without modification to its spectral content). This reflected light can significantly alter the perceived colour of TLC [51].

Each point in a TLC image effectively has a different viewing and lighting angle - therefore point-, or pixel-wise calibration would yield better results than an entire image-wise calibration of the crystal. In practise, this is a very difficult and a cumbersome situation. To achieve greater accuracy Kakade *et al* [49,53] separated the calibration block image into nine different sectors and measured the hue in each.

A more practical way of eliminating this problem would be to use *illuminant-invariant* on-axis viewing and lighting. This set-up could be reasonably achieved by a ring light source mounted around the camera lens. The image

quality could be further improved by using crossed polarisers on the light source and camera lens to maximise the transmission of the circularly polarised light that is returned by the TLCs and minimise stray surface reflections respectively. Furthermore, the light source should be selected carefully so that it does not alter the temperature of the TLC specimen. An infrared filter may be used for this purpose. Farina *et al.* [51] used a 3200 K white light source with a built-in infrared filter (MHF-150L, Moritex) and a fiber optic ring light guide (MRG61-1500S, Moritex) cross-polarised with the camera lens. Other research groups have reportedly used room lighting, tungsten, halogen, flood lamps, Halolux, Xenon short arc lamp and studio lighting in their experiments [52].

An on-axis set-up is not practical in experiments where a TLC must be viewed through an optical window, which creates light reflections. In this case, uniform lighting can be achieved by using two light sources, symmetrically positioned on the opposite sides of the camera.

2.6.12 Data Processing

During the calibration the block is heated in a dark room under an artificial light source illumination. A digital camera records the crystal colour variation and a MATLAB program transforms this signal into the hue of the specific crystal colour. Different variables, such as the colour intensity, or the hue can then be plotted against block temperature for the heating and cooling processes of the block.

For long-term experimentation, it should be noted that perceived hue from a liquid crystal is not only a function of the spectral characteristics of the source of illumination and the reflecting surface, but also of the sensing device [52]. Hue-temperature calibration is to some extent camera-specific, different hue-temperature curves have previously been reported for the same TLC sample when viewed with different cameras [51].

2.7 Infrared Thermography

The following section of this chapter concentrates on an alternative method of visualising temperature distribution – infrared thermography (IRT). Similarly to the use of TLCs, described in the previous section, this is a non-contact method of surface imaging. It is not subject to conductive measurement errors that are encountered with thermocouples. Temperature measurements can be acquired without disturbing flow patterns around the visualised body.

Contrary to the uses of TLC, IRT does not require application of any materials (e.g. spraying crystals) onto the test surface. It is an effective, two-dimensional temperature measurement technique, which is widely used in heat transfer applications (surveillance, search & rescue, as well as industrial and research applications).

2.7.1 Infrared Sensors

Infrared sensors fall into two basic categories: photon detectors and thermal detectors. In photon detectors, photons are absorbed by a material and interact with its electrons, causing the output of an electrical signal. They exhibit very fast response times and nearly perfect signal-to-noise performance, but require cryogenic cooling and hence are mainly large, heavy and very expensive to produce [56].

The use of thermal detectors as infrared sensors dates back to early nineteenth century, when William Herschel reported a correlation between the time it takes for mercury to rise a set number of degrees and the extent to which it is exposed to invisible light rays [57]. The latter category (thermal detectors) can operate at room temperature without any wavelength limitations. It further benefits from being cheaper than photon detectors, but has a larger response time (millisecond order). For the purposes of this research this response time is deemed to be acceptable, while the economical advantage plays a substantial role in its potential selection.

2.7.2 Effect of Camera Case Temperature

One of the most common thermal detector types is a bolometer. Bolometers essentially measure a change in electrical conductivity. The absorption of incident Infrared (IR) radiation in a bolometer increases the temperature of its thermo-sensing material and causes a change in its electrical resistance. For this reason it is important that the sensing elements are sufficiently thermally insulated. This is usually achieved through using materials with low thermal conductivity, such as porous silicone [58].

Even though the sensing elements of an infrared camera thermal sensor are usually well insulated, some conductive heat transfer from the camera casing is possible if the camera heats-up during operation. Thus larger rates of heat transfer are possible when operating in hotter environments, which would cause the case temperature to rise even further. Therefore the camera case temperature can have a significant effect on the temperature readings.

An IR camera has to be calibrated in order to account for this effect during the experimentation. This can be done by allowing the camera case temperature to heat and cool over a known range of temperatures while observing a test body of a constant temperature.

Some modern cameras use a liquid nitrogen (at approximately $-196℃$) cooled detector [59], or a closed-cycle cryogenic refrigerator [60]. New generation cameras usually come with miniature coolers, which are built into thermal-imaging system and hence do not require additional external cooling.

Schulz [39] reported that low-noise camera operation was ensured by cooling the detector down to about $-193℃$) by a Stirling motor. In contrast to liquid nitrogen cooled scanners, this cooling method allowed unlimited operation.

2.7.3 Effect of Light Sources

Contrary to the use of TLCs, an infrared camera does not require a light source and can operate in any lighting conditions. The experimental set-up may however be shielded from light and have black background to the test surface to minimise stray thermal energy onto detector and increase accuracy of the results [59].

2.7.4 Effect of Test Body Temperature

To calibrate the IR camera, a solid black body can be slowly heated and cooled over a known range of temperatures with Infrared Intensity (IRI) images of the body taken at set intervals. Mori *et al*, used a thermally insulated aluminium plate covered in black paint, equipped with several precise surface resistance temperature detectors for this purpose [61].

It is important to correctly identify the precise skin temperature of the test surface as well as the location at which this temperature is being measured in order to obtain reliable results. During this process a specific IRI value can be acquired for each temperature value. After this process the camera can be used to acquire images of thermal distribution over this body, or a different body that has the same surface thermal emissivity values.

2.7.5 Effect of Thermal Emissivity

The effect of thermal emissivity difference has to be taken into account when the infrared camera is used for imaging temperature distributions over a body of a different material to that used for calibration purposes. This is also true of surface coatings, as different paints can significantly affect the surface thermal emissivity. Thus the camera should be calibrated separately for each necessary test body, or for a range of different thermal emissivity values to analyse how this parameter affects the readings of the specific IR camera.

2.7.6 Effect of Viewing Angle on Directional Emissivity

The emissivity values of a surface change depending on the direction at which it is observed. This phenomenon is known as directional emissivity (ϵ) and it depends on the surface material. Figure 2-20 illustrates these changes.

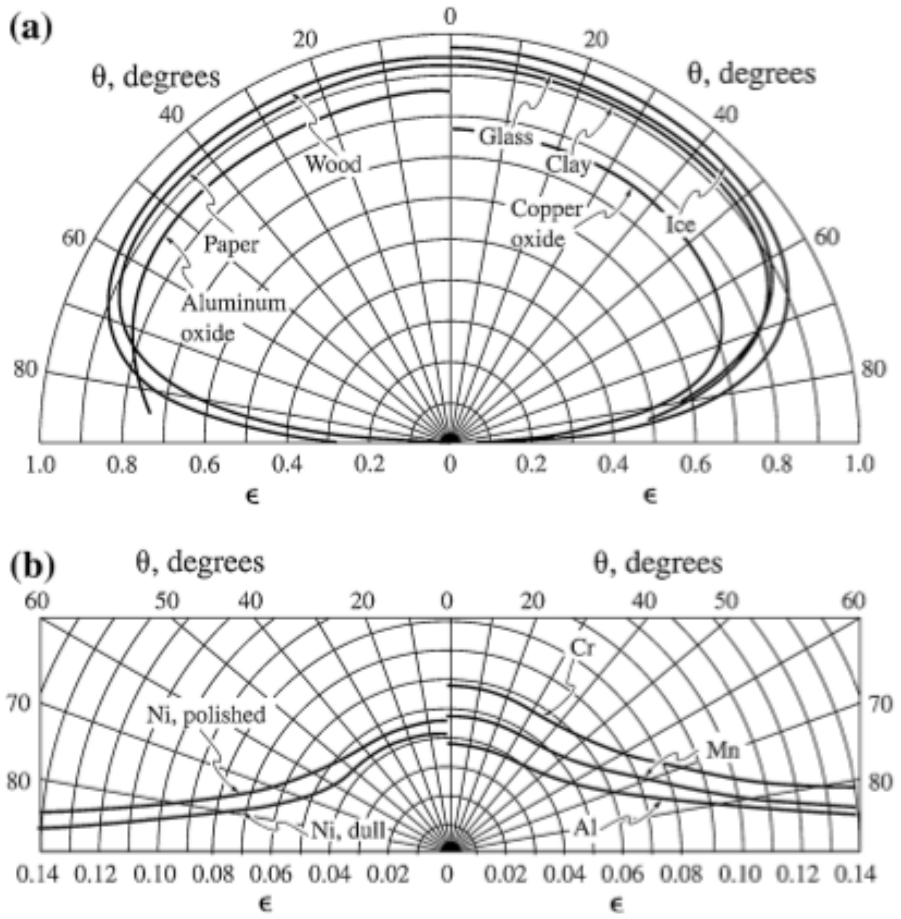

Figure 2-20 – Directional emissivity examples for different materials

The viewing angle is measured in such a way that at 0 degrees the viewed surface is perpendicular to the observer's line of view while at 90 degrees, the line of view is collinear to the observed surface. Figure 2-20 (a) (non-metallic surfaces) [60], shows that ϵ remains high and nearly constant for viewing angles between 0 and 60 degrees. It is general practice to assume that ϵ remains constant over this range of angles for non-metallic surfaces, for example a metal plate covered with black paint [60]. Figure 2-20 (b) (metallic surfaces) shows that ϵ remains low and almost constant between 0 and 40 degrees, and then increases for higher viewing angles.

2.7.7 Effect of 2D mapping of 3D objects

The thermal images are produced as two-dimensional arrays, while observed objects are not always planar and may have complicated three-dimensional shapes. This results in some areas of the visualised surface being observed at different viewing angles by a stationary infrared camera. As discussed in the previous paragraph, this can affect directional emissivity of a test surface.

This effect could be limited by placing the camera further back from the observed surface. However placing the camera further away from the test surface would lead to reduced image resolution and temperature mapping accuracy. Cardonne *et al* used a technique of plotting a 2D image array on a representative 3D model to limit the effect of directional emissivity variation (Figure 2-21 (a) on the left and (b) on the right) [62].

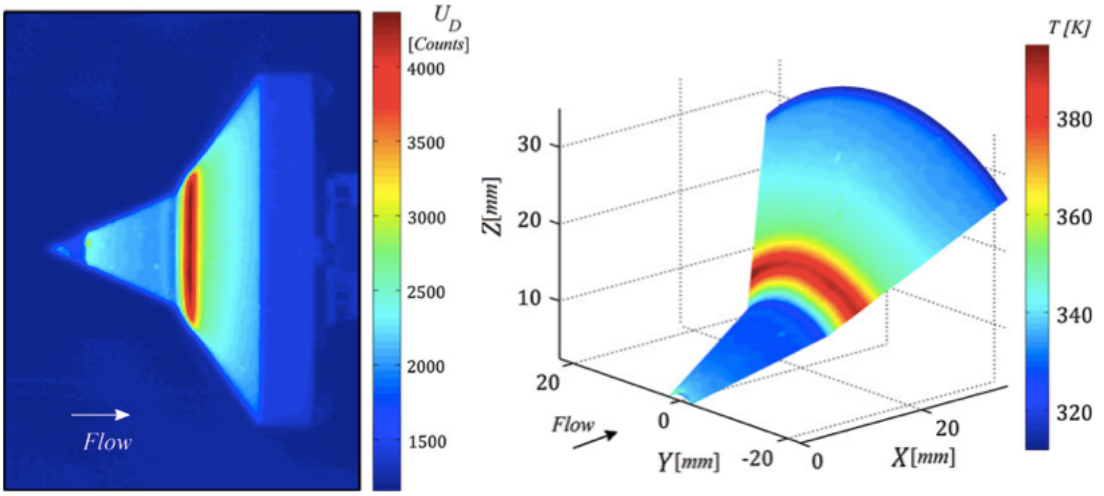

Figure 2-21 - A 2D array (a) superimposed onto a 3D model (b)

Figure 2-21 (a) illustrates a two-dimensional array of Infrared Intensity (IRI), as observed by the infrared camera. A three-dimensional mesh model of the cone was constructed. The IRI, converted into temperature values, together with calculated viewing angles for each segment of the mesh, were superimposed on a three-dimensional model of the cone, as seen in figure 2-21 (b). A similar technique could be used to construct 3D cooling effectiveness mapping over a turbine blade leading edge model for increased results accuracy.

2.7.8 Effect of Lens Distortion

Figure 2-22 [63] illustrates that lens distortion normally divides into pincushion, or barrel distortion. Distortions appear due to magnification tendency of optical lens and largely depend on their geometry.

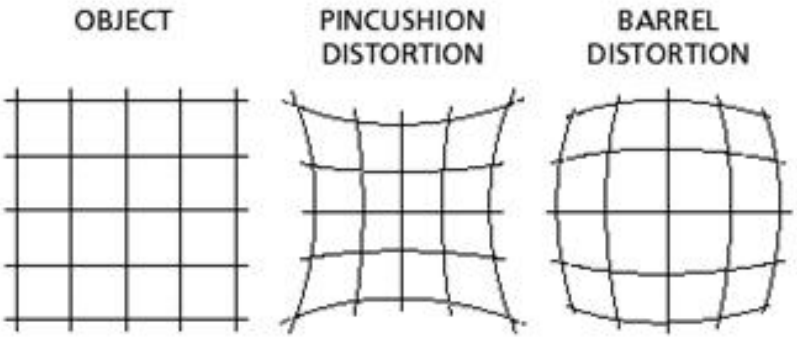

Figure 2-22 - Illustration of the camera lens optical distortions

Cardonne *et al.* [62] have taken this factor into consideration during the programming stage and used a filter, which moved the distorted image coordinates in place of ideal image coordinates to minimise this effect.

2.7.9 Data Processing

An IR camera observes electromagnetic energy radiated by a body in the infrared spectrum and converts it to an electronic output signal. The signal, in the form of a two-dimensional image is essentially a map of the IRI distribution over the visualised surface. As the camera measures IRI at the body's surface and displays the image as an array of pixels, the map can be described as an array of square body skins, each with a distinct IRI Value.

It is possible to design algorithms to transform the IRI value of each pixel into a corresponding temperature value. These codes could be written in MATLAB.

2.7.10 Image Quality Enhancement

Various numerical filtering techniques can be used in the data processing code to enhance the received image quality and improve the spatial resolution of a digital image. It can also reduce the noise effect and can be based on local mean and variance of the two dimensional arrays [64].

Alternatively, the camera should be placed closer the test surface, or if the experimental procedures do not allow this practice – then a series of external lenses, and/or magnification mirrors can be used in order to enhance the image resolution [65].

2.7.11 Effect of Indirect View

Under certain circumstances it is necessary to separate the IR camera from the test surface environment. For example the visualisation of turbine blade film cooling in hot mainstream flow within a turbine test rig. The turbine blade can be made visually accessible to the infrared camera via a transparent window. In this way the camera would not affect the gas flow within the test rig and would not be heated by the mainstream flow.

Not every material is suitable for production of such a window, due to limitations in transmissivity of IR radiation from the test body to the detector. Suitable materials include Zinc Selenide (ZnSe) infrared windows [30,59,66], NaCl optical portholes [30], or Sapphire windows [39] due to their high transmittance and high temperature resistance. The perceived IRI output of the camera could then be used to calculate surface temperature of the visualised body, however the window transmissivity must be taken into account during this calculation in addition to the measured camera case temperature, ambient temperature and emissivity of the visualised body [59].

If the camera is used to visualise a test surface through an indirect view during the experimentation, it should also be calibrated by visualising a black

body of known temperatures through an indirect view (with the same medium). It should also be noted that thickness of the window can displace the image when it is observed by the camera through the window under oblique angles due to effects of refraction.

2.7.12 Calibration Accuracy

The accuracy of thermal distribution measurements depends on careful calibration of the camera for the specific test surface, in addition to how much noise is present in the acquired image. Assuming that a precise calibration procedure has been carried out, it is possible to reduce the measurement uncertainty to a minimum of 1-3% of measured values in some studies [61].

Sweeney and Rhodes studied film-cooling effectiveness over a flat plate through a Zinc Selenide infrared window and reported an accuracy of surface temperature measurement of $\pm 4℃$ [66].

Ekkad *et al.* [67] used IRT to obtain film cooling effectiveness and HT coefficient measurements. A half-cylinder model with a flat afterbody was tested in a wind tunnel with heated mainstream. A single inclined coolant hole with ejecting cold coolant gas was visualised. A cooled FLIR Systems ThermaCAM SC 3000 with an estimated camera uncertainty of $\pm 2℃$ was used. An overall experimental uncertainty of $\pm 4.5\%$ and $\pm 7.0\%$ in calculating the HT coefficient and film-cooling effectiveness was reported.

Lu *et al.* [37] used IRT to obtain film cooling effectiveness. A FLIR Systems ThermaCAM SC 500 with a camera uncertainty of $\pm 2\%$ or $2℃$ was used. The film cooling effectiveness was measured to an uncertainty of $\pm 5\%$

Six BR values have been tested ranging from 0.25 to 2.0. The highest cooling effectiveness coverage appeared to occur between BR of 0.5 and 1.0. Jet lift-off was reported at higher BR values [67].

2.7.13 IRT and Flow Visualisation

Infrared thermography has been widely used by research groups for many years. A study by Carlomango *et al.* [65] has used IRT for flow visualisation on various different surfaces (including delta wings, rotating discs, and others). The study was able to use IR imaging to obtain convective heat transfer (HT) coefficients and to analyse structures of vortices, as well as other flow patterns across the test surface. Similar works and results have been reported in many other papers [60,68,69,70].

Research groups using IRT for acquisition of convective HT coefficients on a rotating rotor-blade [61], or a rotating disc [65] have demonstrated the feasibility of turbine components analysis in real dynamic environments. Hence IRT can be applied to studies of turbine disc cooling and sealing.

2.7.14 IRT and Boundary Layer Analysis

Locations of boundary layer separation and reattachment to the surface can be detected from pressure measurements around the surface. This process relies on intrusive probes. Such measurement techniques can invalidate experimental data, particularly when dealing with highly sensitive boundary layers at low Reynolds numbers.

Desideri *et al.* [71] conducted IRT experiments on a Fokker aerofoil in a heated mainstream flow to analyse boundary layer formations. It has been outlined that heating the test surface, or the flow can aid in visualising precise locations of boundary layer separation and reattachment. This was attributed to the HT coefficient changes in laminar or turbulent flow. Clear temperature gradients were observed on the transition boarders over a solid body, which look like cold and hot fronts.

2.8 Other Visualisation Techniques

Thermochromic Liquid Crystals and Infrared Thermography are established and widespread methods of acquiring adiabatic effectiveness distributions. Both techniques use surface temperature measurements to estimate the effectiveness values and are known as heat transfer measurement approach methods. A less common, but increasingly popular method of effectiveness value acquisition is a Pressure Sensitive Paint (PSP). PSP measurements rely on mass transfer analogy in which mass concentration measurements of a tracer gas near the wall are related to adiabatic wall temperature [72].

PSP is an organic product with luminescent molecules sensitive to oxygen concentration that emit light when excited. Ahn *et al.* used an Argon ion 488nm wavelength laser to illuminate a PSP coated surface [36]. The intensity of the emitted light depends on the local value of oxygen concentration: the intensity increases as the oxygen concentration in the binder around the sensitive molecules is decreased. This phenomenon is called “oxygen quenching”. Using air for the mainstream flow and a tracer gas without molecules of oxygen for the coolant flow (e.g. pure nitrogen), the effectiveness can be evaluated by measuring the oxygen concentration near the test surface [72].

Ahn *et al.* [36] used PSP to measure detailed film cooling effectiveness distributions in the leading edge region of a gas turbine blade with three showerhead rows. Effectiveness uncertainty of $\pm 7\%$ was reported (arising from $\pm 5\%$ uncertainty in the partial pressures of oxygen). Li *et al.* [35] used PSP to study the effect of coolant density on leading edge showerhead film cooling and reported a maximum uncertainty of 9% for low effectiveness values (which decreased for higher effectiveness values). Caciolli *et al.* [72] compared PSP and TLC techniques to measure adiabatic effectiveness of a multi-perforated plate, simulating a film-cooled combustor liner. PSP measurement uncertainty ranged from +/-10% for low effectiveness of 0.2% to +/- 2% for effectiveness values higher than 80%. TLC uncertainty was +/-5%

[72]. PSP was reported to benef from high resolution images and minor experimental uncertainty. This methods requires high capital investment (optical hardware: filter lens, UV illumination system, and scientific grade camera), significant running costs (depletable foreign tracer gas), and is limited by the finite amount of stored tracer gas. TLC benefits from comparitatively lower cost of experiments, but requires significantly more time for data acquisition and post processing [72]. The PSP was proved to be the superior steady state method to estimate adiabatic film cooling distributions with high resolution results obtained in critical regions such as: near the walls, around the effusion holes and in the wake generated by the dilution hole itself [72].

Alternative visualisation techniques include Temperature Sensitive Paints and the ammonia-diazo technique. The later requires coating a surface with chemicals – diazo paper that react with the cooling flow which has been seeded with gaseous ammonia and water vapour. This process results in a reaction leaving traces of various darkness dependent on concentration of coolant and enabling to estimate effectiveness. PSP, TSP, as well as ammonia-diazo technique will however not be covered in more detail in this thesis due to the time limitations.

2.9 Comparison of Visualisation Techniques

In this section advantages and disadvantages of TLC and IRT are compared. The reasoning for choosing IRT as the flow visualisation tool for turbine blade cooling analysis is also outlined.

2.9.1 Calibration

Calibration test surface can be prepared faster for IRT than for TLC. Viewing angles up to the value of $60°$ have no significant influence over the results, contrary to TLC experimentation. No light source is required for IRT experimentation, in fact it is preferred (but not essential) to conduct experiments without light and with black backgrounds to minimise stray infrared radiation emitted onto the detector. IR camera case temperature must be simultaneously recorded, but many more parameters must be taken into account in TLC calibration however.

2.9.2 Application

TLC – requires spray-painting a test surface with crystal solution. This can be time-consuming and relatively expensive if the test surface is large. Crystals can deteriorate and be damaged by the UV (e.g. from sun light and artificial light sources) and solvents. The crystals also age with time and require regular removal and re-application if the experiments are conducted for a prolonged period.

IRT – only requires setting of the camera in a suitable position, which is immediately ready for the experimentation. It is expected to produce constant results regardless of the time of operation.

IRT is therefore faster and simpler to set-up than TLC and does not require maintenance during prolonged experimentation. IRT running costs are

significantly lower than for TLC. IRT however requires significant initial investment, depending on the camera type.

2.9.3 Accuracy of Temperature Measurement

Narrowband TLC can produce results of high accuracy (typically $\pm 0.1℃$) over a narrow temperature range (e.g. $1℃$). A wider bandwidth crystal can cover a larger temperature range with reduced accuracy. Few TLC coatings with crystals of various narrow bandwidths can also be mixed. TLCs are normally destructible at temperatures above $100℃$.

Accuracy in the range of $\pm 0.55℃$ to $\pm 4.0℃$ has been reported for IRT. Higher accuracy cameras require higher initial investment. An IR camera can have very large temperature measurement range (approximately $-50℃$ to $2000℃$ with optional filters [67]).

Therefore IRT has a larger operational temperature range, but a reduced accuracy in comparison to narrowband TLC measurements.

2.9.4 Data Processing

Both TLC and IRT require construction of numerical algorithms, such as MATLAB codes to convert the raw experimental data into temperature, or cooling effectiveness distribution plots. TLC hue measurements are subject to hysteresis and can differ for the same temperature depending on whether the test surface is cooled or heated. This phenomenon must be taken into account during TLC experiments, but is not applicable to IRT.

2.9.5 Selection of the Optimal Visualisation Technique

Having reviewed advantages and disadvantages of TLC and IRT it can be summarised that IRT is superior to TLC technique in the following parameters:

i) IRT has significantly lower running costs (limited simply to power consumption of the equipment).
ii) TLC crystals vary in price, but require continuous removal and re-application of crystals onto a test surface for prolonged experimentation. This can be expensive and time consuming.
iii) IRT is faster and simpler to calibrate, set-up and operate than TLC.
iv) IRT can be operated over a significantly larger range of temperatures and can acquire temperature distribution plots over a surface at ambient temperature, which is difficult to achieve using TLCs.
v) Viewing angles up to the value of 60 degrees have no significant influence over the results, contrary to TLC experimentation.
vi) No light source is required for IRT experimentation
vii) IRT is not subjected to hysteresis

TLC measurement supersedes IRT in the following parameters:

i) TLC technique can provide better image resolution.

This is a significant factor, however various numerical filters can be used to enhance the spatial resolution and image quality of IR images, as it has been discussed in this chapter.

ii) TLC can yield higher accuracy results, but over narrow temperature ranges.

This is deemed as the most significant factor. Careful calibration of IR camera should limit experimental uncertainties to a minimum, but they are still

expected to be greater than for TLC. This research includes visualisation of a cylinder model - the viewing and illumination angles around its circumference would vary when observed from a fixed camera location. This would introduce uncertainties in TLC measurements. This problem is practically eliminated in IRT - therefore choosing IRT for this particular task could yield better overall experimental accuracy than TLC measurements.

iii) High initial investment into the IR camera is required. The investment varies depending on the camera choice, and is higher for greater accuracy cameras.

This investment could pay-off over a prolonged period of IR exploitation in comparison to continuous use and replacement of TLC. The associated time saving factor of IRT use over TLC technique is also important.

IRT is preferred over the TLC technique for the advantages it offers in flow visualisation. The associated disadvantages have been taken into account and their potential solutions stated.

2.10 Literature Review Conclusion

Previous sections have outlined that increasing efficiency of turbine cooling designs can yield greater power output or a reduction in fuel consumption in gas turbines. Improved imaging techniques can help improve turbine analysis and therefore aid in this development. Various technologies can be exploited to analyse cooling effectiveness and their review has been performed.

Two non-intrusive thermal imaging techniques (TLC and IRT) have been considered and analysed in depth. Their advantages and disadvantages have been compared. The reasoning for choosing IRT as the flow visualisation tool for turbine blade cooling analysis has been outlined.

The scope of this study – assessment of applications and limitations of IRT in turbine cooling visualisation has been previously defined. The objective is to perform this assessment and outline the potential, as well as limitations of IRT in design of improved turbine cooling visualisation techniques.

Previous experimental studies of turbine cooling effectiveness have been considered. Their experimental methodologies have been analysed and will serve as a basis of designing an improved IRT methodology of this study (detailed in the next chapter).

A turbine blade leading edge with showerhead configuration film cooling will be modelled. IRT will be used to analyse leading edge film cooling effectiveness and visualise coolant distribution both at the model surface, as well as above it. The obtained conclusions would be used to analyse limitations of IRT in turbine blade cooling visualisation and assessed for potential analysis applicability of other turbine components.

3 Experimental Methodology

The main objective of this project was outlined as experimental assessment of limitations and applications of Infrared Thermography in Turbine cooling visualisation. For this purpose a cylinder with coolant ejection holes in showerhead configuration was constructed to model a turbine blade leading edge. The model with heated coolant was operated in a cold-mainstream wind tunnel. An infrared camera was used to record images of coolant trajectories at the cylinder wall and above it (captured by a perpendicular fine nylon mesh). The experimental set-up, camera calibration procedure and data processing techniques are discussed in this chapter in detail.

3.1 Wind Tunnel Experimentation

A number of experiments were conducted in a low-speed wind tunnel at mainstream velocities of 10m/s. The tunnel has a diameter of 0.77m and a 1.15m long open test section. The following section concentrates on a description of the apparatus used during the wind tunnel experiments.

3.1.1 Cylinder Model Description

The model (Figure 3-1) used in this project was similar to that used in the study by Reiss and Bolcs [20], and was based on a Rolls Royce turbine blade. Essentially it is a hollow Perspex cylinder with a plenum chamber. A 3mm thick layer of a Rohacell insulation covered the inside and outside of the cylinder. The conductivity of the insulator was approximately 0.04 W/ m K, ensuring minimal heat transfer. The outer Rohacell layer was spray-painted with the same black paint as the copper block used in the camera calibration.

Similarly to a study by Mee *et al.* [22], a ‘cold mainstream – hot coolant’ arrangement was used in this work. The air of a controlled temperature was pumped into the plenum chamber and ejected out of the cylinder as the

Figure 3-1 - Cylinder Model

coolant flow. The coolant cylindrical channels were drilled through the cylinder wall at an angle of $45°$ to the cylinder surface. The $\pm 20°$ and $\pm 40°$ coolant ejection hole lines were angled at $30°$ to the mainstream direction of flow (figure 3-2 – not to scale [7]):

The coolant hole pitch/diameter ratio was 3.7, while the coolant hole/cylinder diameter ratio was 0.05. The cylinder diameter was 240mm and the

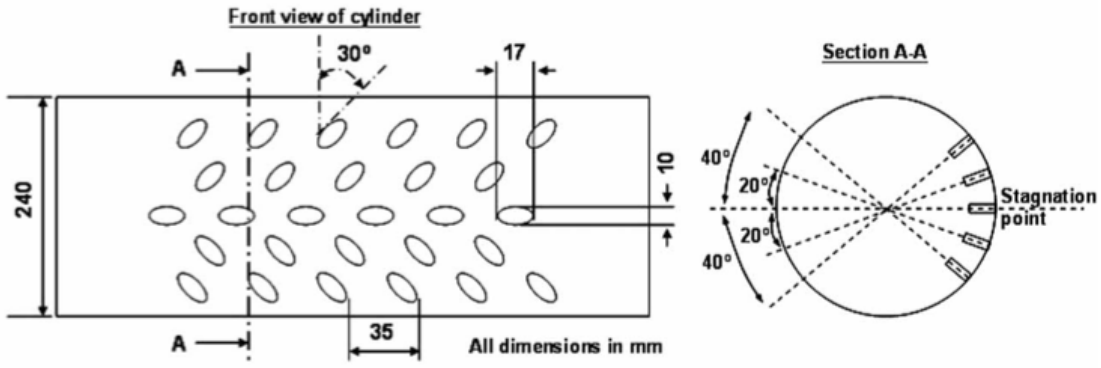

Figure 3-2 - Coolant ejection hole geometry

experimental Reynolds number (based on the cylinder diameter) was approximately 150 000. The Reynolds number was similar to that used in the study by Reiss and Bolcs [20]. The plenum chamber, coolant passages, as well as the external cylinder surface were considered adiabatic.

The central coolant ejection hole row was set to be on the stagnation line of the cylinder, facing the mainstream flow. Air was drawn at room temperature by the air pump (figure 3-3), supplied to the mesh heater (figure 3-4) where it was heated to the desired temperature (30℃-60℃) before being supplied to the plenum chamber of the cylinder (figure 3-5) and exiting through the ejection holes.

Changing the pump power settings varied the rate at which air was supplied to the cylinder. The temperature was recorded inside the heating channel and sent as a feedback signal to the temperature control unit to ensure coolant temperature was maintained at a constant value. A thermocouple was positioned inside the cylinder. The thermocouple signal was taken as the coolant temperature directly before it left the plenum chamber.

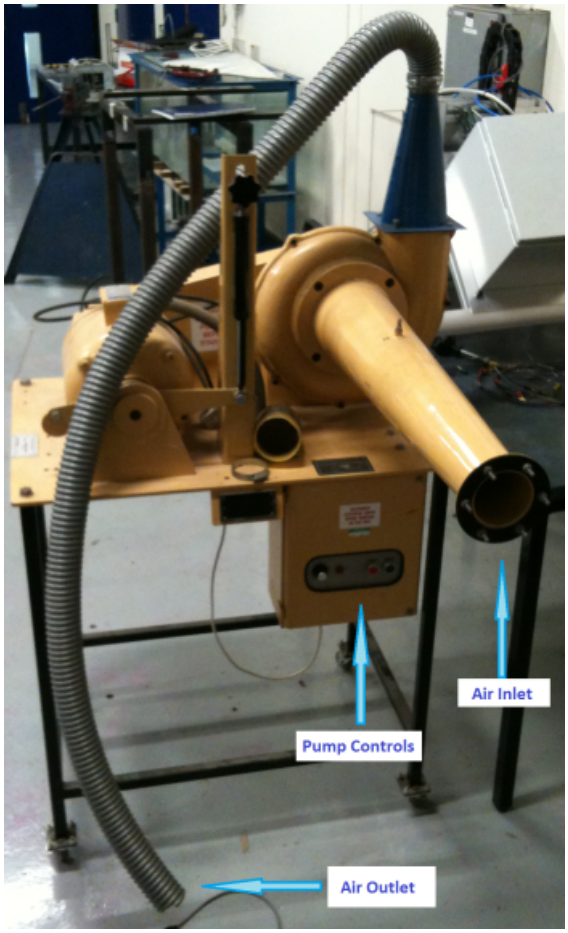

Figure 3-3 - Coolant pump

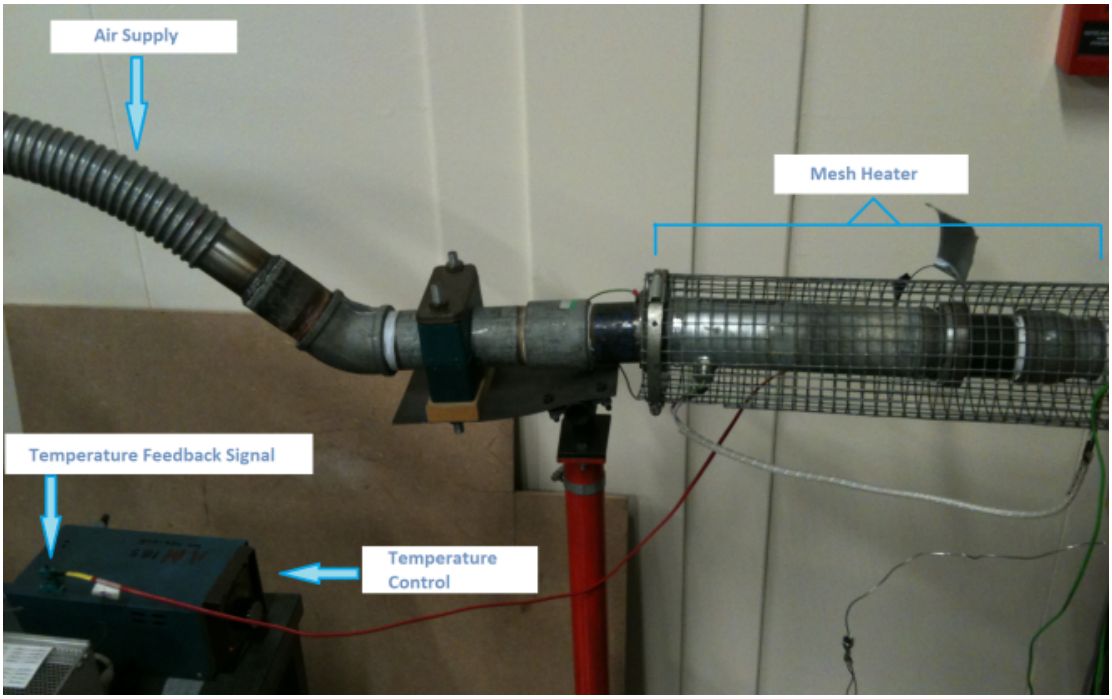

Figure 3-4 - Mesh heater

Figure 3-5 - Cylinder test platform

The entire test platform was elevated to a height such that the stagnation line of the cylinder is level with the centreline of the wind tunnel.

3.1.2 Temperature and Pressure Readings

Figure 3-6 illustrates the cylinder surface, as well as the coolant and mainstream flow conditions. The plenum chamber temperature has been taken as the coolant total temperature condition. The densities of the coolant and oncoming mainstream flow are assumed to be equal, as it is essentially air drawn from the same environment at relatively low velocities and modest temperature difference.

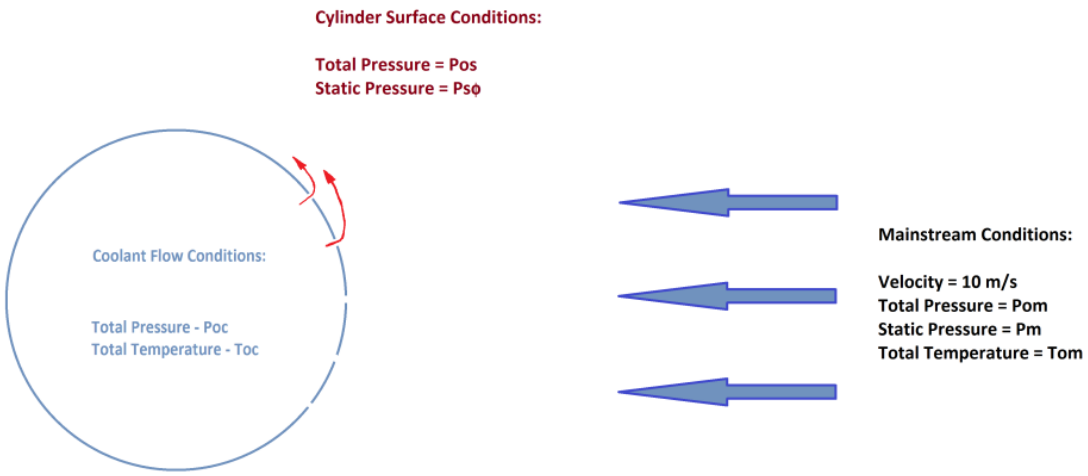

Figure 3-6 - Flow conditions

Temperature of the wind tunnel airflow was measured by a thermocouple and used as the mainstream total temperature condition. A Pitot-static tube was used to measure the mainstream velocity in the wind tunnel. The wind tunnel speed was set at a constant level of 10 m/s throughout the experiments.

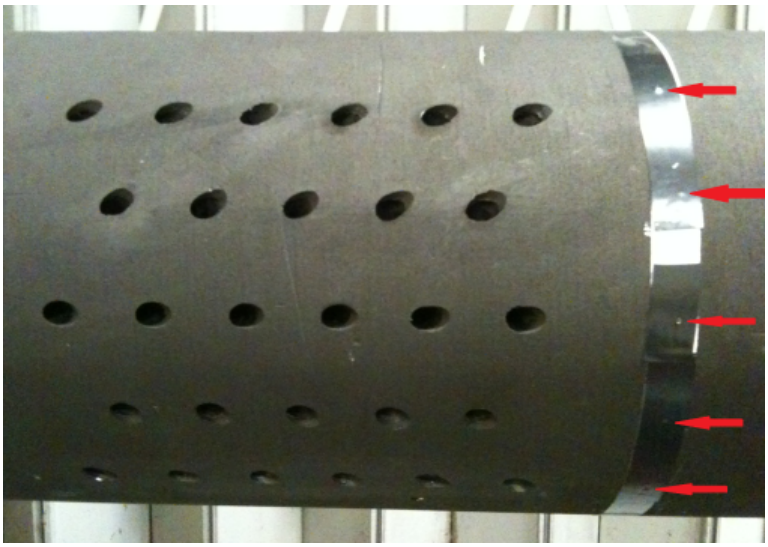

Figure 3-7 - Pressure taps

A pressure tapping was connected to the inside of the cylinder plenum chamber to record total pressure inside the cylinder. A series of further 14 pressure tap holes were located around the entire circumference of the outer cylinder area. Figure 3-7 shows five of the pressure taps, identified by the red arrows. The pressure taps were covered with a black smooth insulating tape (with a series of holes to allow pressure readings). This was done to minimise the friction between the flow and cylinder wall.

The model was assembled in a way, which allowed rotation of the cylinder. Thus the zero degree line along which the central row of the coolant ejection holes was located could be inclined at a selected angle to the horizontal. The cylinder could then be fixed in that position. By rotating the cylinder at five-degree increments, it was possible to use the fourteen pressure taps to record the static pressure distribution around the entire surface of the cylinder.

Temperature and pressure conditions for the cylinder surface, coolant and mainstream flow, were fed to and recorded by the data acquisition unit.

3.1.3 Nylon Mesh Selection

The fine nylon mesh used in this study has a honeycomb structure with the hexagon width of approximately 2mm, while the mesh material thickness was less than 0.2mm. This mesh (referred to as the Oxford mesh in Chapter 2) was selected due to the low material thickness, in order to minimise flow disturbance. It was also selected for its low thermal conductivity. Thus conduction along the mesh fibres was negligible compared to the heat convected from the flow and hence the mesh temperature was assumed to be equal to that of the flow.

3.1.4 Nylon Mesh Location

The coolant plumes were visualised above the cylinder surface on a nylon mesh, positioned perpendicularly to cylinder surface (figure 3-8). The mesh was tailored and glued onto a special fence to minimise its deformation during the experiments. The fence was produced from 4mm diameter aluminium bar.

Figure 3-8 - Perpendicular nylon mesh

In order to secure the mesh perpendicularly to the cylinder and prevent it from moving in the wind tunnel during experiments, the fence has been fixed in its position with a number of strings. In order to prevent in from bowing near the cylinder surface, the legs of the mesh fence have been stretched away from each other (notice the difference in bowing near the cylinder surface between figures 3-8 and 3-9). The minimum distance between the mesh and cylinder surface was reduced to approximately 2 millimetres.

Figure 3-9 - Stretched nylon mesh

The circumferential location of the mesh on the cylinder was measured from the trailing edge of the $-40°$ ejection holes row. A non-dimensional x/d distance was used for defining the mesh location, where *x* denotes the distance aft of the trailing edge of the coolant ejection holes, while *d* denotes the hole diameter, which was taken to be 10mm. During the experiment, the mesh was located at these non-dimensional distances:

5, 3, 1, -1

Thus the mesh has been positioned at three locations aft the $-40°$ hole row and at one location $(x/d = -1)$ aft the $-20°$ hole row only (on the border of the $-40°$ hole leading edges). In order to position the mesh in these precise locations, a strip of masking tape was used with those distances marked on its surface. The masking tape was wrapped around the curving cylinder surface to identify along which line the mesh fence should be stretched. As this was done for distance measurement only, the masking tape was always removed prior to the experiment initiation.

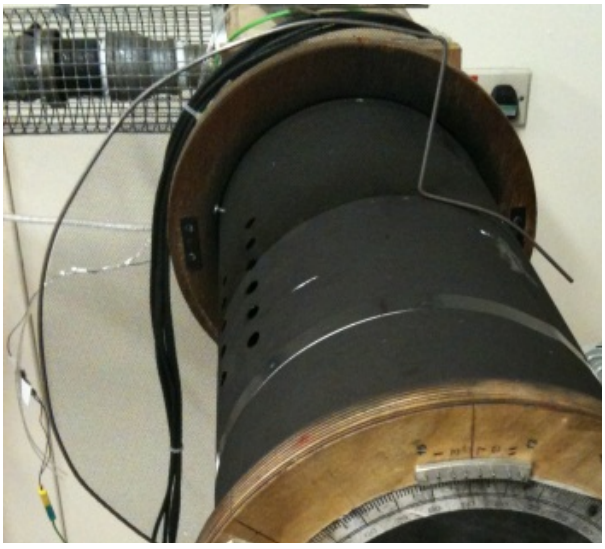

Figure 3-10 - Lateral mesh

Visualisation of the coolant plume trajectories on a lateral mesh (figure 3-10), were considered, but not realised, as it has been determined that the lateral mesh frame significantly distorts the mainstream flow and thus has an influential effect on the coolant plume trajectories.

3.1.5 The Infrared Camera Specifications and Set-up

The camera chosen for the project was a FLIR Systems Thermovision Micron / A10 camera by Indigo Operations (figure 3-11 [73]). It is a long-wavelength (7.5-13.5 microns) uncooled microbolometer camera. The operating case temperature range is between 0 and 40°C. The camera is capable of producing images of an object at temperatures of up to 500°C, however it will be operated in a low-temperature (high sensitivity state). In this state it is only able to produce images of objects up to a temperature of 150°C, which is sufficient for the purposes of this experimentation.

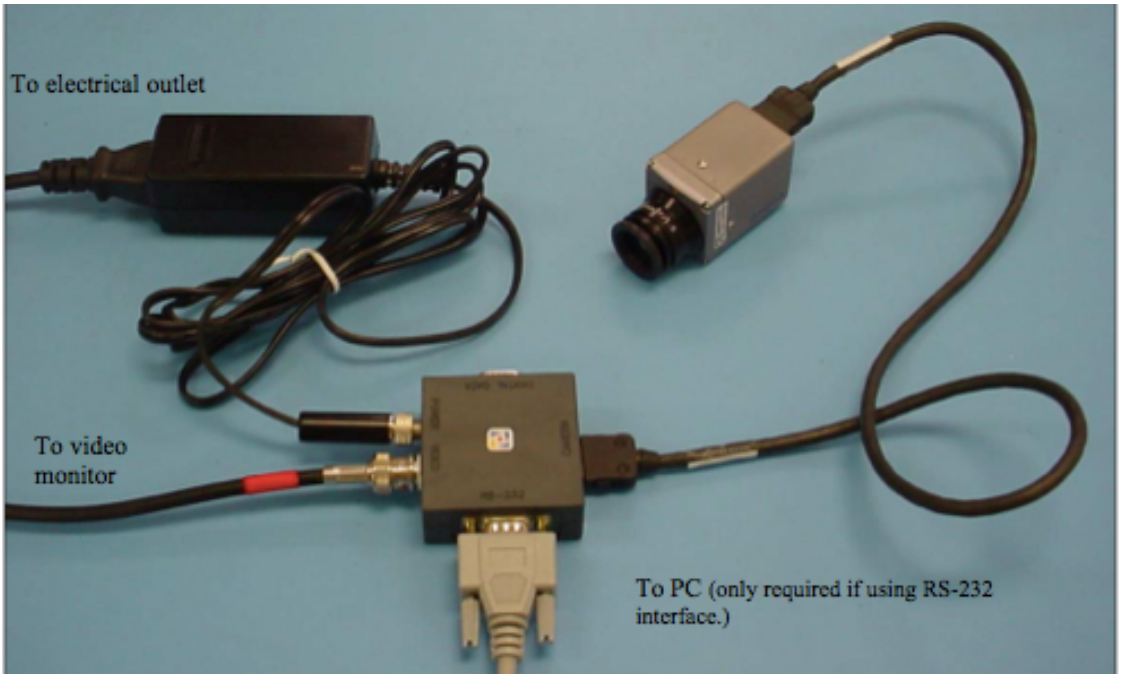

Figure 3-11 - Camera Set-up

The camera software allowed acquisition of raw infrared images to visualise the observed surface and hence adjust the camera into a suitable position prior to the start of an experiment. During wind tunnel experiments its position was chosen to produce good resolution images, while not affecting experimental results. The camera was located ahead and below the cylinder to visualise the cylinder leading edge, without distorting the free stream flow over the cylinder. The camera was directed perpendicular to the surface, with a clear vision of the $-40°, -20°$ and $0°$ ejection hole rows.

The nylon mesh was fixed to the model surface at the previously discussed locations around the cylinder circumference. A different camera location was used for each mesh position. The camera was positioned underneath the model surface and pointed at a perpendicular angle to reverse side of the mesh (the camera was located aft of the mesh in the mainstream flow).

3.1.6 Experimental Procedure

The experimental apparatus (including the IR camera) within the wind tunnel was shielded from background light. The wind tunnel top section was covered with black painted MDF sheets to shield the apparatus from ceiling lights. The concrete laboratory floor (painted in glossy blue paint) was covered with black cloth sheets in order to minimise light reflections. The wind tunnel sides were covered with black drapes to further shield the apparatus from background light. The drapes were stretched and fixed to prevent them from flapping during the experiments. Any lights that could cast light onto the camera or turbine blade model were switched off. Large boards were placed near the wind tunnel to shade the apparatus from any stray light coming through laboratory windows.

After camera set-up, trial images were taken to ensure that they were of good resolution and fully captured the test surface area of interest. Once the camera was switched on it started to heat up. Switching the wind tunnel to the required setting and allowing it to run for approximately 15 minutes allowed the mainstream flow and IR camera case temperature to stabilise.

With the wind tunnel and IR camera stabilised, the coolant flow pump was switched on and the desired coolant temperature was set. All experiments were started at the maximum pump power setting. With this power setting set, the coolant mass flow rate was at its highest and three further minutes were allowed for the coolant temperature to stabilise. The infrared camera framegrabbing software was switched on and the camera proceeded to take raw IR images of the test surface. Ten frames (ten raw IR images) of a test

surface were taken at 20 second intervals. Once the framegrabber took the last image, it automatically closed and the coolant setting was lowered. The coolant flow was again allowed to stabilise before repeating the procedure for the new coolant flow setting. Each experiment was repeated for fourteen power settings, totalling at least 140 frames per experiment. In total all the experiments (four mesh locations and cylinder surface visualisation) produced more than 700 frames of raw images for processing.

3.2 Calibration of the Infrared Camera

In order to use the infrared camera in experimentation, it is necessary to calibrate it. This procedure requires:

1. Preparation of a test surface.
2. Assembly of the calibration apparatus.
3. Performance of the calibration test.
4. Data processing.

For the scope of this project two types of test surfaces were selected for the purpose of calibrating the infrared camera. These were a black solid body (copper block covered in black paint) and a black nylon mesh.

3.2.1 Calibration Block Preparation

A clean 67mm x 67mm x 5mm copper block was uniformly spray-painted with Hallcrest BB-G1 Black Coating (figure 3-12). A pre-drilled narrow channel in one of its sides allowed threading of a thermocouple to record temperatures at the centre of the block. Detailed description of the black test body preparation can be found in section 6.1 of the Appendix (steps *i-ix*).

Figure 3-12 Copper Block

3.2.2 IR Camera Calibration on a Black Solid Body

Figure 3-13 illustrates the equipment set-up for calibration of IR camera on a black solid body (copper block).

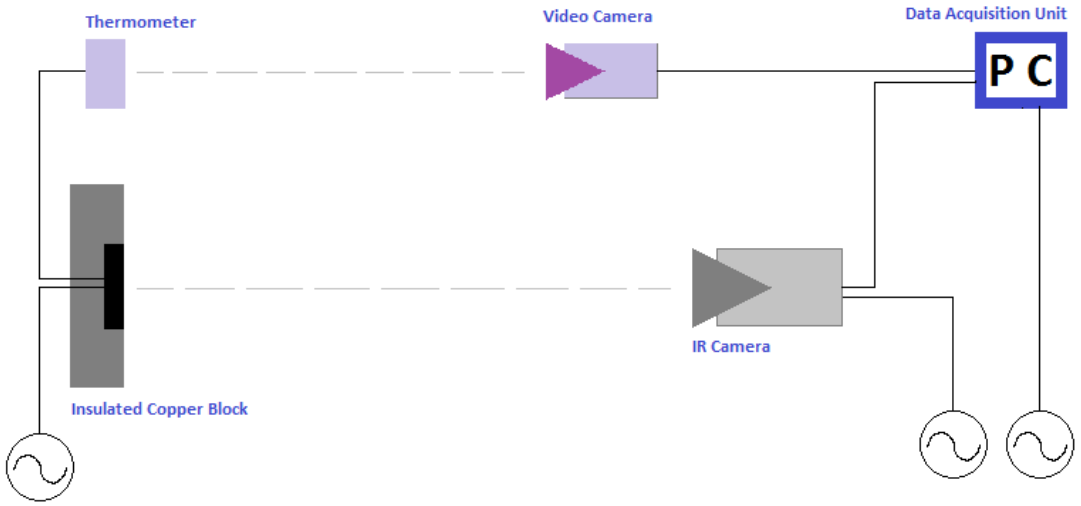

Figure 3-13 – Camera calibration on a black solid body

The camera was positioned on the same vertical level and pointed at a perpendicular angle towards the copper block to record its IR raw images. The copper block with a threaded K-type thermocouple (figure 3-14 right) was positioned on a foil heater (figure 3-14 left). The heater was connected to an adjustable power supply, enabling a controlled heating rate (figure 3-15).

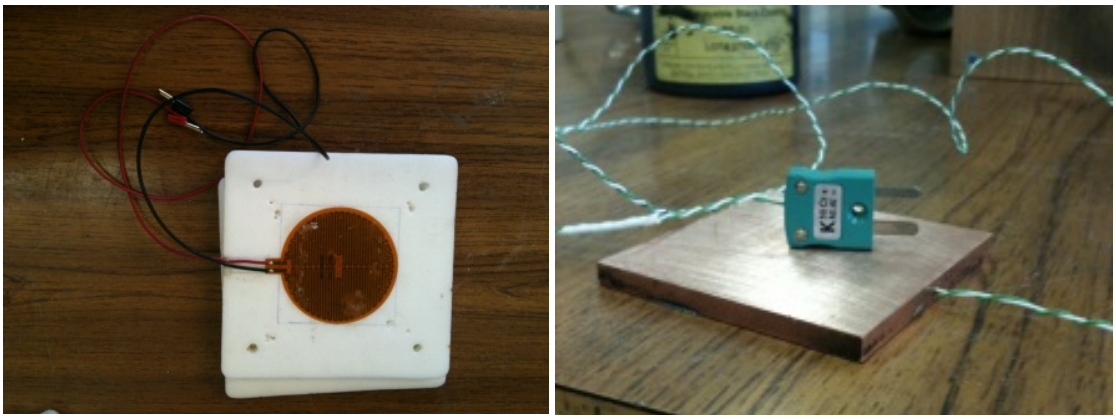

Figure 3-14 – Foil Heater in Rohacell (left), K-type Thermocouple (right)

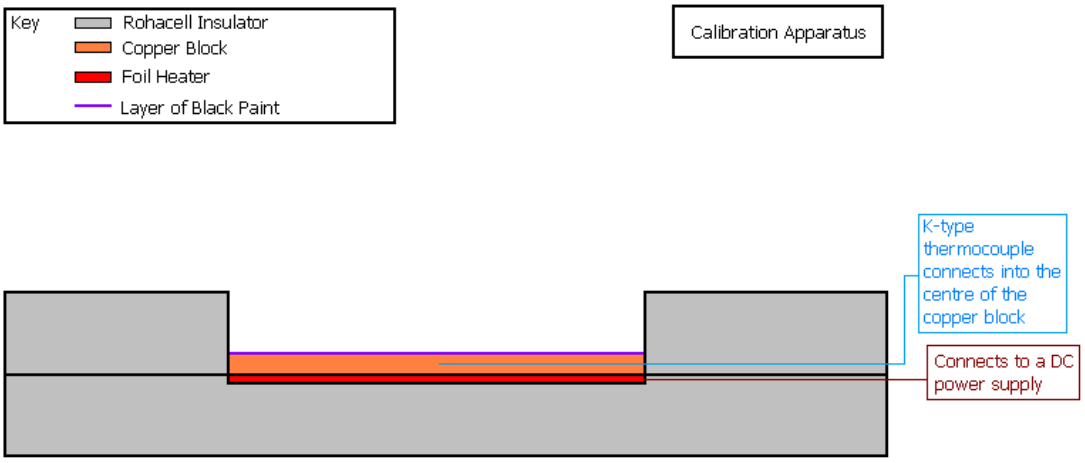

Figure 3-15 - Copper Block Calibration Apparatus

The distance between the copper block and the IR Camera was adjusted to ensure that the entire block surface was clearly visible on the IR raw image. The block was located as close as possible in order to achieve images with the highest resolution, while heat transfer by radiation from the copper block was not sufficient to affect the camera case temperature. In practice the optimal distance was found to be approximately 30cm.

Figure 3-16 demonstrates an example of an IR raw image of the hot copper block in a Rohacell case. The narrow line of hotter material observed around the block is the foil heater. The block was heated slowly to ensure that large temperature differences did not occur across its thickness. The temperature detected by the thermocouple at the block centre was close as possible to the surface temperature.

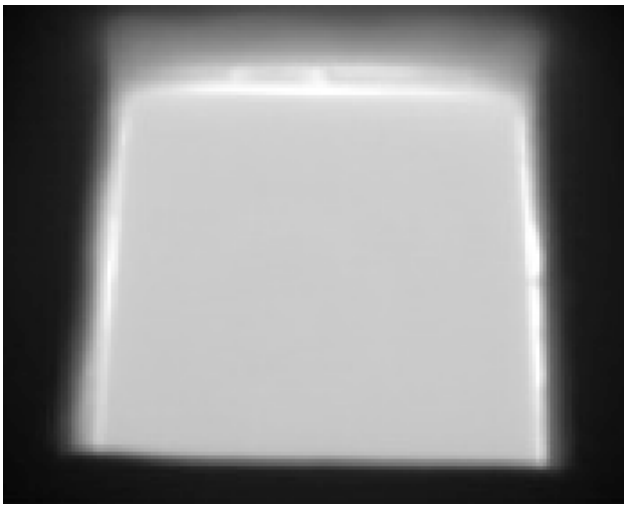

Figure 3-16 - IR Raw Image of the Copper Block

The copper block temperature was read from a digital thermometer. The temperature display produced readings accurate to 0.1°C. The display was recorded with a video camera to track the variation of temperature with time. This was achieved to an accuracy of one second.

The camera was connected to a data acquisition unit and a frame grabber program was opened. This program was designed to allow the rate at which the IR images were taken to vary. Each IR image is saved in a specified folder with a unique name and number. A separate MS Excel spread sheet is produced after an experiment. This document details the exact time at which the IR image was taken, location and name of that image, as well as the corresponding camera case temperature (accurate to 0.1°C).

	A	B	C	D	E
1	Date	Time	File location & name	IR Camera Temperature ('C)	Test Body Temperature ('C)
2	14/08/2011	16:52:42	c:\blockvideo3_1.raw	18.7	20.3
3	14/08/2011	16:52:55	c:\blockvideo3_2.raw	18.7	20.3
4	14/08/2011	16:53:08	c:\blockvideo3_3.raw	18.7	20.3
5	14/08/2011	16:53:22	c:\blockvideo3_4.raw	18.7	20.4
6	14/08/2011	16:53:35	c:\blockvideo3_5.raw	18.7	20.4
7	14/08/2011	16:53:49	c:\blockvideo3_6.raw	18.8	20.4
8	14/08/2011	16:54:02	c:\blockvideo3_7.raw	18.8	20.5
9	14/08/2011	16:54:15	c:\blockvideo3_8.raw	18.8	20.5
10	14/08/2011	16:54:29	c:\blockvideo3_9.raw	18.8	20.5
11	14/08/2011	16:54:42	c:\blockvideo3_10.raw	18.8	20.6
12	14/08/2011	16:54:55	c:\blockvideo3_11.raw	18.9	20.6
13	14/08/2011	16:55:09	c:\blockvideo3_12.raw	18.9	20.6

Figure 3-17 - Calibration MS Excel Sheet

From the video file of the thermometer display, the copper block temperature for the specific time at which the IR image was taken, was known and added to the calibration file (figure 3-17). Thus the IR camera body temperature and copper block temperature was recorded for each specific raw IR file.

3.2.3 IR Camera Calibration on a Black Nylon Mesh

Part of the project was concentrated on assessing the structure and trajectory of a coolant jet above the model surface for varying Blowing Ratio values. This was done by visualising thermal imprints of the jets on a fine nylon mesh. The mesh (Nylon) and cylinder model surface (Rohacell) have different emissivity values. As discussed in the previous chapter, the camera had to be calibrated separately for a nylon mesh and a copper block for this reason.

Figure 3-18 shows the arrangement for camera calibration on a nylon mesh. A hot air gun was used to heat the mesh. A variable resistor was used to control the heating intensity. The hot air gun was fixed in a stable position to ensure constant hot air stream projection. The gun was fixed at an angle to the camera view so that its hot filament would not be visible on the IR image.

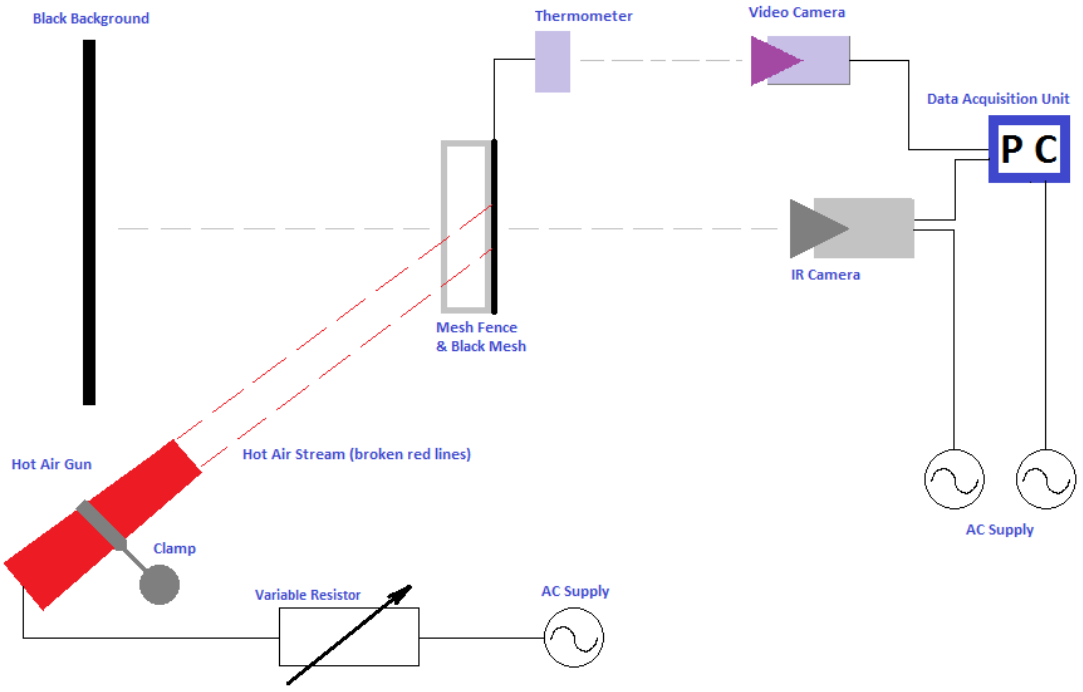

Figure 3-18 - Nylon Mesh Calibration Apparatus

The mesh was stretched on a mesh fence so that it did not bend or move and remained vertical throughout the experiment. The mesh was viewed against a black background in a dark room in order to simulate conditions of the wind tunnel experimentations (described earlier in this chapter).

Figure 3-19 - Photo (left) and IR image (right) of a thermocouple and mesh

A K-type thermocouple was threaded through the mesh with its metallic end as close as possible to the centre of the circular hot area on the mesh. Infrared imaging (figure 3-19) was then used to locate the centre (hottest area) of the jet on the mesh and accordingly adjust the thermocouple location before the start of calibration. The temperature signal was then measured using a digital thermometer and recorded by a video camera throughout the experiment. The data acquisition unit was used to record the data in the same way, as described in the previous paragraph.

3.2.4 Raw Calibration Data Processing

The acquired raw IR images for the calibration on a black solid body and the nylon mesh were further processed in MATLAB. A “Calibration Code” was written to open a raw image file, read-in the IRI values for each pixel of the image and display the IRI image in MATLAB. This code can be found in Appendix section 6.6.1. Figure 3-20 shows an IRI image of the heated copper block at 60°C.

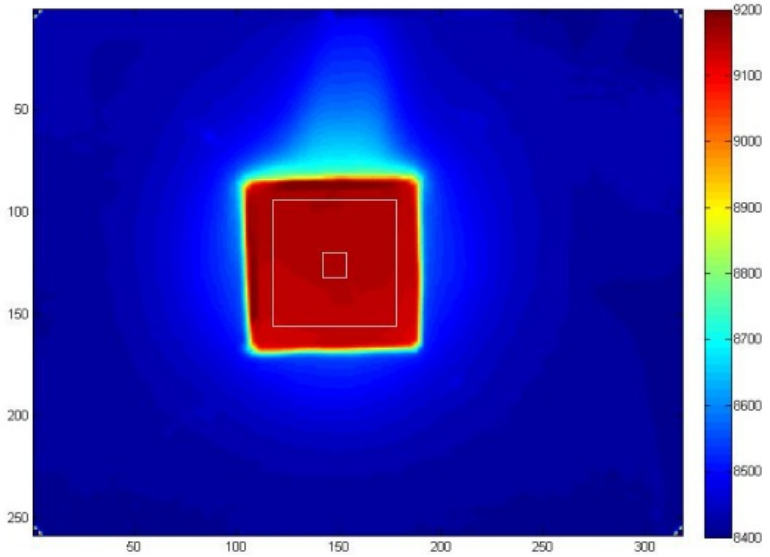

Figure 3-20 – IRI image of a block at 60°C

The scale to the right of the image displays the difference between IRI units of the block and surrounding Rohacell. Figure 3-21 shows a copper block at approximately 30°C and it can be easily seen that the hot foil heater is visible behind the block (less evident at higher block temperatures).

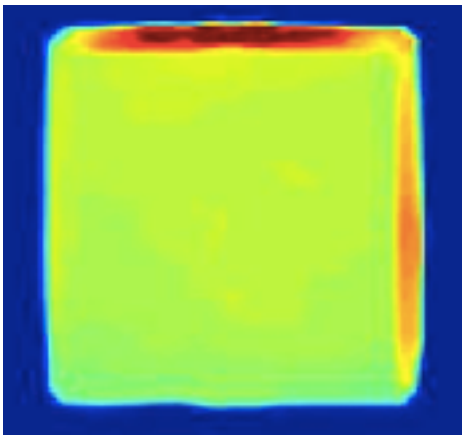

Figure 3-21 – IRI image of a block at 30°C

From both figures it can be seen that IRI values vary slightly across the block surface. This may be due to the fact that the block does not heat uniformly across the entire surface. It may be cooled non-uniformly by air motion within the laboratory. While every effort was made to ensure a uniform paint distribution, slight variations in paint thickness may occur across the block surface, which can affect both thermal conductivity and emissivity values of the painted surface. IR camera sensitivity is expressed by the noise equivalent temperature difference (NETD), which represents the difference in temperature between two points of the image that results in a signal equal to the random background noise of the camera. NETD is usually given at 30℃, for commercially available systems and ranges from 0.01℃ to 0.5℃ [60]. NETD of this particular camera is equal to $0.085℃$ [73], (i.e. nearly $\pm 0.1℃$) and may also be responsible for differences in IRI across the block. In order to minimise the effect of measurement uncertainties, the data used for the calibration was taken over a small central area of the copper block near the thermocouple location. Figure 3-20 shows white squares superimposed on the image of the copper block. IRI values for each pixel within the larger square were used to assess IRI variation, across the block surface. The smaller white square illustrates the area across which the IRI was used for calibration. The standard deviation of the smaller area was much smaller than across the entire block. Using data from central area ensured more consistent and reliable results. The mean IRI value across the smaller square was calculated for each image frame of a copper block at a known surface temperature. The internal camera temperature for each frame was also known. Hence by this method three variables are acquired for each image frame: (Infrared Intensity (IRI), Camera Case Temperature (T_C) and Test Body Temperature (T_B). The main difficulty of calibrating the camera over a nylon mesh is that the background can be seen through the mesh and background IRI values can be falsely taken for IRI values of the mesh. In order to avoid this a small square covering only a small portion of the mesh fibre as close to the thermocouple as practically possible was selected. This method ensured the background IRI was not falsely taken for the mesh IRI during calibration.

3.2.5 Effect of Test Body Temperature on Perceived IRI

Having acquired mean IRI for a copper block or a nylon mesh at a known temperature, it was possible to analyse the relationship between the test body temperature (T_B) and the corresponding IRI values.

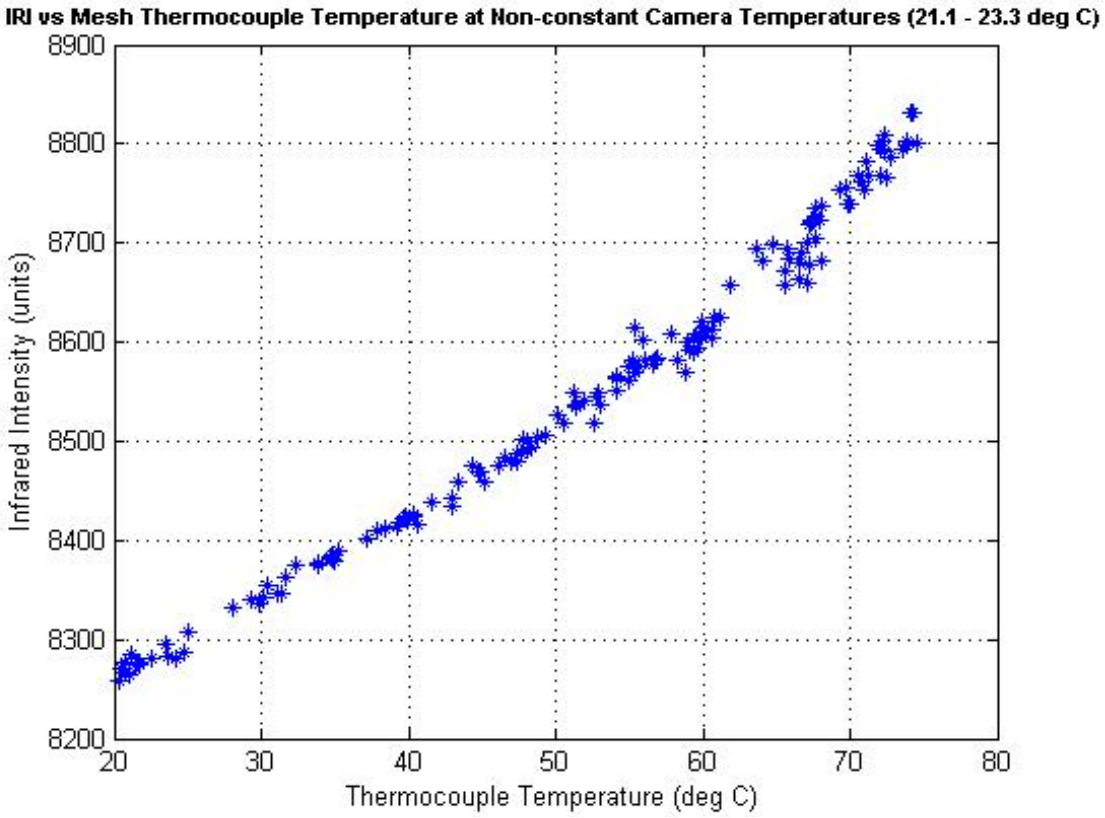

Figure 3-22 - A graph of IRI vs Mesh Temperature at non-constant Tc

Figure 3-22 demonstrates the variation of IRI, with the thermocouple temperature reading. The camera was not cooled during this mesh calibration, and T_C was not held constant (fluctuating between 21.1°C and 23.3°C). The extent and rate of such fluctuation is dependent primarily on the rate of image acquisition, as well as room temperature during the experiment. A clear positive relationship can be observed with IRI increasing as the temperature of the mesh increases. The relationship is not linear and more refined calibration may be necessary to determine graph gradient at the required thermocouple temperature reading with higher accuracy than a line of best fit.

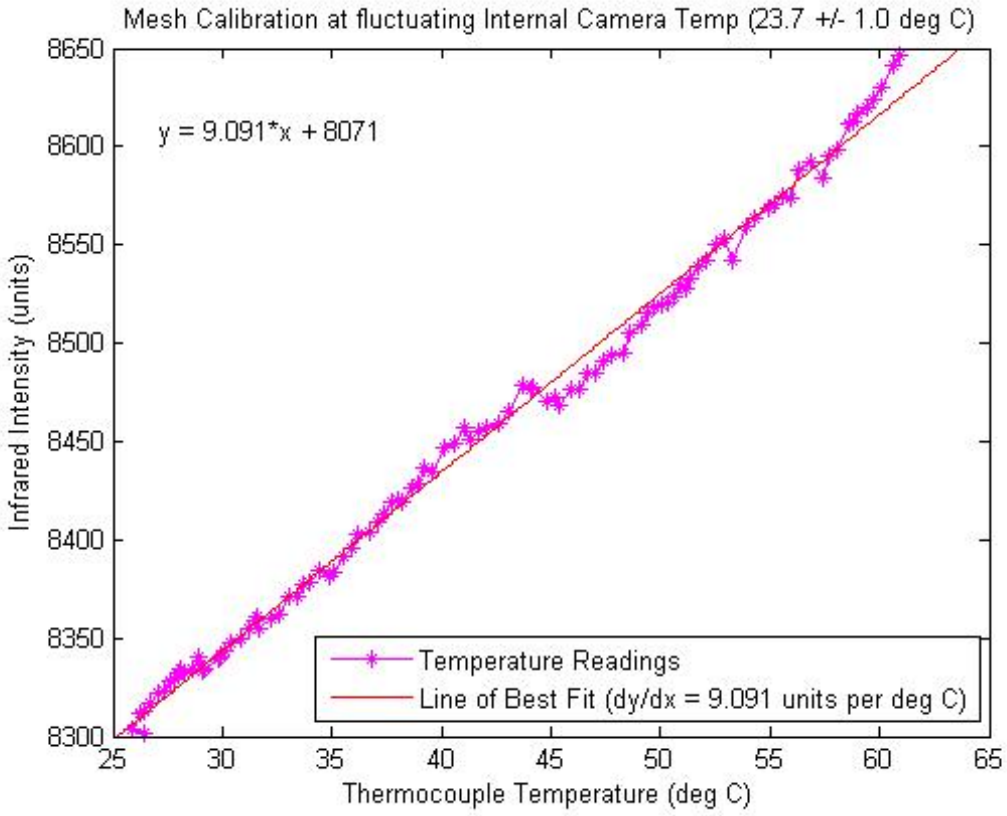

Figure 3-23 - A graph of IRI vs averaged mesh T at non-constant Tc

Figure 3-23 shows a plot of IRI variation with thermocouple temperature at fluctuating T_C (between 22.7°C and 24.7°C) for a different mesh calibration experiment. In this case IRI values have been averaged for each thermocouple temperature reading. A change of one degree in perceived mesh temperature accounts for a change of approximately 9 units of IRI.

3.2.6 Effect of Camera Case Temperature on Perceived IRI

The relationship between the internal camera temperature and the perceived IRI was analysed. For this purpose a copper block was heated to a known temperature of 60.3°C. The IR camera was then used to grab a series of images of the block, which was held constant at this temperature throughout the experiment. The camera case temperature was permitted to vary significantly (between approximately 18.2°C and 26.2°C). Figure 3-24 demonstrates how the perceived IRI values varied with camera case temperature for the fixed temperature of the block.

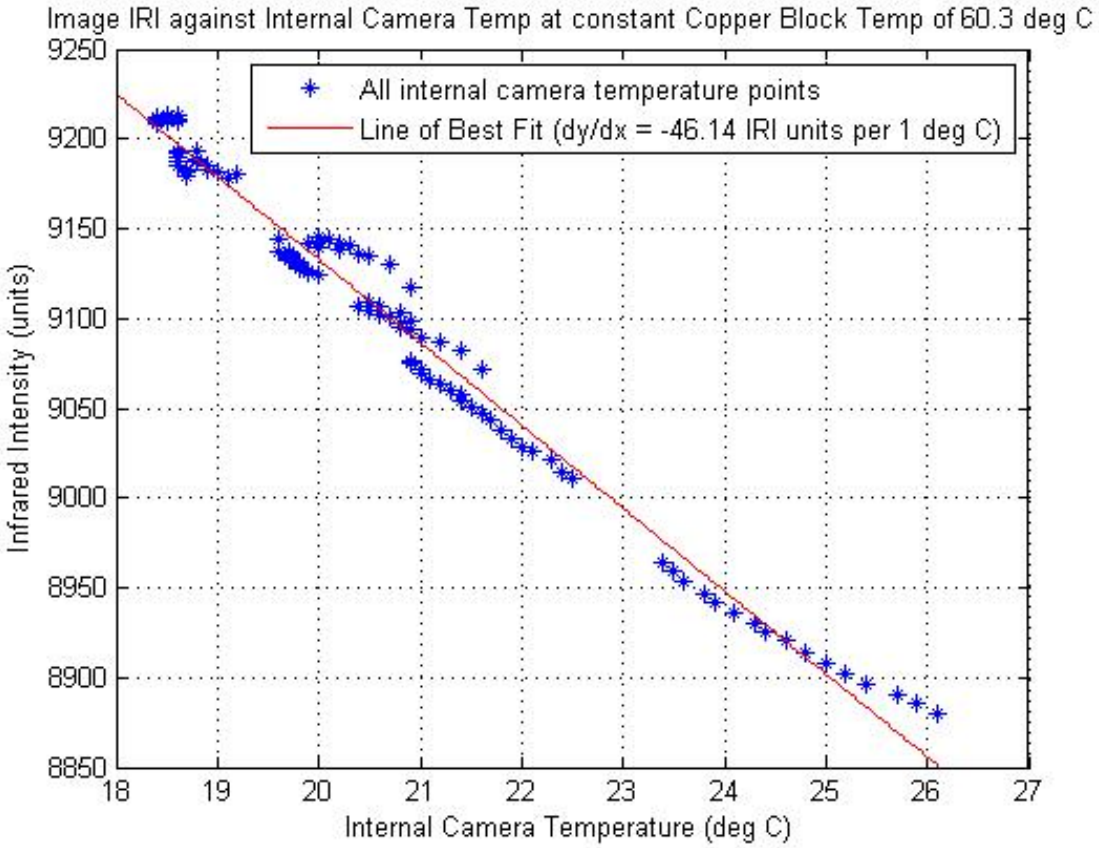

Figure 3-24 - A graph of IRI vs Tc for constant Tb

A negative relationship can be observed – increasing case temperature decreases the perceived IRI for constant T_B values.

Figure 3-25 shows a plot for the same experiment, where a mean value of IRI was taken for each value of case temperature to illustrate the average trend. From both figures it can be seen that the gradient of the line of best fit is approximately -46 IRI units per $1℃$ change in internal camera temperature. According to the findings described in the previous paragraph, an equivalent average difference in perceived IR intensity would be observed if the visualised body temperature was to decrease by approximately $5℃$.

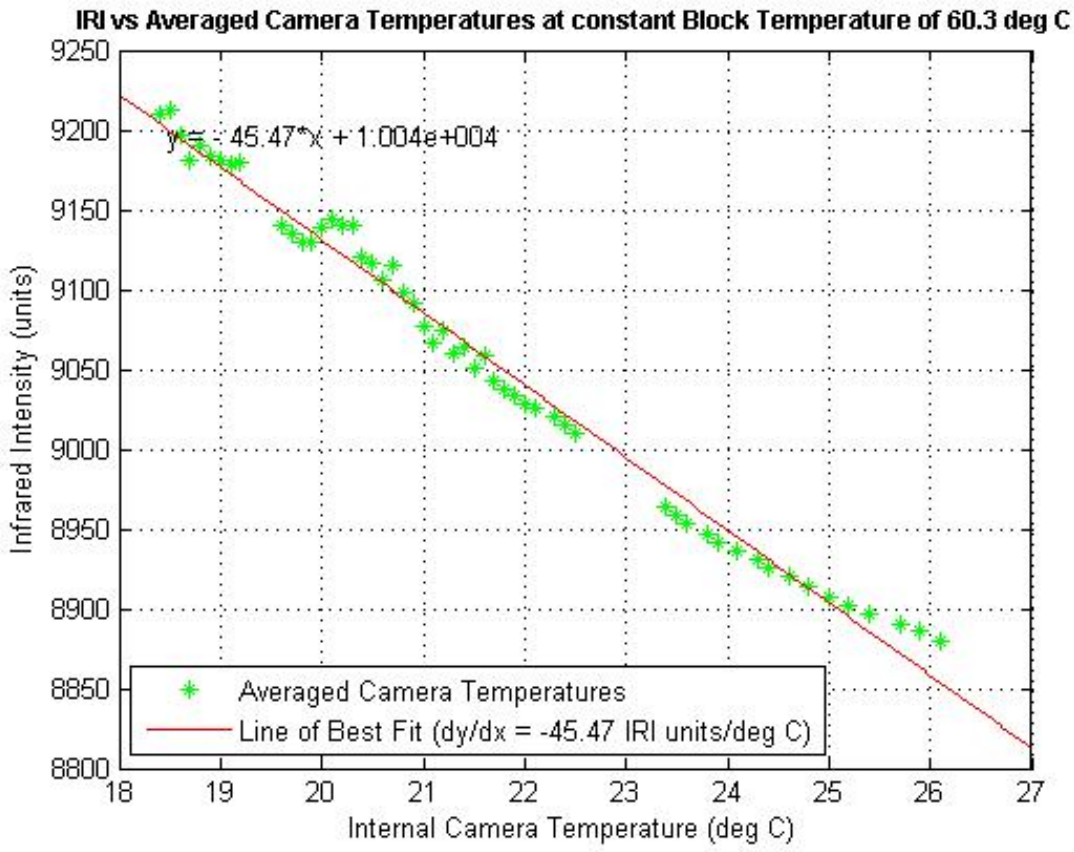

Figure 3-25 - A graph of IRI vs averaged Tc for constant Tb

It is evident that this relationship is not linear and better calibration could thus be achieved, if it was performed over a smaller temperature range (with data points fitting closer to the line of best fit over a smaller range). Thus limiting the calibration to the internal camera temperature range only encountered during the wind tunnel experimentation would increase calibration accuracy. Limiting variation of camera temperature (by cooling), as well as calibrating the camera only for this reduced range would yield even higher accuracy.

3.3 Calibration Technique Enhancement

The IR camera case temperature has a significant effect on perceived infrared intensity of a visualised body. The case temperature tends to vary during camera operation. This is dependent on length of operation, temperature of the surroundings and the frame-grabbing rate. The calibration experiments described in the previous section were performed prior to the start of wind tunnel experiments. No effort to control the camera case temperature was made, which resulted in T_C varying in the range of 18.2°C – 26.2°C.

During wind tunnel experiments T_C was found to have a reduced range of 18.2°C – 21.2°C due to the cold stream of air in the tunnel continuously cooling the camera. It has been discussed that because the relationship between IRI and T_C is not linear, increased accuracy of MATLAB codes can be achieved if the algorithms use graph gradients over a reduced T_C range. Post-experimental camera calibration was therefore performed over this reduced case temperature range.

Sufficiently cooling the infrared camera to a constant value of T_C can also allow to analyse the relationship between IRI and T_B more accurately.

3.3.1 Reducing IR Camera Case Temperature Oscillation

At first an air fan was tried to cool the camera and reduce case temperature. Windshields were designed to ensure the camera would be cooled effectively, without affecting the copper block surface during calibration (figure 3-26). The copper block was shielded with a wall, while a converging shield was used to concentrate the cool airstream directly onto the IR Camera.

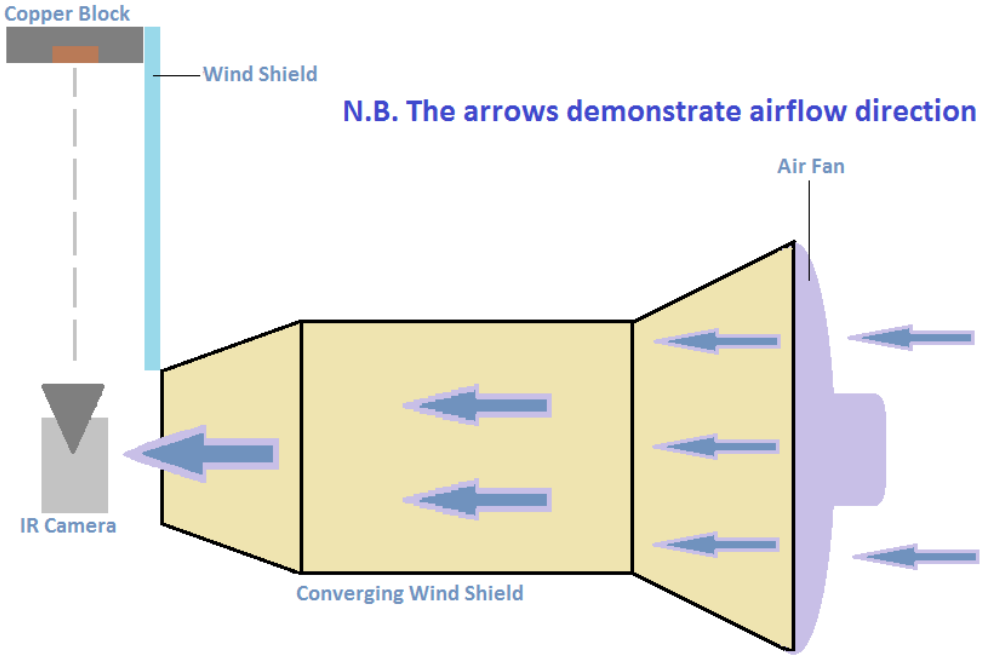

Figure 3-26 - Cooled camera calibration set-up

The case temperature oscillation was reduced, but even at the maximum fan speed setting, case temperatures encountered during wind tunnel experiments have not been achieved. For this reason it was decided to perform cooled calibration in the wind tunnel instead.

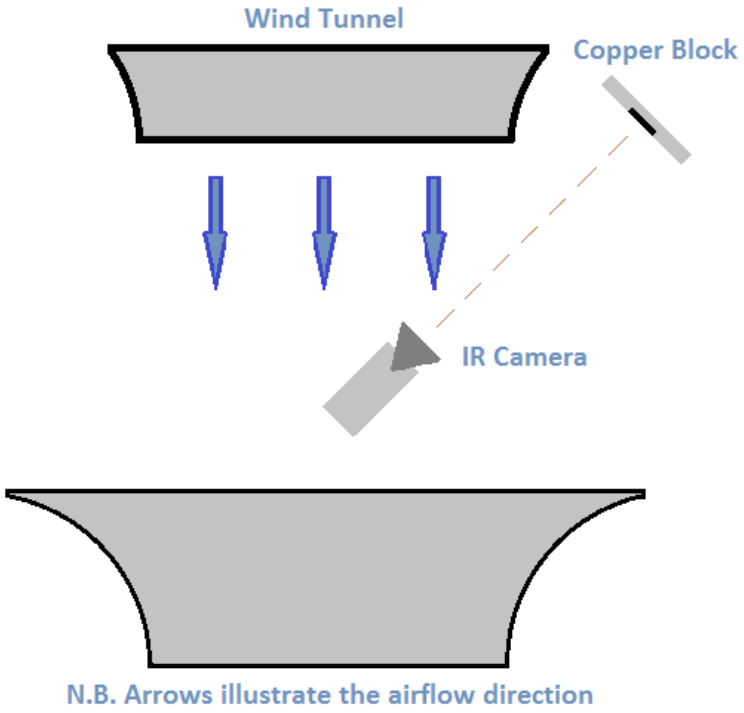

Figure 3-27 - Cooled camera (wind tunnel) calibration set-up

Figure 3-27 illustrates wind tunnel cooled calibration equipment set-up (not to scale). The copper block was shielded and positioned outside the wind tunnel in such a way that its surface temperature would not be influenced by the cool airflow and would not deviate significantly from the temperature taken inside the block by the thermocouple. To maintain high image resolution of the block, the IR camera position within the wind tunnel was adjusted to be as close to the block as possible while being cooled by the cold airflow. The case temperature and block temperature were acquired as described previously.

3.3.2 Improved Tb vs IRI Relationship Analysis

Case temperatures in the range of 18.2°C – 21.2°C have been achieved during this calibration as intended. In addition it was possible to maintain a constant case temperature of 18.4°C during one calibration, where the block temperature was increased from 22°C – 62°C (figure 3-28).

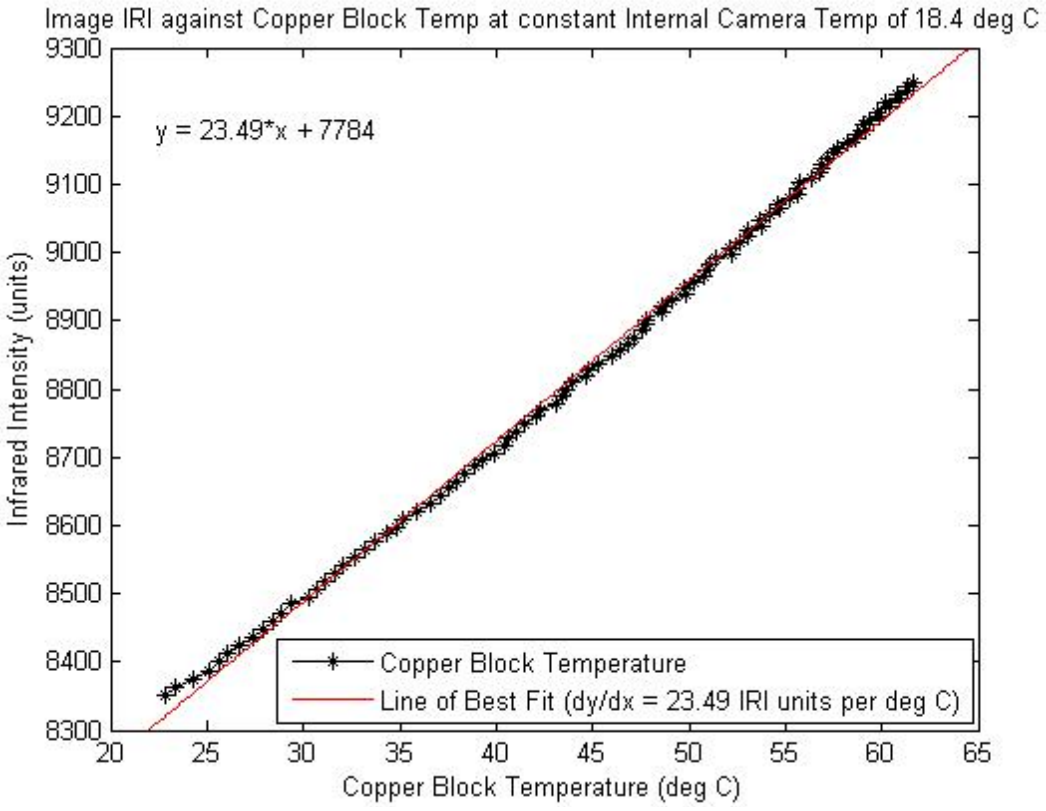

Figure 3-28 - A graph of IRI vs Tb for constant Tc

A nearly ideal positive relationship can be observed with a gradient of approximately 23.5 IRI units change per degree change in block temperature. It can be seen that the calibration data obtained for the nylon mesh deviates significantly from that obtained from the copper block even though they are at the same temperature. The difference in gradients of approximately 9.1 IRI units change per degree change in mesh temperature versus the 23.5 IRI units change for the respective block temperature variation has been observed. Due to such high differences, the mesh and cylinder surface images have to be processed separately using different codes.

3.3.3 Improved Tc vs IRI Analysis

Figure 3-29 illustrates variation of T_C in the range of 18.2°C – 21.2°C for a constant T_B of 60.3°C. A linear approximation over this reduced range seems much more accurate and appropriate than in the range considered earlier.

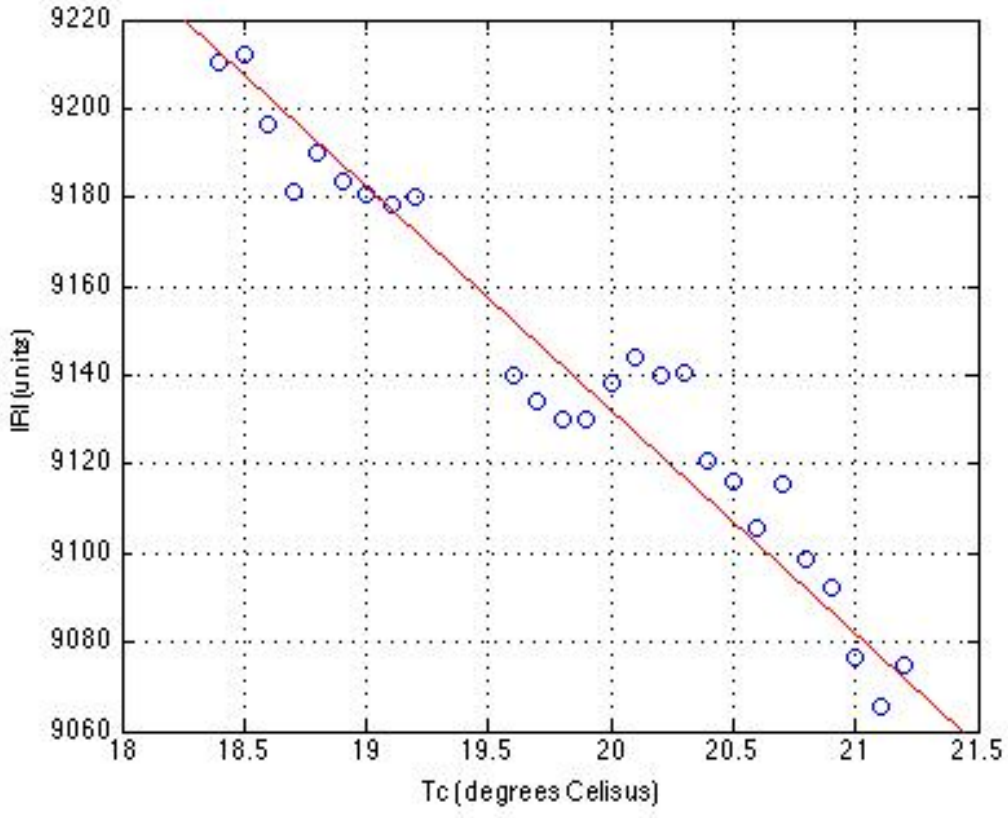

Figure 3-29 IRI vs Tc (reduced range) for constant Tb (= 60.3°C)

By making this approximation, a line of best fit was plotted and its gradient has been calculated as – 50 IRI units per 1°C (hence perceived IRI value would decrease by 50 units for every degree increase in T_C, when observing a body of constant temperature).

3.3.4 Temperature MATLAB Code

Perceived infrared intensity (IRI) is dependent on surface temperature of the visualised body (T_B) and the camera case temperature (T_C). The relationship between these variables can be written in two simultaneous equations:

$$IRI = -m_1 T_c + A_1$$
$$IRI = m_2 T_B + A_2$$

where the letter *m* denotes a graph gradient and *A* denotes a *y* intercept. A MATLAB code was developed to take information of each raw IR image (pixel-wise) IRI and (image-wise) T_C from the frame grabber program and use it to form a respective (pixel-wise) surface temperature image. Thus for each pixel of the image, the IRI value was replaced by the T_B value. An algorithm was written for this purpose:

$$T_B = a(IRI) + b(T_C) + d$$

where *a, b* and *d* are constants. EViews 7 (a statistical package for Windows) was used for determining the constants. The algorithm was included in the MATLAB code in order to display an image in terms of **Temperature**, rather than **IRI**. This code is henceforth referred to as a Temperature Code and can be found in Appendix section 6.2.2.

3.3.5 Code Validation

By using the temperature code, it was possible to convert the IRI images into temperature distribution images and hence compute the copper block surface temperatures (allowing the accuracy of Matlab codes to be validated, by comparing the computed surface temperature values with experimentally measured copper block temperature values).

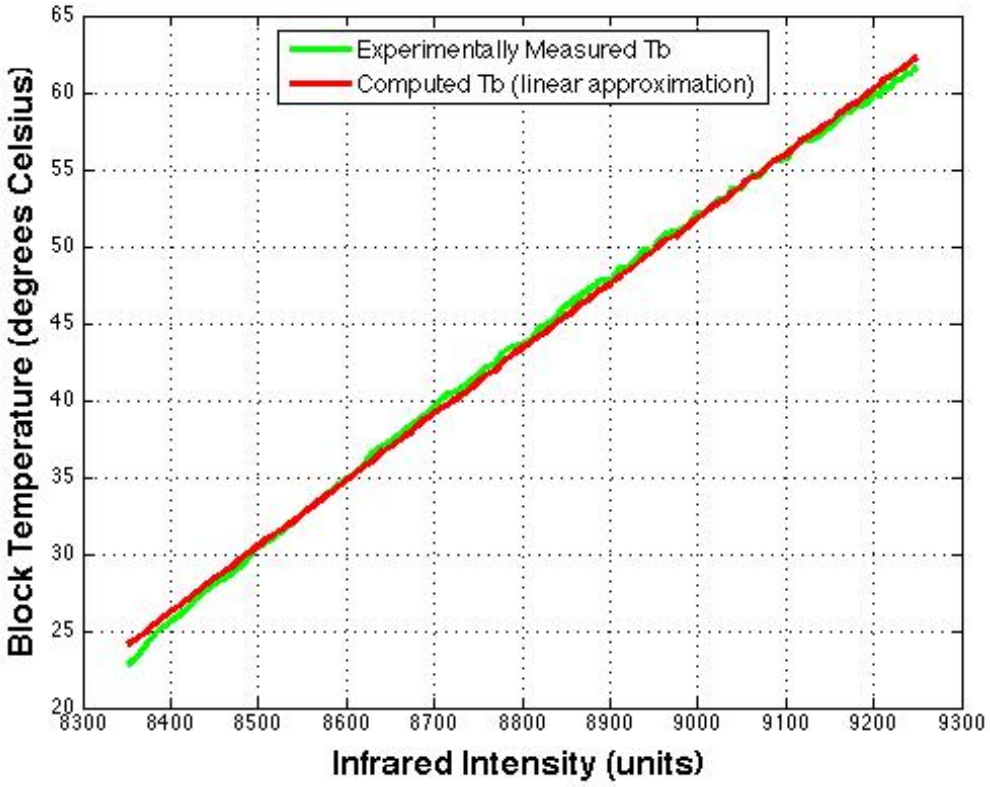

Figure 3-30 Tb vs IRI for constant Tc (= 18.4°C) – Linear Approximation

Figure 3-30 illustrates the computed copper block temperature values produced using the algorithm assuming a linear relationship of T_B and IRI (in red) compared with the true measured T_B values (in green). The T_B range considered in this study (approximately 22 – 62°C) is relatively small, since a linear approximation yields a reasonably accurate prediction.

The relationship between T_B and IRI is evidently not linear and resembles a second-degree polynomial relationship. Therefore a different algorithm has been constructed and validated for comparison.

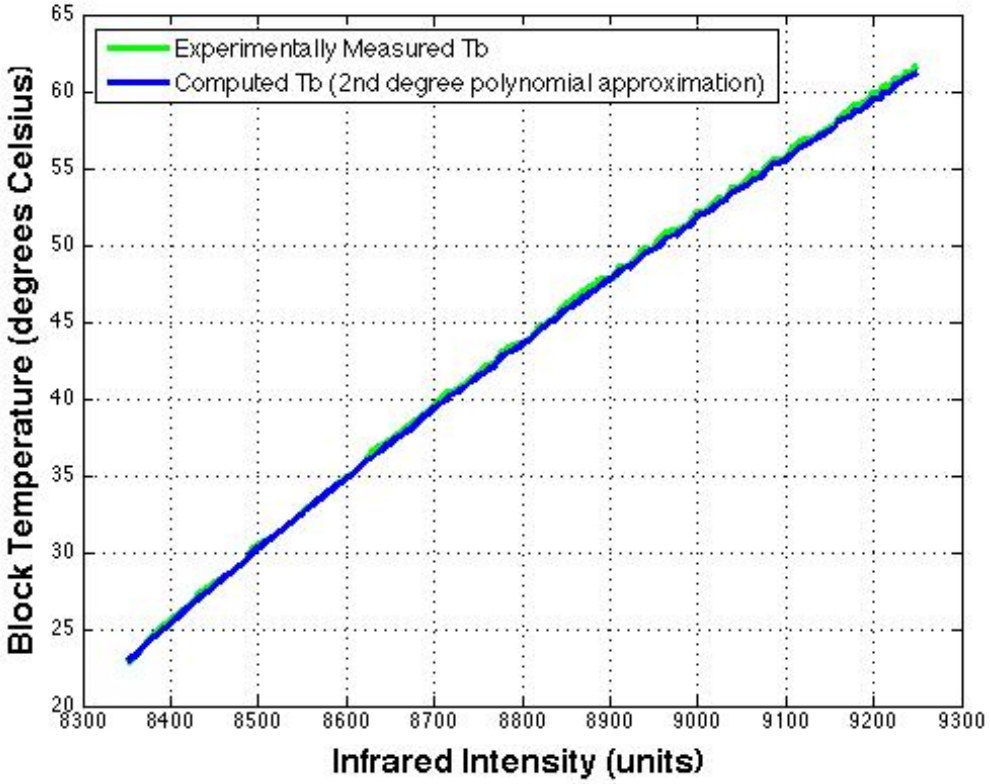

Figure 3-31 Tb vs IRI for constant Tc (= 18.4°C) – 2nd degree polynomial

Figure 3-31 illustrates the computed values produced using an algorithm assuming a second-degree polynomial relationship of T_B and IRI (in blue) compared to the measured T_B values (in green). It can be seen that this algorithm can compute T_B with a higher degree of accuracy. This is more clearly seen in figure 3-32, which demonstrates the difference between measured and computed T_B values for both algorithms.

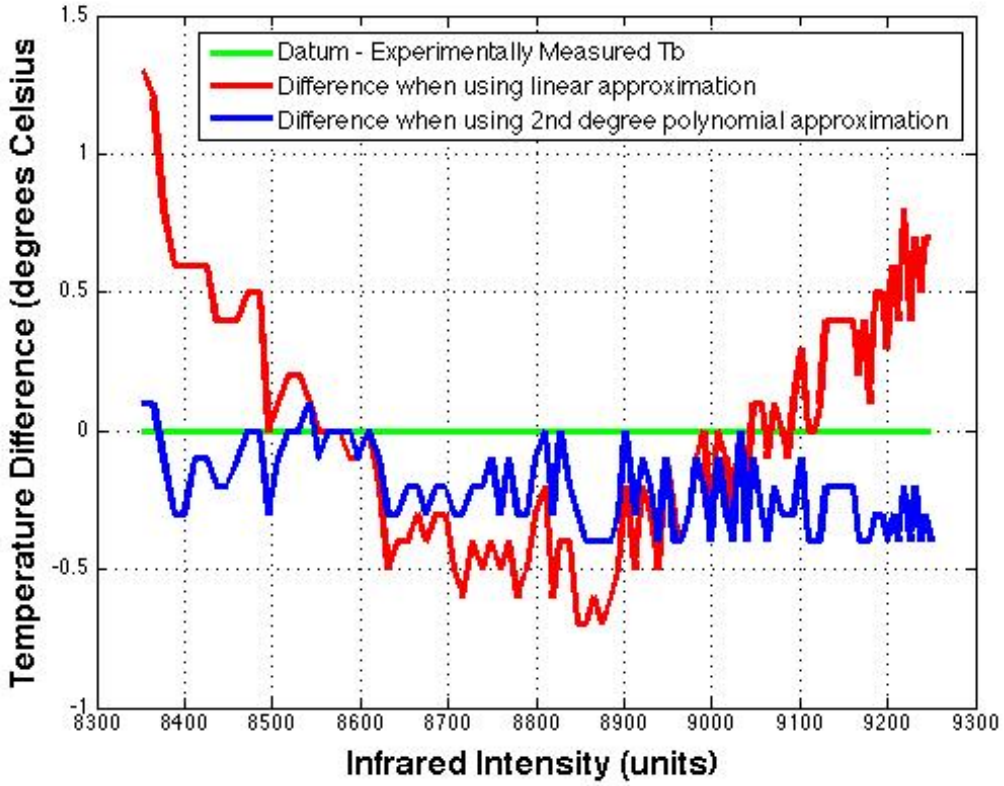

Figure 3-32 – The difference between measured and computed Tb value

The linear approximation data spread is +1.3/-0.7°C from the measured T_B values (the data is spread over a 2°C range). The second-degree polynomial approximation has a reduced data spread (+0.1/-0.4°C – a range of only 0.5°C) and is a much better fit to the measured block temperatures.

It is not visually evident from the range of T_B considered in this study, whether higher polynomial degree values may yield better approximations. This could form a useful basis for future studies, however it will not be considered in this work due to time limitations.

3.4 Post-experimental Data Processing

Various MATLAB codes were written and image processing techniques were used to analyse and improve the quality of experimental results. These codes and techniques will be discussed in more detail in this section.

3.4.1 Image Enhancement

The infrared camera produces images with a relatively poor resolution, as the raw images appear pixelated. This is noticeable in model surface images where coolant jets vary in shape and IRI value over small areas of the image frame and becomes even more pronounced during visualisation of the fine nylon mesh.

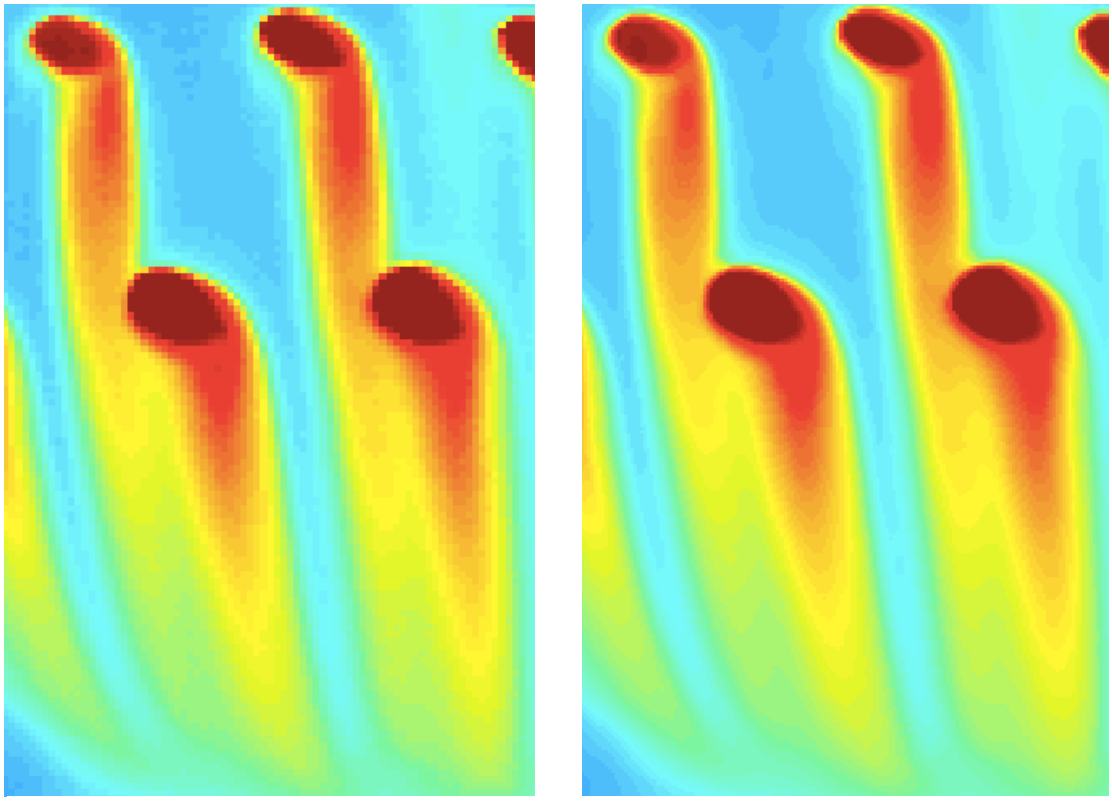

Figure 3-33 - Surface Image before (left) and after (right) image enhancement

Figure 3-33 illustrates how artificially increasing the number of image pixels per frame and applying a median filter can reduce noise and enhance image resolution. This technique has been used to enhance representation of the experimental results (detailed in the next chapter).

3.4.2 Effectiveness Code

As has been described in Chapter 2, the gas effectiveness can be defined as:

$$\eta = \frac{T_s - T_m}{T_{cg} - T_m}$$

where T_m and T_{cg} are the mainstream and coolant gas temperatures, determined experimentally and known for each image frame. T_s denotes the visualised surface temperature (e.g. mesh, or copper block). The above equation is included in an effectiveness MATLAB code, which converts the temperature value of each image pixel into the representative effectiveness value. The MATLAB code itself can be found in Appendix section 6.2.3.

Both the cylinder and the nylon mesh surface temperatures are assumed to be equal to the adjacent flow. The T_s value is taken as T_{aw} for η_{aw} (adiabatic wall effectiveness for cylinder visualisation), and as T_{mesh} for η_{gas} (gas effectiveness for mesh visualisation).

3.4.3 Contour Plots

The effectiveness code described in the previous section is capable of producing global distribution images of effectiveness over a visualised body. These images are very useful for qualitative flow analysis and can be used in order to visualise and understand flow patterns, as well as qualitatively comparing which cooling conditions appear to be more effective. It is considered to be sufficient for analysis conducted in this study.

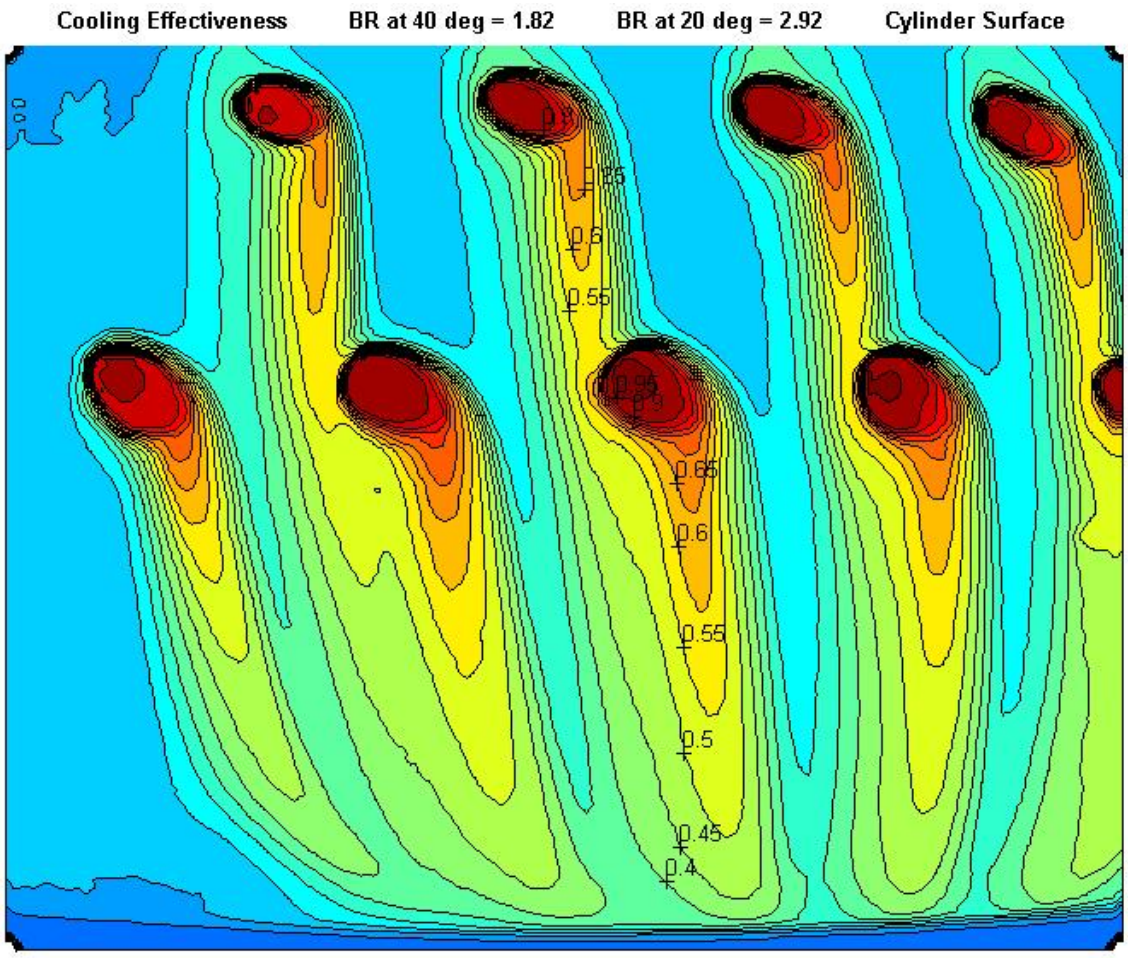

Figure 3-34 - A contour plot of cooling effectiveness over a cylinder surface

A contour plot image (figure 3-34) however can provide a more practical method of test surface visualisation for quantitative analysis of cooling effectiveness distribution in the future studies.

3.4.4 Image Segmentation

During visualisation of a fine nylon mesh, an infrared camera observes both the mesh and the background. The use of a median filter can cause the background IRI readings to be averaged with adjacent mesh IRI readings – resulting in reduced gas effectiveness values across the mesh. An image processing technique called Image Segmentation can be used to filter-out the background IRI readings to prevent this. Image Segmentation would only be effective if image resolution is sufficient to clearly distinguish the fine mesh fibres from the background however (i.e. if a mesh fibre is at least 3 pixels wide on the image – where the central pixel can be taken as the mesh IRI value, while the mesh pixels adjacent to background can be ignored).

3.5 Conclusion

This chapter has described in detail the process of preparation, set-up and operation of the experimental apparatus used in this project. The calibration and post-experimental data processing techniques have also been discussed. The experimental results obtained will be discussed in the next chapter.

4 Experimental Results

This chapter concentrates on experimental results achieved using Infrared Thermography to capture images of coolant plumes over a cylinder model (simulating the leading edge of a gas turbine blade), as well as plume contours on a nylon mesh at perpendicular angles to the cylinder surface for different circumferential locations.

The parameters used for representation of coolant plumes are Calculated Gas Effectiveness (*CGE* - at the mesh) and Calculated Adiabatic Wall Effectiveness (*CAWE* - at the cylinder surface). The calculated effectiveness values are based on thermocouple temperature readings and the temperature distribution over the visualised body (mesh, or cylinder) produced by the IR camera. These values are subjected to various uncertainties (limitations of the IRT technique in turbine cooling visualisation) and are detailed in this chapter.

It is therefore difficult to claim that CAWE and CGE are absolute effectiveness measurements made to a high accuracy, but they do provide qualitative visualisation of coolant jets at and above the model surface (part of the identified applications discussed in this chapter). It is possible to compare data acquired at the cylinder surface and different mesh locations in order to assess the results for consistency. The calibration method of the camera could be further improved in order to produce more accurate distributions, which could potentially enable quantitative analysis of gas, or adiabatic wall effectiveness. The potential improvements are also discussed in this chapter.

The methodology of this work enables qualitative analysis of coolant plumes and could therefore be used to qualitatively assess optimum film-cooling characteristics of turbine blades (aiding in design and development). This can be achieved by analysis of the extent of film-cooling coverage and Calculated Adiabatic Wall Effectiveness values at respective Blowing Ratios. An optimum BR value could thus be estimated to provide optimum cooling. The coolant jet cross-section profiles could be analysed from mesh images to establish how

the coolant flow interacts with the mainstream at the BR values. Some of the BR values considered in this work are not considered to be representative of real engine conditions, but are used for the purposes of general assessment of the experimental technique feasibility. Some work that does not fall immediately into the scope of the project is also discussed in this chapter.

4.1 Introduction

The circumferential pressure distribution around the cylinder model in the wind tunnel was measured at 5-degree intervals. These values have been converted into pressure coefficients and plotted in figure 4-1.

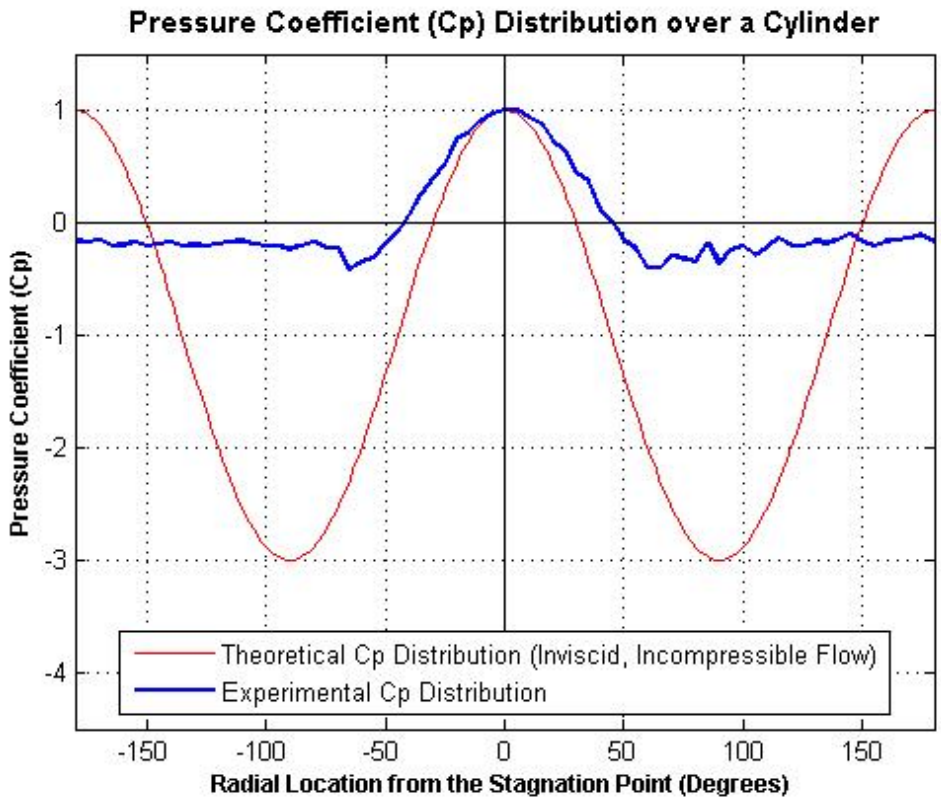

Figure 4-1 – Cp distribution over the cylinder model

The experimental pressure coefficient has been plotted with the theoretical distribution, based on inviscid and incompressible flow: $C_p = 1 - 4sin^2\phi$. The difference between these values has been attributed to friction of air with the cylinder surface, in addition to compressibility and turbulence effects.

C_p equals unity on the Stagnation Line (*SL*), indicating that the cylinder is level with the horizontal and SL of the cylinder is aligned with the centreline of the zero degree row of coolant ejection holes. It can be seen from the plot of experimental results that airflow begins to separate from the cylinder surface at approximately $\pm 70°$ from SL. This is reasonably close to the anticipated point of separation for viscous and compressible airflow around a circular cylinder ($\phi \approx 80^{\circ}$) for Reynolds numbers between 10^5 and 10^6 [74].

4.1.1 Blowing Ratios

The Blowing Ratios (*BR*) for settings of the coolant air pump and the respective coolant stagnation pressures have been calculated and listed in table 1, where BR_{20} and BR_{40} stand for *BR* values at $\phi = 20°$ and $\phi = 40°$ respectively:

Pump power setting	Coolant total pressure	BR_{20}	BR_{40}
3.5	63	1.04	1.01
4	67	1.15	1.05
4.5	70	1.23	1.08
5	77	1.39	1.13
5.5	81	1.48	1.17
6	90	1.64	1.23
6.5	98	1.78	1.29
7	111	1.98	1.37
7.5	121	2.12	1.44
8	135	2.32	1.53
8.5	149	2.49	1.61
9	168	2.7	1.71
9.5	181	2.83	1.77
10	189	2.92	1.82

Table 1 – Blowing Ratio variations for different coolant pump settings

The coolant air pump is technically not able to work faster to generate larger BR values. At power settings below 3.5 it fails to provide sufficient air flow to eject the coolant through the coolant ejection holes. The range of the achievable blowing ratios with the current apparatus is therefore limited to between 1.04 and 2.92 units for the row of coolant ejection holes at $20°$ from SL and 1.01 to 1.82 for the respective $40°$ row of coolant ejection holes.

The Blowing Ratios encountered in typical turbine blade environments vary approximately from 0.5 to 2.0 [21], which are lower than some of the obtained values in this experiment (although some research groups have analysed BR values as high as 2.7 [7], BR = 3 [31], or even higher [19,32]. The range of BR values shaded green in table 1, was used to analyse the jet structure after lift-off (mesh images) and further assess camera consistency by comparing CGE and CAWE values.

The BR values, which are not considered as being representative of typical turbine blade environments, are shaded green in Table 1. Unfortunately Blowing Ratios in the region of 0.5-1.0 are out of scope of this study due to technical limitations of the apparatus (pump) and time constraints (insufficient time to change this apparatus). Analysis of an extended BR range (including 0.5-1.0) could form a good basis for a potential further study in the future however.

4.2 Cylinder Surface Visualisation

The following section concentrates on analysis of cylinder surface images. The images demonstrate results of processing data with an effectiveness code in MATLAB. Figures 4-2 – 4-15 represent distribution of Calculated Adiabatic Wall Effectiveness (CAWE) and the scale is set between 0 and 1 units (where 1 equals 100% CAWE).

4.2.1 Adiabatic Effectiveness at Cylinder Wall Images

The CAWE values at location of the coolant ejection holes are most often in the region of 95%-100%, which is consistent with expectations (although values around 90% can be observed at lowest BR image). The background effectiveness value is expected to be close to 0%, but is in fact in the range of 10%-20% for most images. This value is higher than anticipated, but the background thermal emissivity values deviate from that of the cylinder model (for which the camera calibration has been performed). The effectiveness values are computed on the assumption that thermal emissivity is constant throughout the image. Therefore high background effectiveness values may be largely due to its emissivity differing significantly from the cylinder surface.

Qualitatively, the images illustrate how coolant coverage of the turbine blade model changes across the surface over the tested range of blowing ratios. The (upstream) row of coolant holes on the left side of each image corresponds to the row at $20°$ from SL. Consequently the (downstream) row of coolant holes on the right side of each image corresponds to the row of holes at $40°$ from SL. A blowing ratio value for circumferential location of each coolant hole row is stated above each of the separate images.

Figure 4-4 – Cylinder Surface
BR_{40}=1.08, BR_{20}=1.23

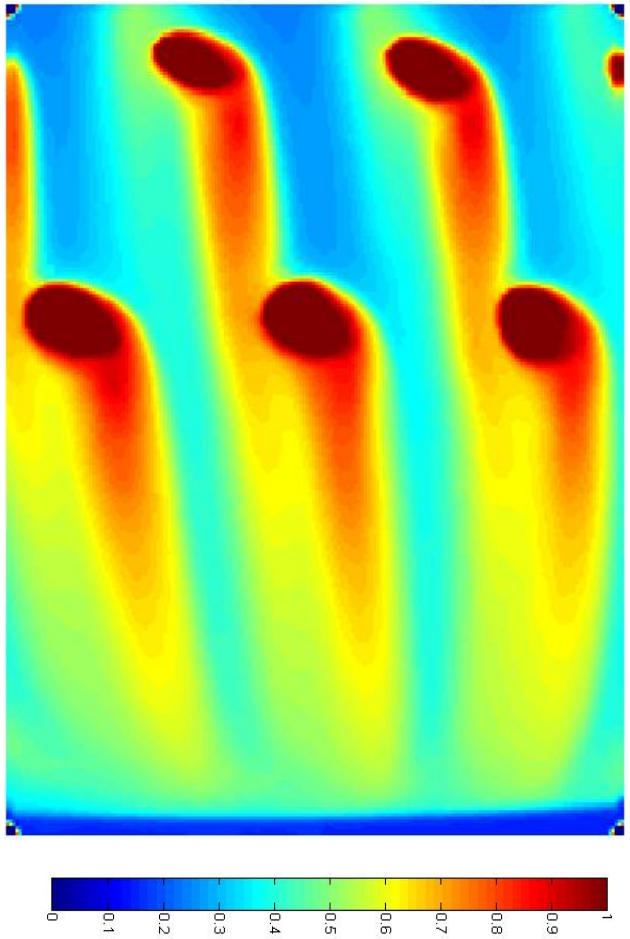

Figure 4-3 – Cylinder Surface
BR_{40}=1.05, BR_{20}=1.15

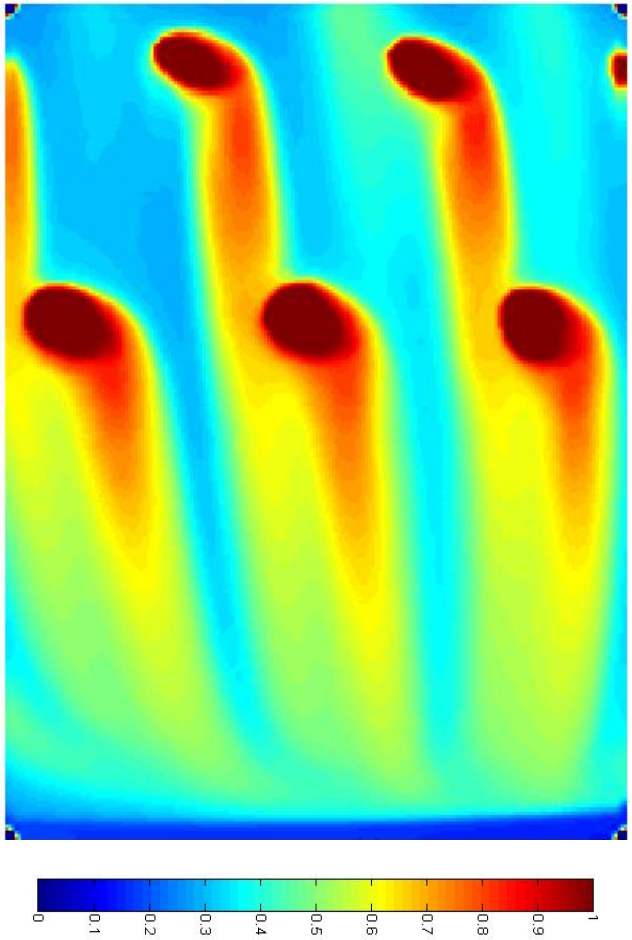

Figure 4-2 – Cylinder Surface
BR_{40}=1.01, BR_{20}=1.04

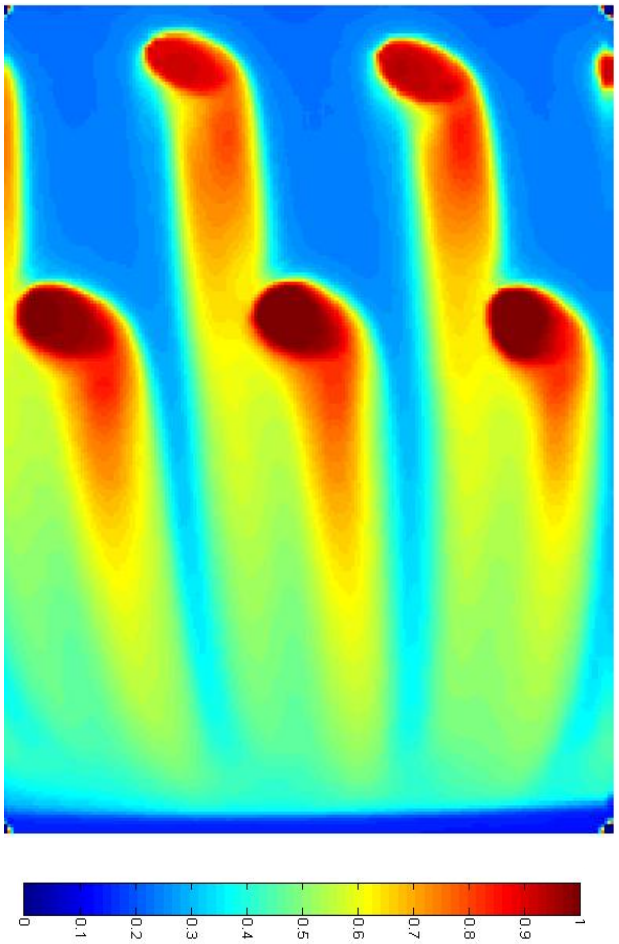

Figure 4-7 – Cylinder Surface
BR_{40}=1.23, BR_{20}=1.64

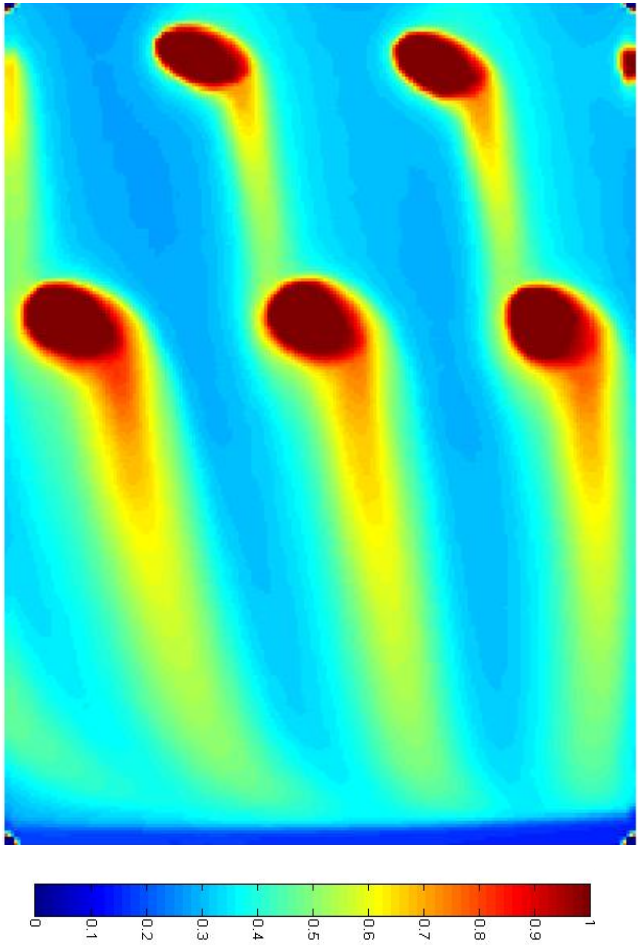

Figure 4-6 – Cylinder Surface
BR_{40}=1.17, BR_{20}=1.48

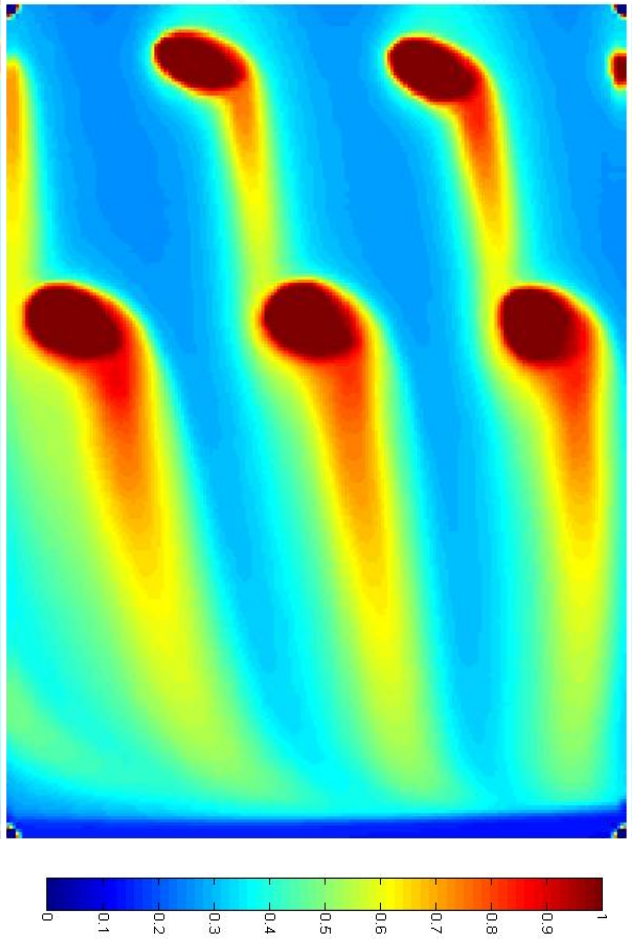

Figure 4-5 – Cylinder Surface
BR_{40}=1.13, BR_{20}=1.39

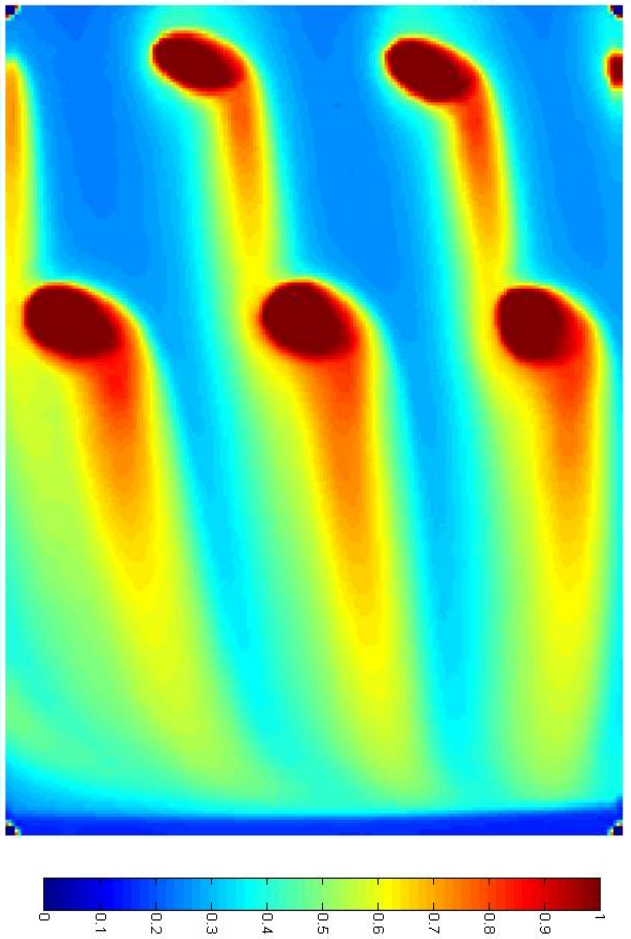

Figure 4-8 – Cylinder Surface
BR_{40}=1.29, BR_{20}=1.78

Figure 4-9 – Cylinder Surface
BR_{40}=1.37, BR_{20}=1.98

Figure 4-10 – Cylinder Surface
BR_{40}=1.44, BR_{20}=2.12

Figure 4-13 – Cylinder Surface
BR_{40}=1.71, BR_{20}=2.70

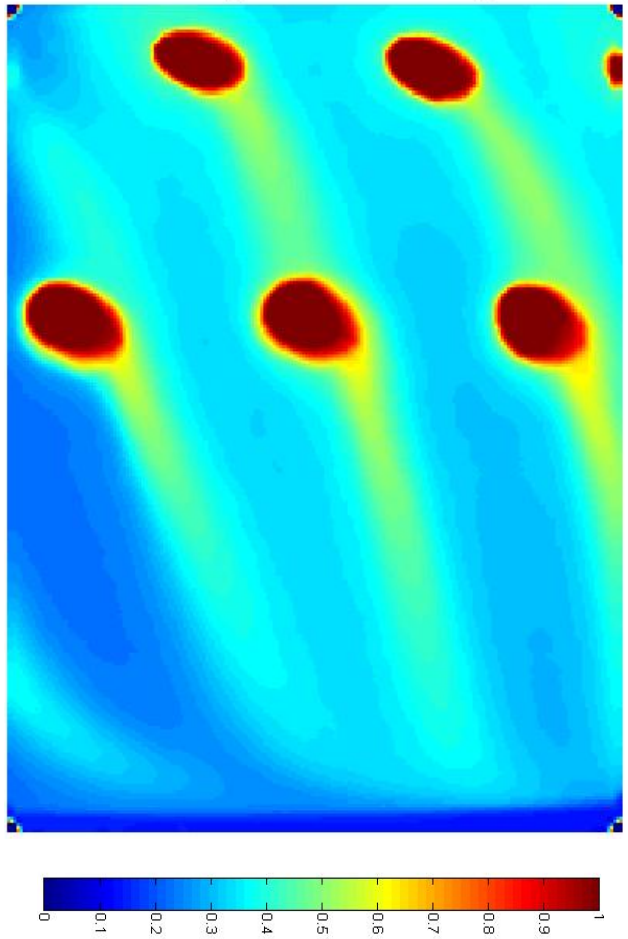

Figure 4-12 – Cylinder Surface
BR_{40}=1.61, BR_{20}=2.49

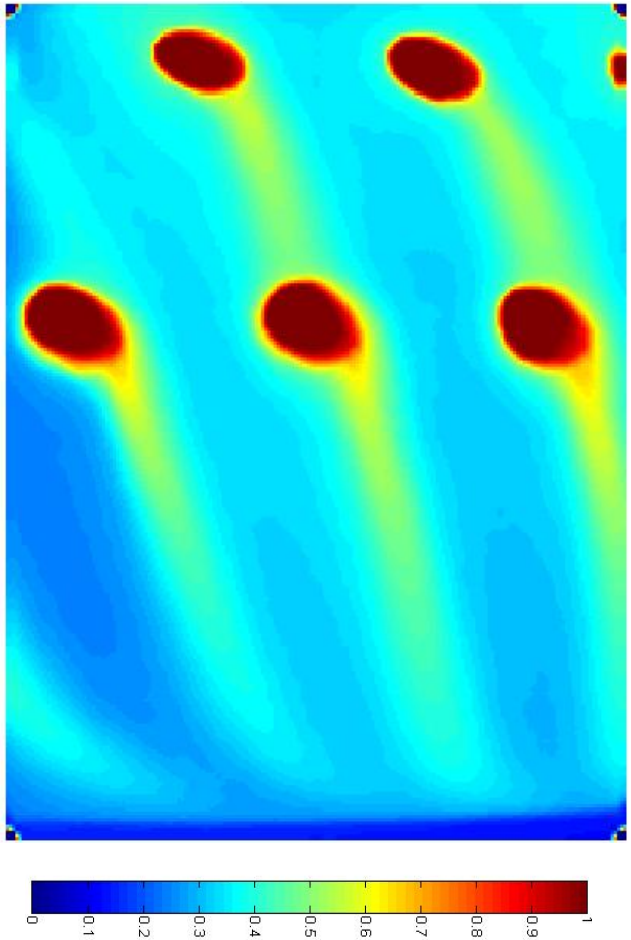

Figure 4-11 – Cylinder Surface
BR_{40}=1.53, BR_{20}=2.32

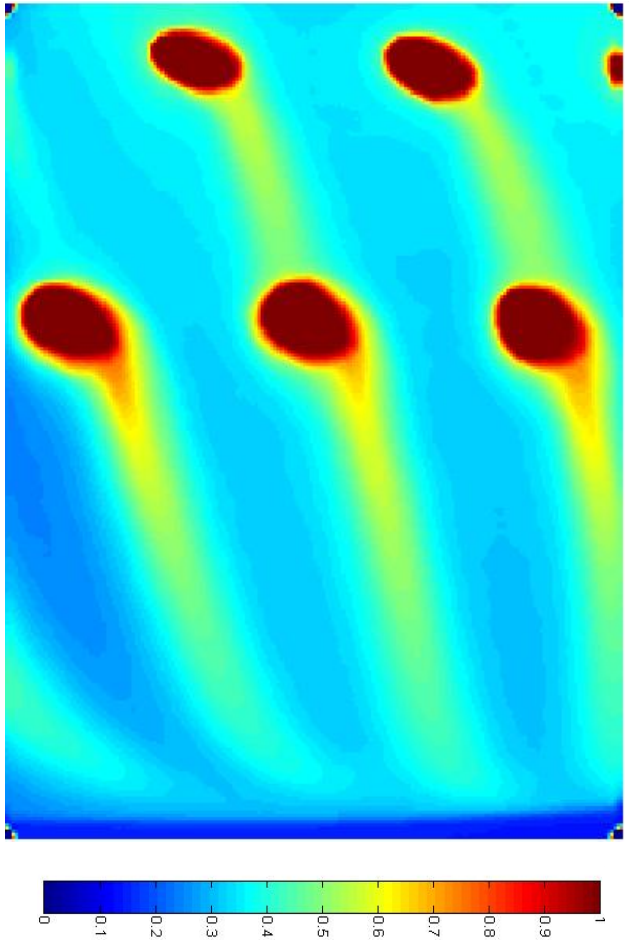

Figure 4-15 – Cylinder Surface
BR_{40}=1.82, BR_{20}=2.92

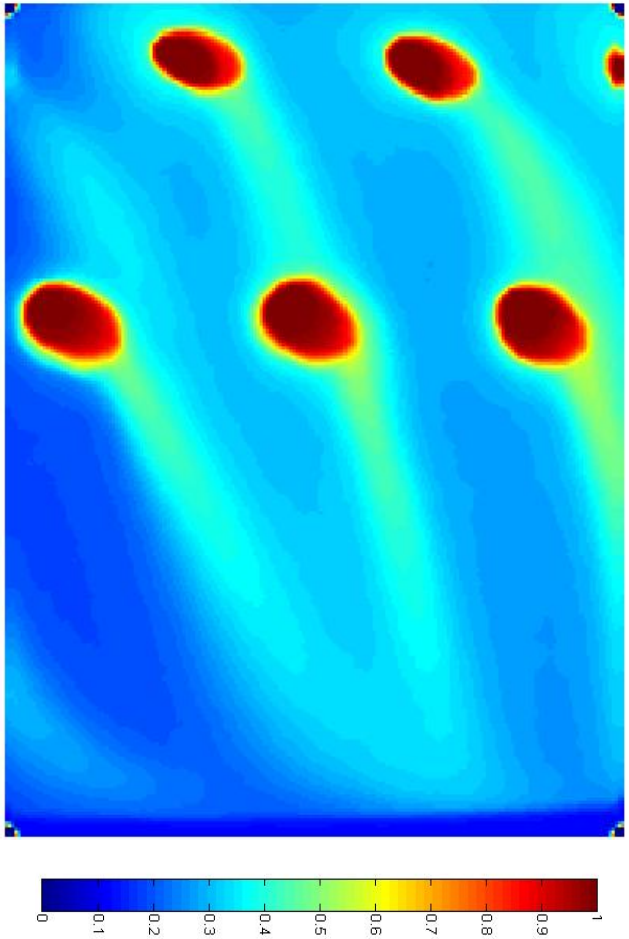

Figure 4-14 – Cylinder Surface
BR_{40}=1.77, BR_{20}=2.83

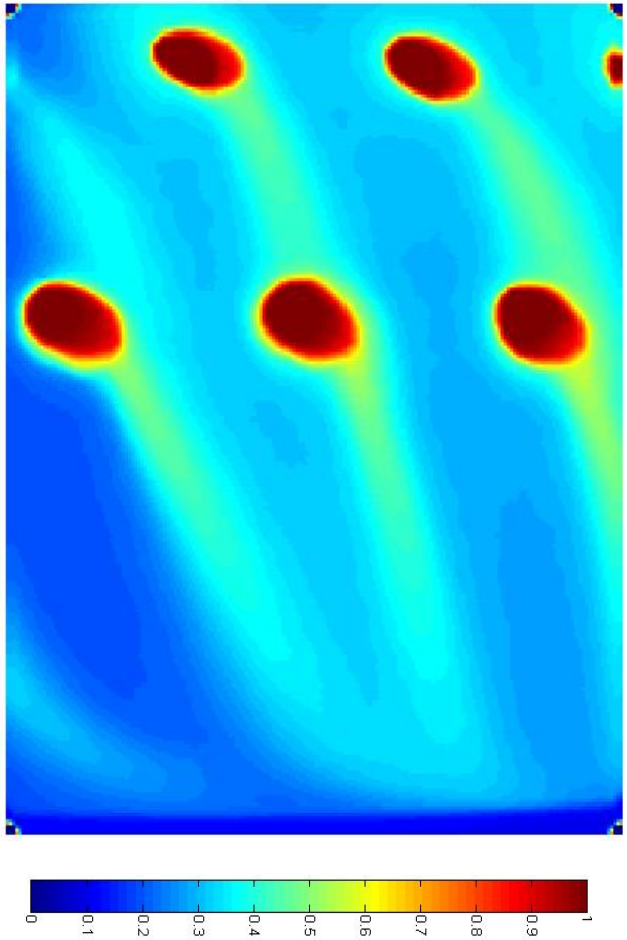

4.2.2 Cooling Film Geometry over the Cylinder Surface

Upon first inspection it can be noted that increasing the Blowing Ratio value between figures 4-2 – 4-15 results in an increased lateral shift of the coolant plumes (i.e. with increasing Blowing Ratio the coolant plumes tend to increasingly move towards the side of the cylinder). As the plumes divert towards one side of the cylinder, the other side receives insufficient cooling.

This effect has been expected, as the coolant ejection holes are directed at a lateral angle and increasing the BR value would increase the ratio of coolant to mainstream momentum, giving rise to more powerful jets of coolant in relation to the mainstream that will launch further away from the ejection orifice than jets with less momentum.

It can also be noted that coolant plumes ejected from holes at different angular locations have different geometries and core cooling effectiveness values. This of course has been expected, as the BR value is dependent on circumferential location of the ejection holes. The images however illustrate that an engine designer must work to find a compromise at which coolant ejection holes of different circumferential locations produce overall optimum film cooling coverage over entire turbine blade surface area. Infrared Thermography could be used to visually determine optimum cooling parameters over a turbine model and aid in turbine blade design and development.

4.2.3 Calculated Adiabatic Wall Effectiveness Distribution

From figures 4-2 – 4-15 it can be noted that Calculated Adiabatic Wall Effectiveness generally seems to increase with decreasing Blowing Ratio.

From figures 4-3 and 4-4 it can be seen that downstream of the $40°$ hole row, the coolant plume core with CAWE larger than 80% covers the largest area in comparison with all other images. This indicates that the highest values of local CAWE occur at a value of BR between 1.05 and 1.08 units. As these values lay very close to the lowest BR values tested, it may be necessary to perform additional experiments at lower BR to verify this finding.

While it is acknowledged that the images do not produce plots of absolute η_{aw} measurements, it is still possible to assess the consistency of experimental results produced by the IR camera. For this purpose a qualitative comparison between a $20°$ row cooling plume on figure 4-2 and a $40°$ row cooling plume on figure 4-3 can be made for example. These plumes have been calculated to be at blowing ratios of 1.04 and 1.05 units respectively and hence in theory should have similar CAWE. Qualitatively they do look similar on the images.

Cooling plumes with very similar properties could also be observed between $20°$ row at BR=1.15 (figure 4-3) and $40°$ row at BR=1.17 (figure 4-6), as well as $20°$ row at BR=1.39 (figure 4-5) and $40°$ row at BR=1.37 (figure 4-9). A further example of similarity would also exist between plumes from $20°$ row at BR=1.78 (figure 4-8) and $40°$ row at BR=1.77 (figure 4-14). These results suggest that infrared camera is within reason producing consistent results throughout the experimentation period.

4.2.4 Cooling Film Coverage

The most efficient film cooling method would not only result in high cooling effectiveness values across a turbine blade surface, but would also lead to a relatively even distribution of cooling effectiveness throughout that surface. That is to say that the cooling plumes should essentially blend into a single coolant film, which would stay attached to the entire surface effectively shielding it from hot mainstream engine flow.

From figures 4-13 – 4-15 it can be seen that the coolant plume coverage over the cylinder surface is very narrow in comparison to earlier figures with lower BR values. This implies that the jets at high BR values have a greater tendency to separate from the cylinder surface. These images illustrate the ability of IRT to visualise jet lift-off. In perspective this shows that IRT can be applied to determining the location and BR value at which lift-off occurs, when designing a new turbine blade, or assessing different coolant ejection hole profiles.

The core section of coolant plumes from the $20°$ row, ejected at a blowing ratio of 2.70 fall below 50% cooling effectiveness even before reaching the leading edge of the $40°$ row holes. That is to say that some of the highest BR values considered in this study would not only provide insufficient lateral spread of coolant across the cylinder, but may also not provide sufficient circumferential cooling between the cylinder hole rows, as the jets would tend to lift-off early without creating a circumferential cooling film. Images at such high BR values have been intentionally chosen to analyse coolant jet structure after lift-off, captured by a perpendicular nylon mesh (in later sections of this chapter).

As BR decreases, the coolant plume core appears to grow in size – the larger than 60% CAWE region reaches a width of nearly x/d=0.5 and a length of x/d=3 aft of the $40°$ row for blowing ratios below 1.17 (figure 4-8). This is still short and narrow compared with images seen for even lower blowing ratios (figures 4-2 – 4-6).

The core region of the coolant plumes generally tends to increase in size (in terms of both width and length), in addition to increasing in CAWE with decreasing BR across all fourteen figures. The coolant plumes appear to be closest to blending together into a single shield of coolant at lowest BR (figure 4-2), although they never actually join into this single shield across any of the experimental BR values.

This may mean that the optimum BR value for maximum surface coverage by the coolant is actually below those tested within this project. This may be confirmed with further experimental work and would require an air pump capable of producing coolant jets at smaller BR values. Regretfully, due to time constraints these experiments are outside the scope of this project. They can however form a good base for future studies.

4.3 Nylon Mesh Visualisation

4.3.1 Visualisation of Separated Coolant Jets

The effect of coolant jet lift-off can be observed from cylinder surface images, however it can be more clearly visualised and studied in more detail by analysis of coolant plume imprints on a nylon mesh surface positioned aft (downstream) of the coolant hole trailing edges.

As described in the previous chapter, the mesh was positioned at the following non-dimensional distances aft of the $-40°$ row holes trailing edges:

x/d	-1,	1,	3,	5

The $x/d = -1$ location implies that the mesh was actually located one x/d unit ahead (upstream) of the $-40°$ row holes trailing edges. This means it was located on the border of the leading edges of the $-40°$ row holes (or at a distance of $x/d = 2$ downstream of the $-20°$ row holes). Thus the mesh has been positioned at three different locations aft of both the $-40°$and $-20°$ coolant holes row and at one location aft of the $-20°$coolant holes row only.

Mesh locations at $x/d > 5$ have not been planned for experimentation. This is because directional emissivity of Rohacell is only assumed to be equal for viewing angles of up to $60°$ (as discussed in Chapter 2) and hence GCE values acquired at higher x/d locations would not be directly comparable with CAWE values seen in figures 4-2 – 4-15.

4.3.2 Comparison of Cylinder and Mesh Images

In order to prevent bowing near the cylinder surface, the legs of the mesh fence have been stretched away from each other and while maximum effort was made to ensure that the mesh would be as close to the cylinder surface as possible, the minimum distance was still approximately 2 millimetres (which varied along the mesh length due to its hexagonal fibre pattern).

As such, the data that can be observed on the nylon mesh images immediately next to the cylinder surface is not a direct representative of the data observed on the cylinder surface at the exact location of the mesh (due to the mesh displacement (elevation) of ~2mm above the cylinder surface).

In the following sections, cross-references between the mesh images and the cylinder surface images are often made in order to assess the consistency of the experimental data (and feasibility of IRT in turbine blade visualisation). During this process the CGE values at the mesh and CAWE values at the cylinder surface are compared to assess the difference in calculated effectiveness that the two separate MATLAB code algorithms produce. Thus it can be assessed whether the surface and mesh effectiveness readings are in agreement and whether the camera produces consistent results.

The width of a coolant jet's cross-section on the mesh is compared with the width of a coolant plume observed on the cylinder surface. As a jet does not have immediate distinct boarders and rather blends with the surrounding environment, an arbitrary value (e.g. 60% calculated effectiveness) is often taken to serve as guidance 'bench-mark' for this purpose. Therefore the width of the coolant plume region in excess of 60% CAWE at x/d=3 can be compared with width of the coolant jet's cross-section region in excess of 60% CGE at x/d=3 for example.

4.3.3 Camera Position and Image Preparation

The camera has been positioned in such a way that the images produced capture the cylinder surface, the mesh and the space between them. Since the cylinder and the mesh have different thermal emissivity values and require separate code algorithms for data processing, the cylinder surface has been cropped out of mesh images. The mesh area that does not capture the coolant imprints has also been cropped. This enabled to produce large figures with detailed jet cross-section images.

Only two jet imprints per frame have been left for representation. Having two jet imprints side-by-side enables to comparatively assess symmetry, geometrical and positional changes of the cross-sections.

4.3.4 Identifying Coolant Jet Lift-off

The coolant jet is visualised on the mesh as an imprint with different colours representing different values of CGE. The jet generally tends to have a hot core, where the CGE peaks. This value falls with increasing lateral distance from the jet cross-section's centre.

A jet that is considered to be lifting-off, or have lifted-off a surface is subjected to greater interaction with the mainstream flow and essentially greater diffusion. As such there is no immediate jet boundary. Instead the CGE converges to zero gradually with increasing lateral distance from the jet cross-section's centre.

For the purposes of jet lift-off analysis the author refers to separation of the hot jet core from the cylinder surface. In order to identify the "boundary" of the core region, an arbitrary value of CGE (e.g. 60%) is often used, as it has been previously discussed.

4.4 Nylon Mesh Images at x/d = - 1

The following nylon mesh images have been taken for a mesh positioned at a non-dimensional distance of x/d = -1. The mesh was located 1 nozzle diameter ahead of the $40°$ hole row trailing edge (at its leading edge). As a result, the images demonstrate the imprint of the coolant jets ejected from the $20°$ hole row only. The images represent the Calculated Gas Effectiveness distribution and the scale is set between 0 and 1 units (0 and 100% CGE).

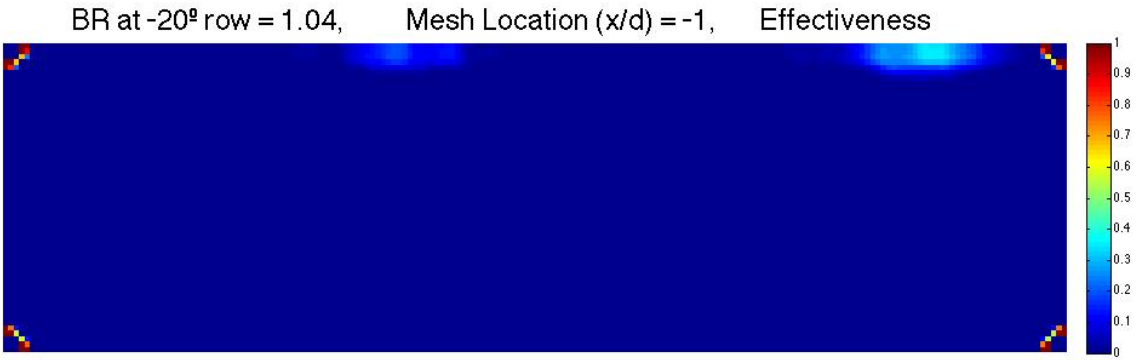

Figure 4-16 – Mesh at (x/d) = -1, BR_{20}=1.04

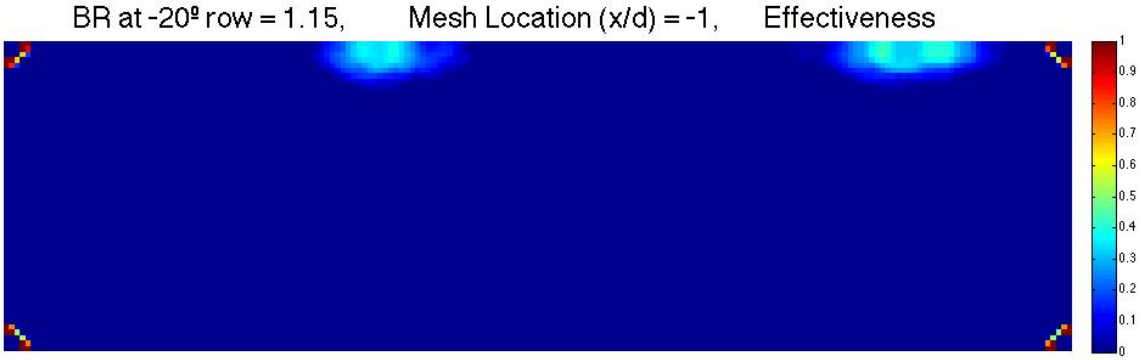

Figure 4-17 – Mesh at (x/d) = -1, BR_{20}=1.15

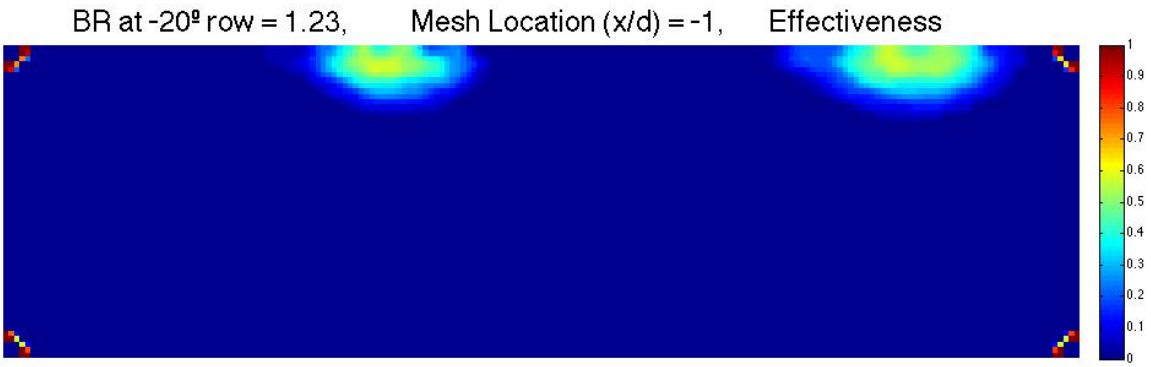

Figure 4-18 – Mesh at (x/d) = -1, BR_{20}=1.23

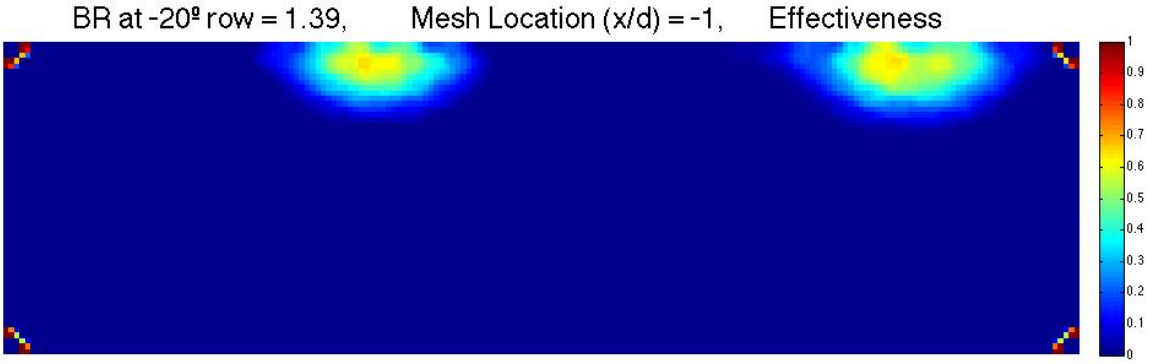

Figure 4-19 – Mesh at (x/d) = -1, BR_{20}=1.39

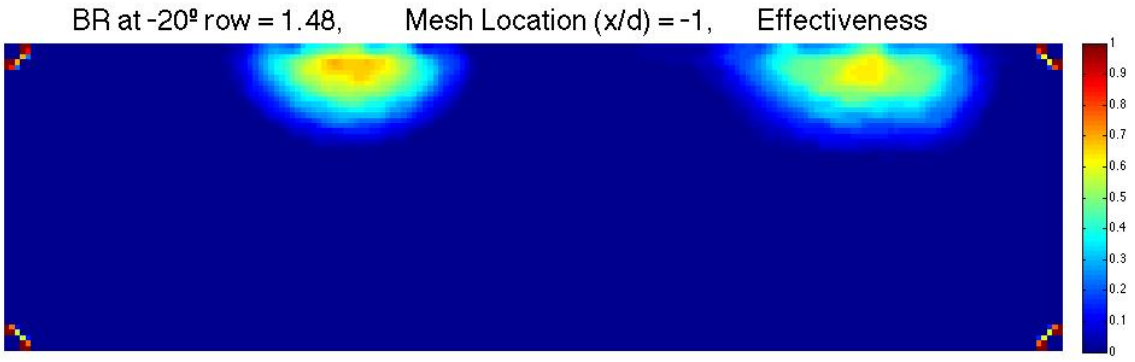

Figure 4-20 – Mesh at (x/d) = -1, BR_{20}=1.48

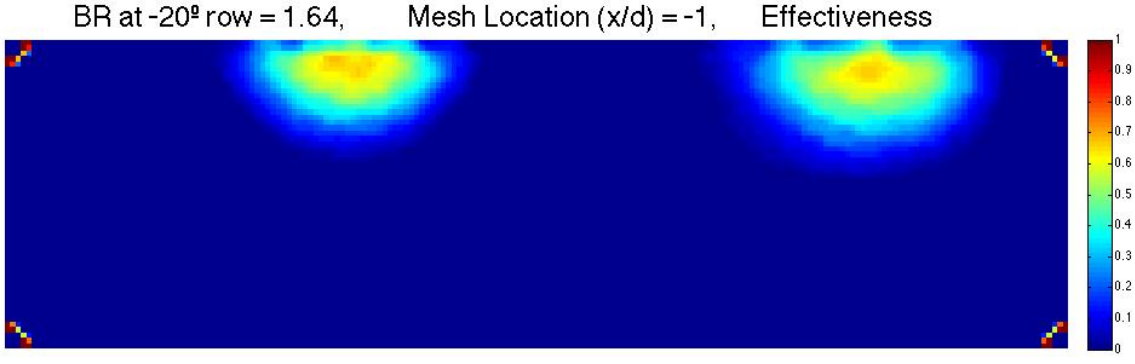

Figure 4-21 – Mesh at (x/d) = -1, BR_{20}=1.64

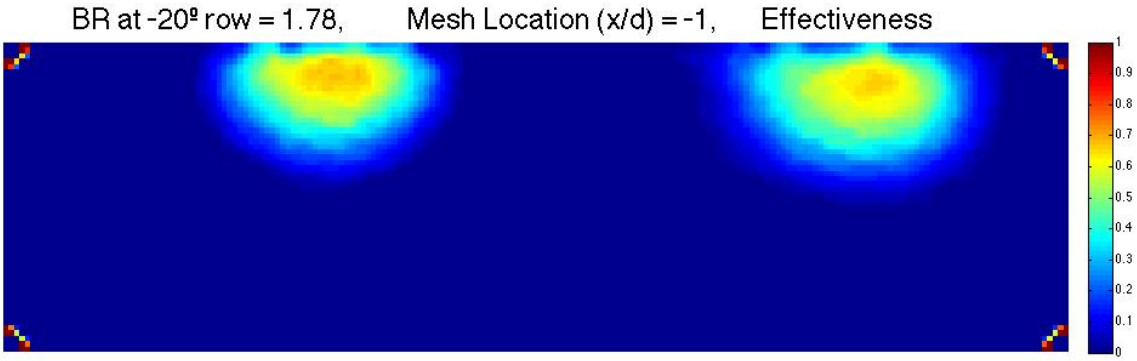

Figure 4-22 – Mesh at (x/d) = -1, BR_{20}=1.78

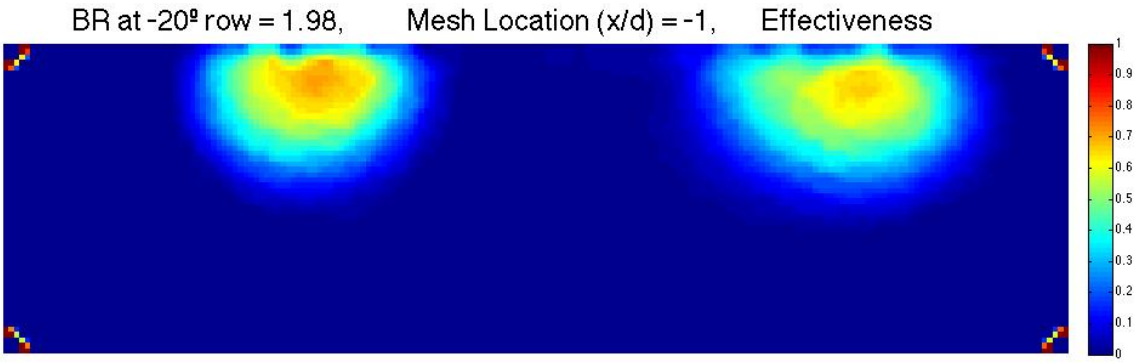

Figure 4-23 – Mesh at (x/d) = -1, BR_{20}=1.98

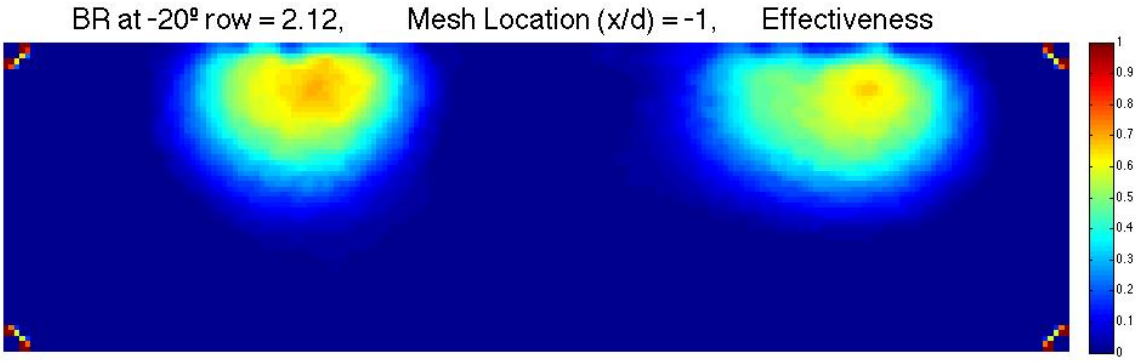

Figure 4-24 – Mesh at (x/d) = -1, BR_{20}=2.12

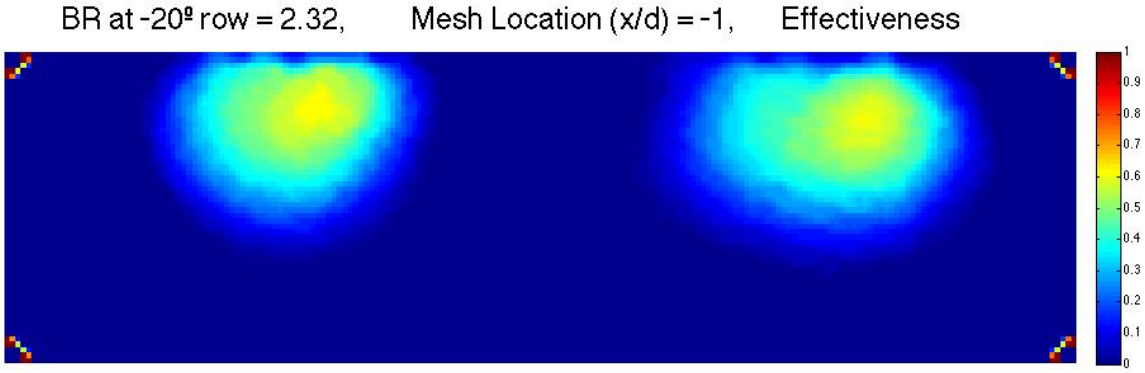

Figure 4-25 – Mesh at (x/d) = -1, BR_{20}=2.32

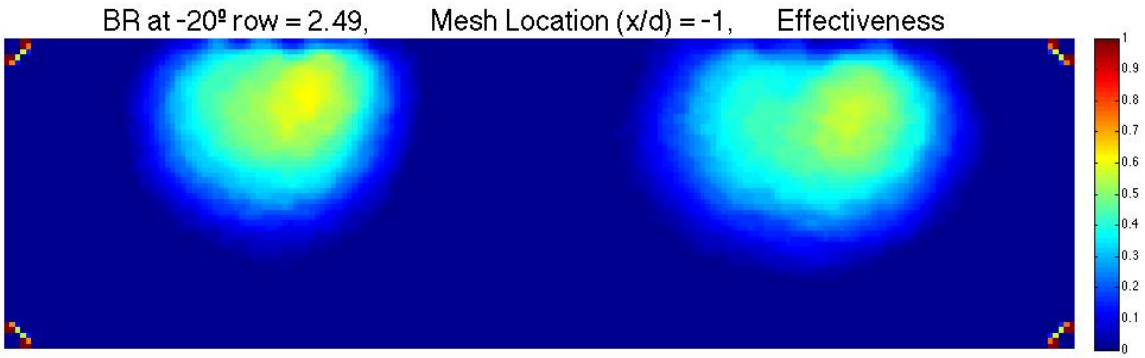

Figure 4-26 – Mesh at (x/d) = -1, BR_{20}=2.49

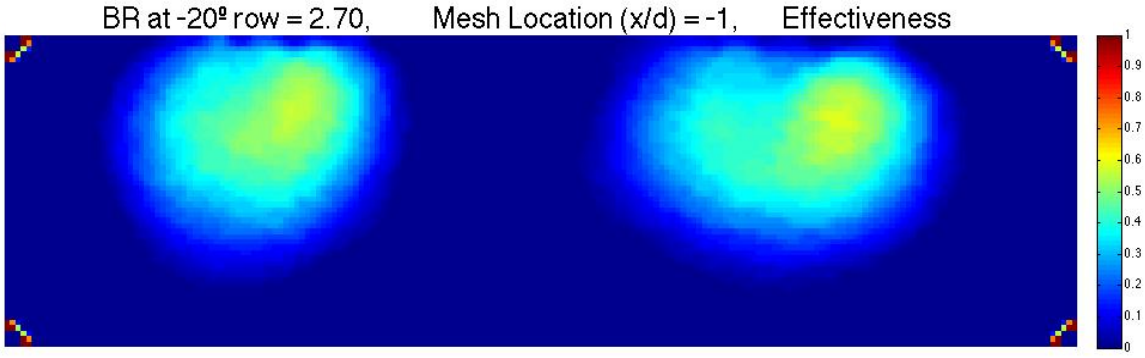

Figure 4-27 – Mesh at (x/d) = -1, BR_{20}=2.70

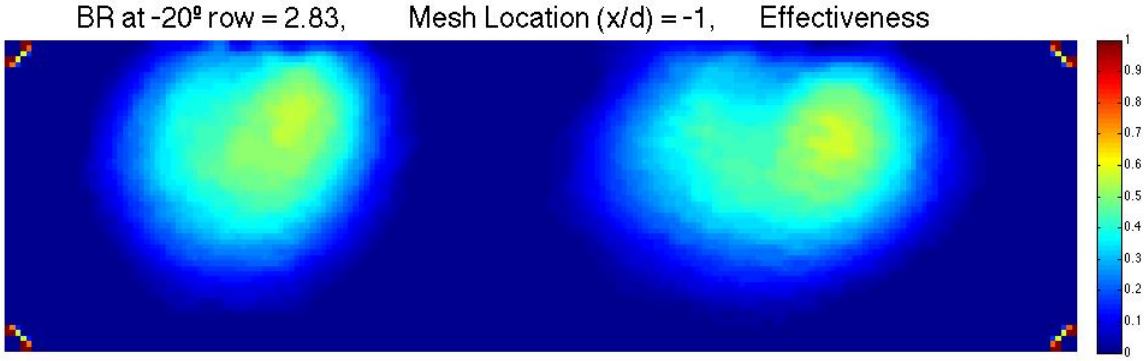

Figure 4-28 – Mesh at (x/d) = -1, BR_{20}=2.83

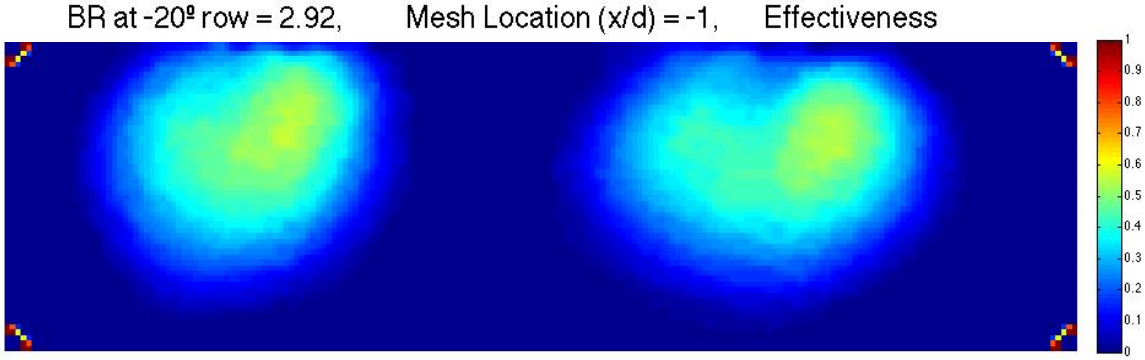

Figure 4-29 – Mesh at (x/d) = -1, BR_{20}=2.92

4.4.1 Discussion of the Mesh Images at x/d = -1

From figures 4-16 – 4-29 it can be seen that increasing the Blowing Ratio increases the coolant jets' tendency to lift-off from the surface. The coolant plume core remains attached to the cylinder surface at BR=1.15 (and lower BR values). Further increasing BR to 1.23 results in the plume region of 60% CGE detaching from the surface and being visible on the mesh. The plume core region of 70% cooling effectiveness becomes visible on the mesh at BR=1.39 and seems to detach form cylinder surface at BR values between 1.48 and 1.64. The jets grow in size and move further away from the cylinder surface with increasing BR values. They appear to completely detach form the cylinder surface at BR around 1.98 units. Any further increase of Blowing Ratio results in increased vertical and lateral jet movement. The jets begin to mix with the mainstream flow and diffuse. As a result it can be noted that average observed CGE of the jets begins to decrease when BR value is increased higher than 1.98 units.

4.4.2 Kidney Shape Vortices

The counter-rotating vortex structure of kidney vortices produce lift in a direction angled to the cylinder surface. This results in increased separation of one side of the jet from the cylinder surface. Therefore the coolant jets do not appear to lift off the cylinder surface as symmetrical circles, but tend to take prolonged and curving (kidney shapes) inclined at an angle to the cylinder surface. This lift force encourages the film cooling jet to separate from a turbine blade surface and into the gas turbine mainstream. Kidney vortices are therefore detrimental to turbine blade film cooling effectiveness (due to decreased film coverage of turbine blades) and gas turbine operating efficiency (due to increased mixing of cold coolant air with hot mainstream).

Vortices resembling kidney shapes can be seen on all images at Blowing Ratios of 1.98 or higher. Although the coolant ejection holes are circular, asymmetric coolant imprints of such shapes have been expected for a jet in a cross flow and previously described in chapter 2.

The vortices become much more distinct when they clearly separate from the picture edge (BR = 2.7) and are more clearly shaped with increasing BR value. It seems that the kidney vortices tend to rotate with increasing BR value. Again, this is reflects their theoretical behavior [19].

4.5 Nylon Mesh Images at Positive x/d Locations (1, 3, 5)

The following section demonstrates how the blowing ratio affects coolant jets at non-negative x/d locations (1, 3, and 5). In the previous section the images represented coolant jets ejected from the $20°$ coolant hole row only. Thus each of the two imprints per figure was representative of a singular coolant jet ejected from a singular coolant hole.

The images presented in the subsequent sections differ because they represent flow patterns that are a mixture of two coolant jets (each of the two imprints per figure is a mixture of a jet ejected from a $40°$ row hole, and an upstream $20°$ row hole). Local BR values at the $40°$ row are also lower than those at the $20°$ row for the same power setting of the air pump. The images are presented in the same way for ease of comparison.

4.5.1 Nylon Mesh Images at x/d = 1

The following nylon mesh images have been taken for a mesh positioned at a non-dimensional distance of x/d=1 aft of the $40°$ coolant ejection hole row. The images represent the Calculated Gas Effectiveness distribution and the scale is set between 0 and 1 units (0 and 100% effectiveness).

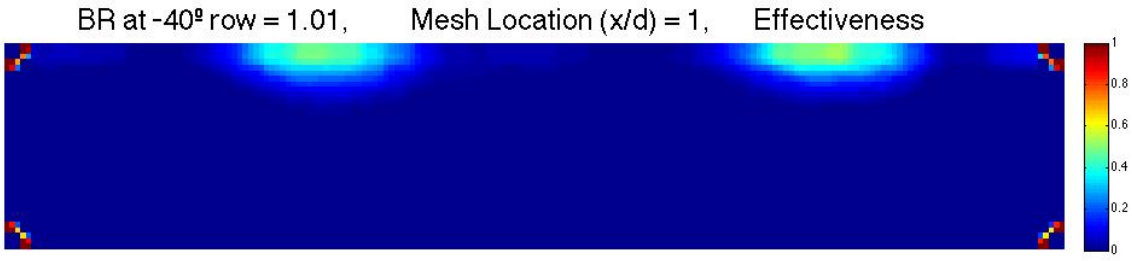

Figure 4-30 – Mesh at (x/d) = 1, BR_{40}=1.01

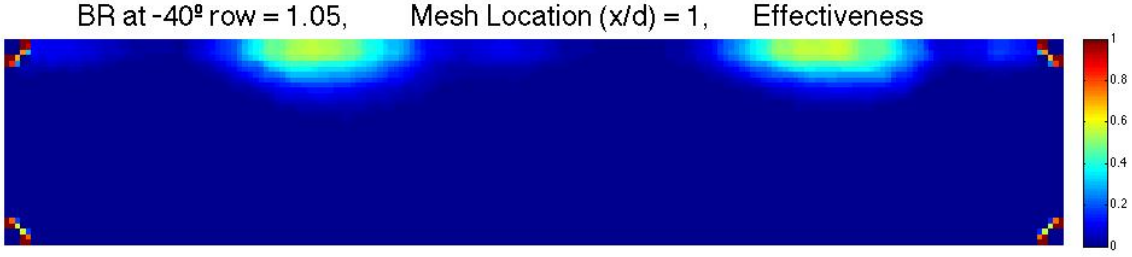

Figure 4-31 – Mesh at (x/d) = 1, BR_{40}=1.05

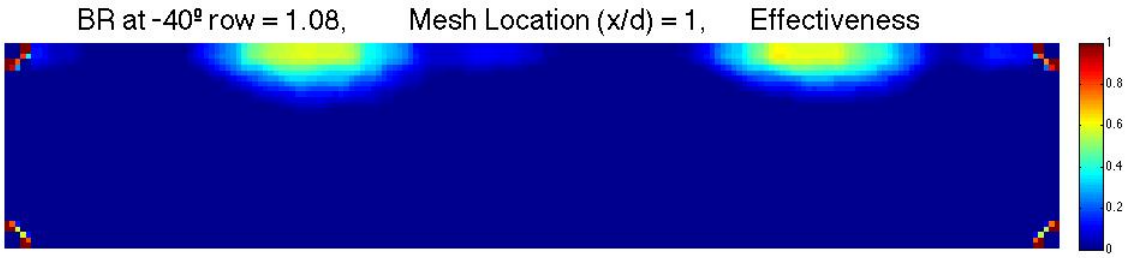

Figure 4-32 – Mesh at (x/d) = 1, BR_{40}=1.08

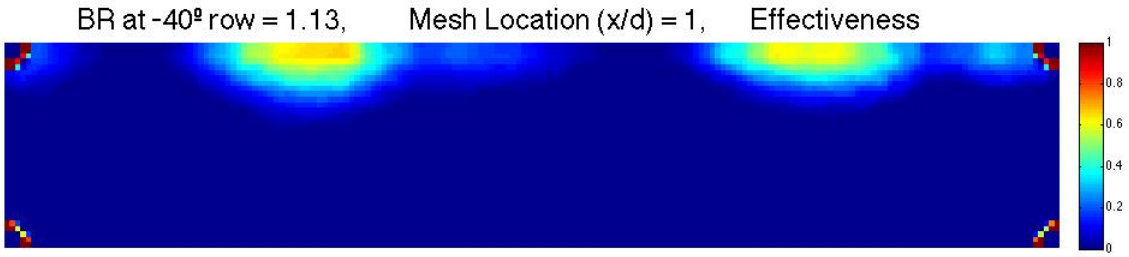

Figure 4-33 – Mesh at (x/d) = 1, BR_{40}=1.13

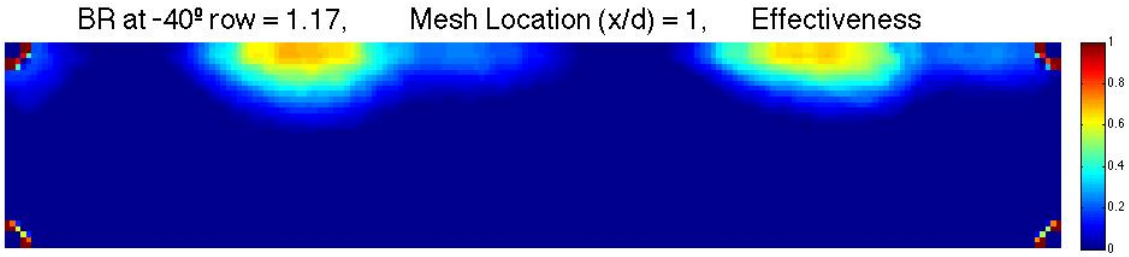

Figure 4-34 – Mesh at (x/d) = 1, BR_{40}=1.17

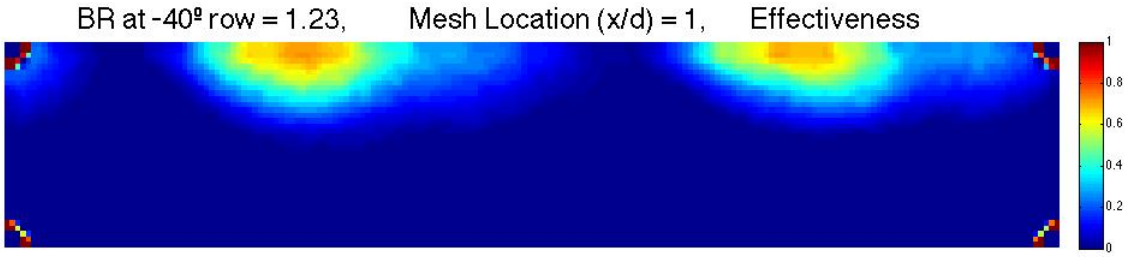

Figure 4-35 – Mesh at (x/d) = 1, BR_{40}=1.23

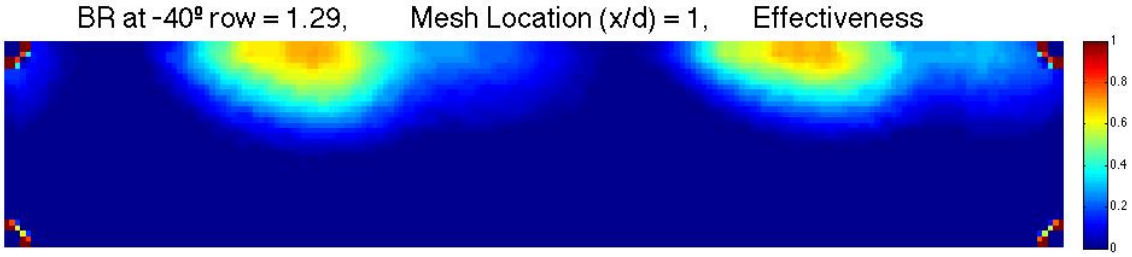

Figure 4-36 – Mesh at (x/d) = 1, BR_{40}=1.29

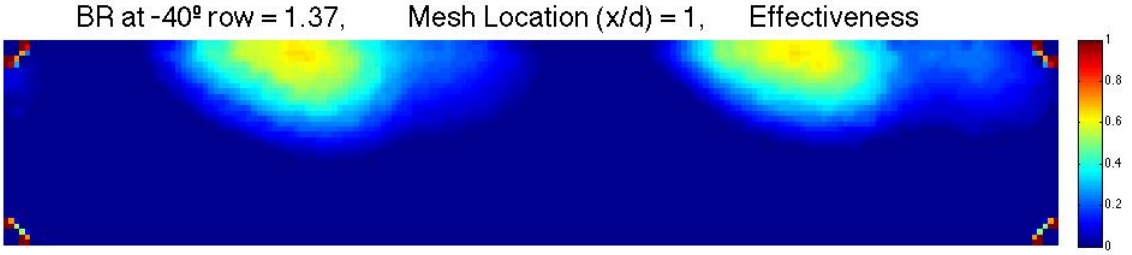

Figure 4-37 – Mesh at (x/d) = 1, BR_{40}=1.37

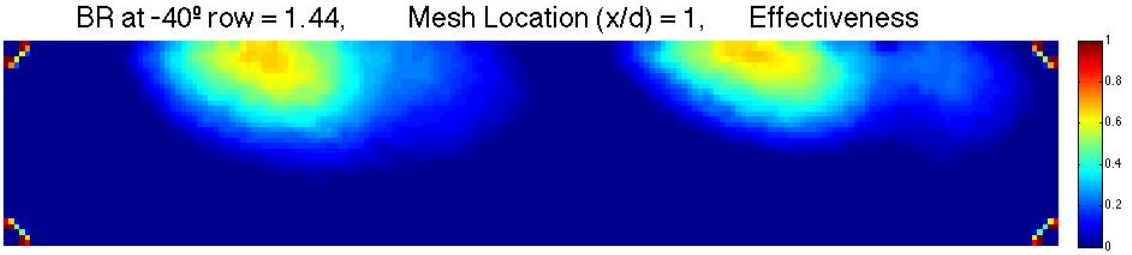

Figure 4-38 – Mesh at (x/d) = 1, BR_{40}=1.44

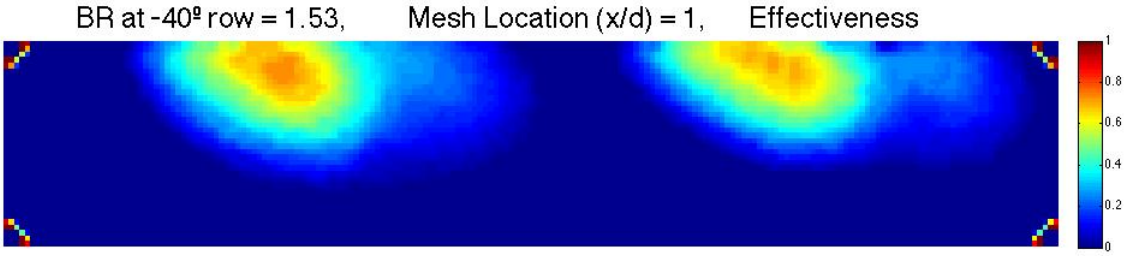

Figure 4-39 – Mesh at (x/d) = 1, BR_{40}=1.53

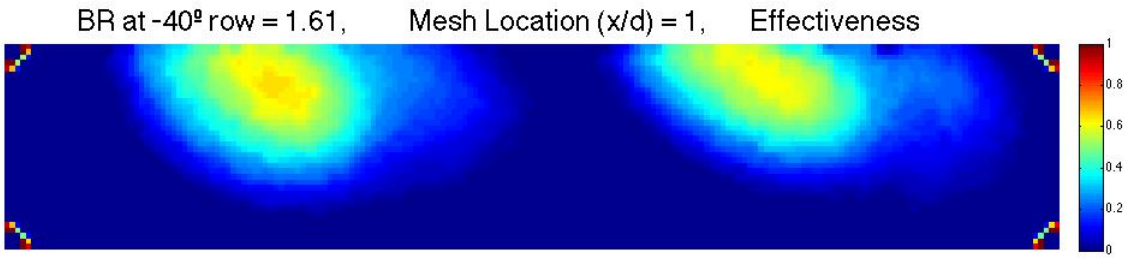

Figure 4-40 – Mesh at (x/d) = 1, BR_{40}=1.61

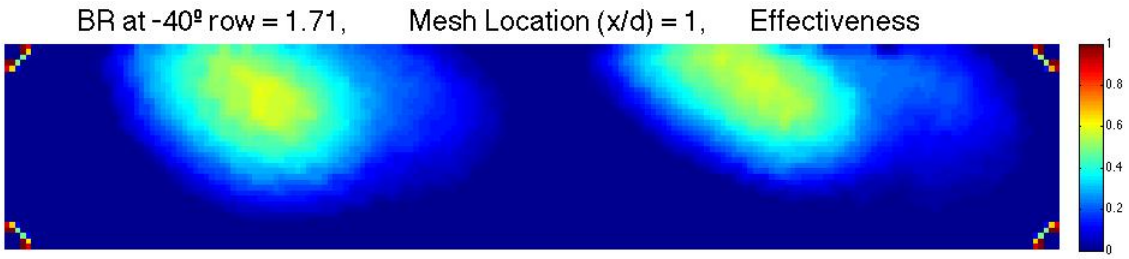

Figure 4-41 – Mesh at (x/d) = 1, BR_{40}=1.71

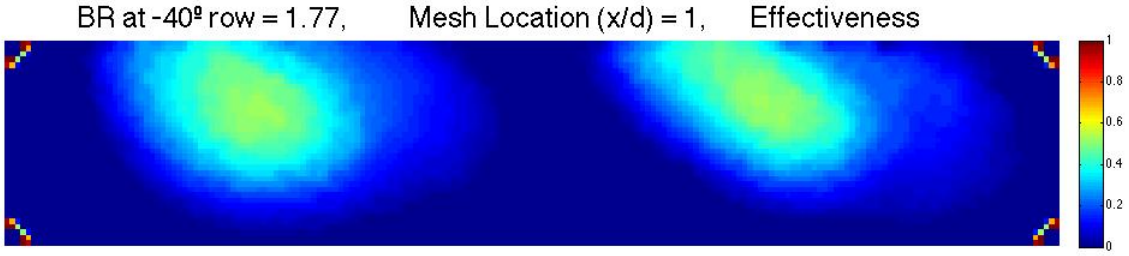

Figure 4-42 – Mesh at (x/d) = 1, BR_{40}=1.77

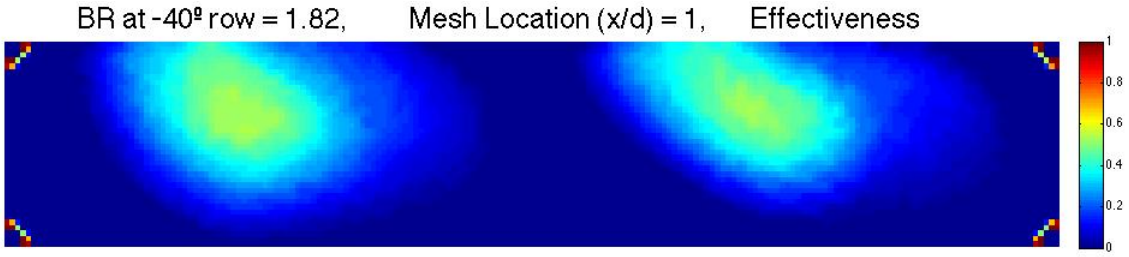

Figure 4-43 – Mesh at (x/d) = 1, BR_{40}=1.82

4.5.2 Discussion of the Mesh Images at x/d = 1

As it can be seen at BR = 1.01 (figure 4-30) the jet is still mainly attached to the cylinder surface. The visible core of the jet here can be approximated to be at a CGE value of 60%. By comparing it with figure 4-2 and analysing the line at x/d=1 aft of the $40°$ row trailing edge, it can be seen that the core of the cooling plume on the cylinder surface at this distance can be approximated to 80% CAWE. These values are not expected to be identical, as they are taken approximately 2mm above the surface and directly on the cylinder surface respectively (to which the jet is still attached).

Generally, as the BR value is increased from figure 4-30 to figure 4-43, it can be clearly seen that the coolant jet begins to lift off the cylinder surface to such an extent that its core almost loses contact with the cylinder surface. This is consistent with the pattern visualised in figures 4-2 – 4-15 at a distance of x/d=1 aft of the $40°$ row.

As the coolant jet begins to lift-off from the cylinder surface, its hot core region lifts above the surface of the cylinder and becomes visible on the mesh. Hence increasing the BR value from 1.01 to 1.53 (figures 4-30 – 4-39) results in the coolant imprint appearing to grow in size (lifting above the cylinder surface) and getting hotter (the coolant jet core with higher values of CGE becoming visible on the mesh). The coolant jet core CGE peaks at BR = 1.53 (figure 4-39) with a value of approximately 75%. The jet region nearest to the cylinder surface is approximately at 70% CGE (at 2mm above cylinder surface), which is close to the surface value of 60% CAWE at the respective location and BR value. The 75% CGE of the core region (which is diffusing due to interaction and mixing with cold mainstream flow) is also close to the 80% CAWE, which can be observed on the cylinder surface before jet begins to separate (e.g. BR = 1.01).

Any further increase in the blowing ratio results in the jets diffusing more strongly: the jet imprints grow in size, they move further above the cylinder

surface and shift laterally to one side of the cylinder. The core region cools due to mixing with the mainstream flow.

When the BR value peaks at 1.82 (figure 4-43), the CGE values of the jet area nearest to the cylinder wall can be approximated to 45% and is narrow (about 0.5d), which is consistently close to the observations made for respective surface image conditions (50% CAWE and 0.5d width).

4.5.3 Nylon Mesh Images at x/d = 3

The following nylon mesh images have been taken for a mesh positioned at a non-dimensional distance of x/d = 3 aft of the $40°$ coolant ejection hole row. The scale is set between 0 and 1 units (0 and 100% CGE) as previously.

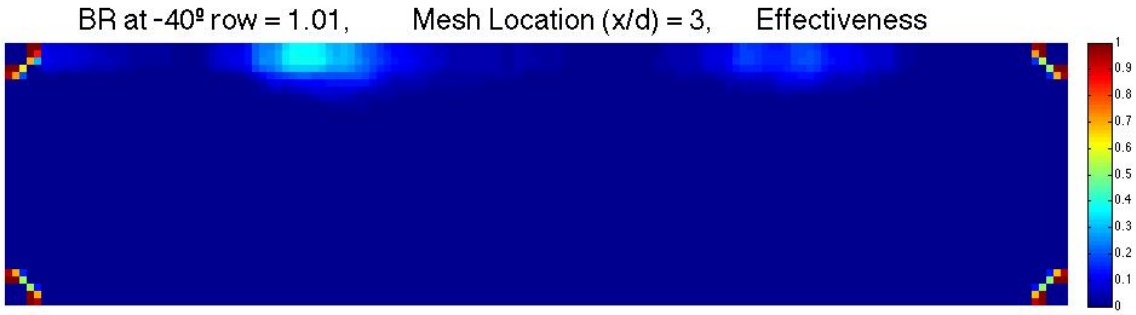

Figure 4-44 – Mesh at (x/d) = 3, BR_{40}=1.01

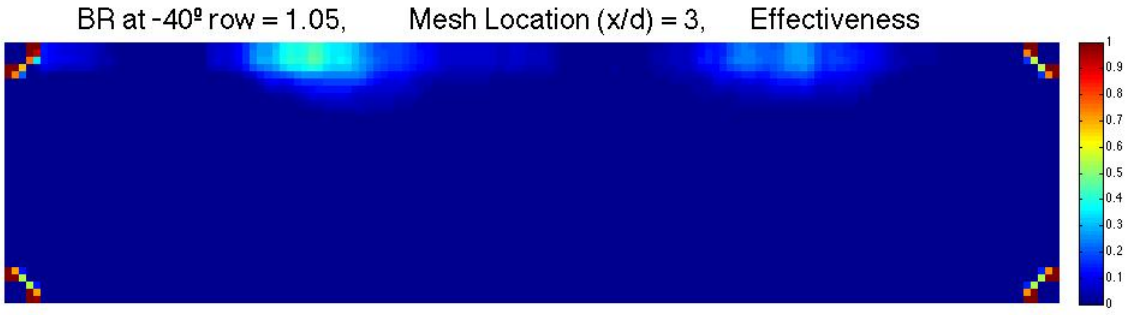

Figure 4-45 – Mesh at (x/d) = 3, BR_{40}=1.05

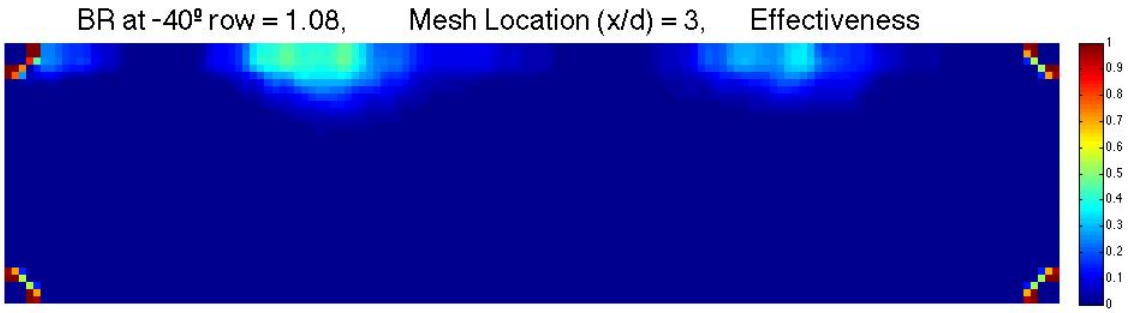

Figure 4-46 – Mesh at (x/d) = 3, BR_{40}=1.08

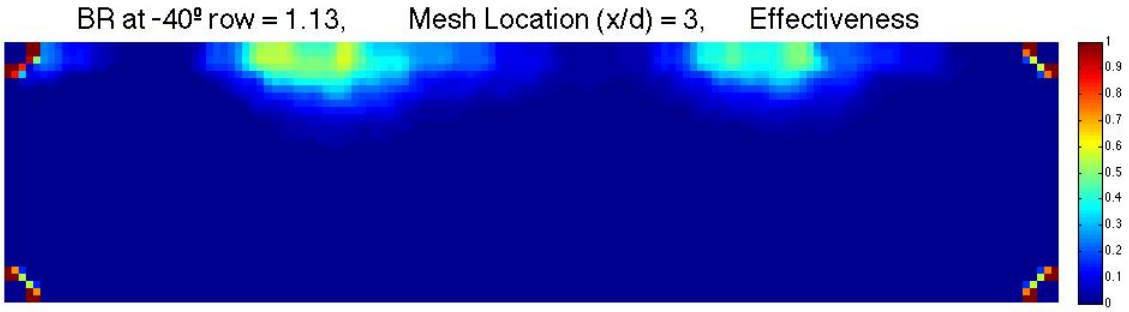

Figure 4-47 – Mesh at (x/d) = 3, BR_{40}=1.13

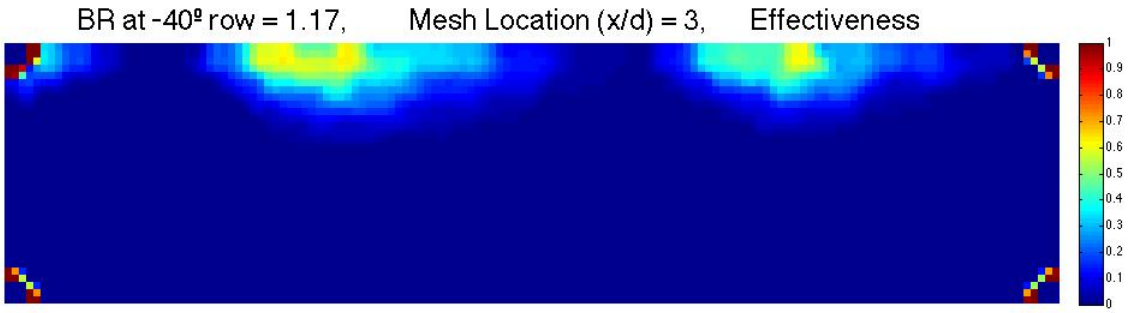

Figure 4-48 – Mesh at (x/d) = 3, BR_{40}=1.17

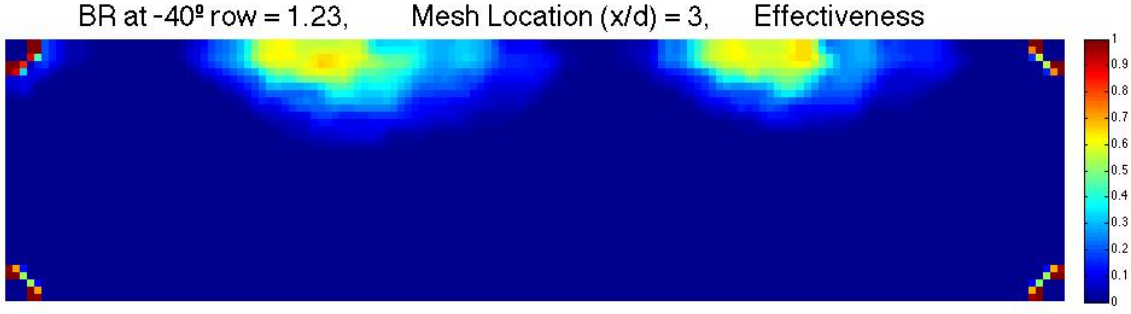

Figure 4-49 – Mesh at (x/d) = 3, BR_{40}=1.23

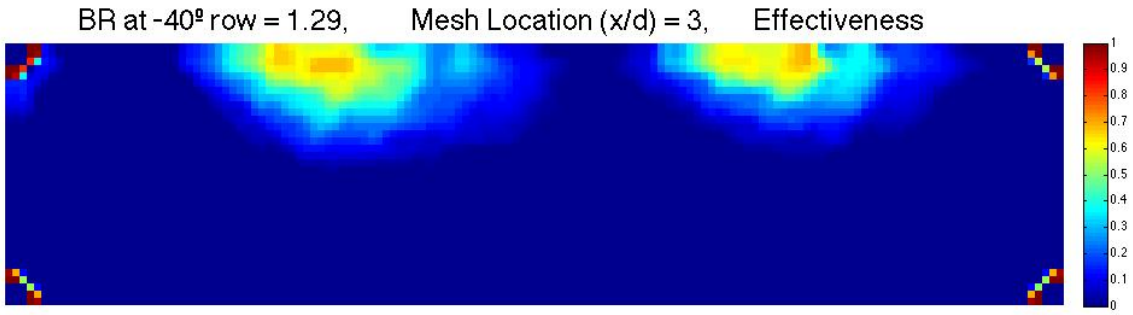

Figure 4-50 – Mesh at (x/d) = 3, BR_{40}=1.29

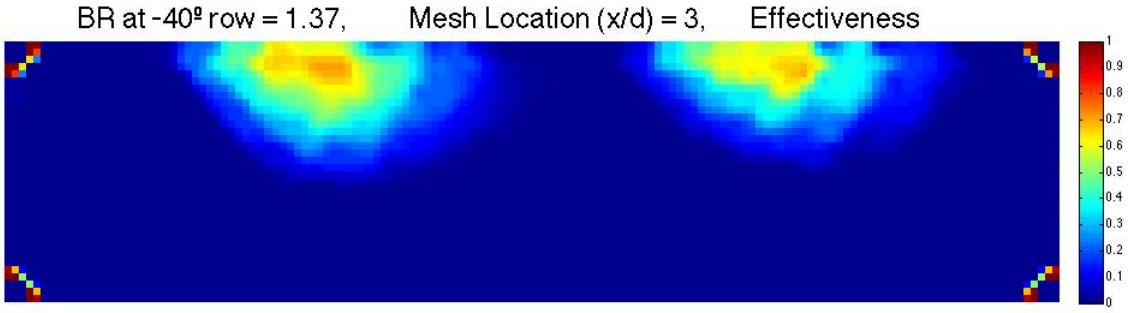

Figure 4-51 – Mesh at (x/d) = 3, BR_{40}=1.37

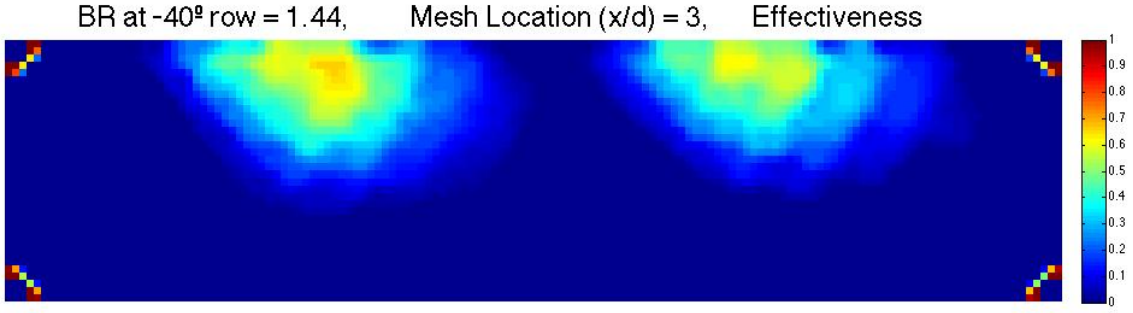

Figure 4-52 – Mesh at (x/d) = 3, BR_{40}=1.44

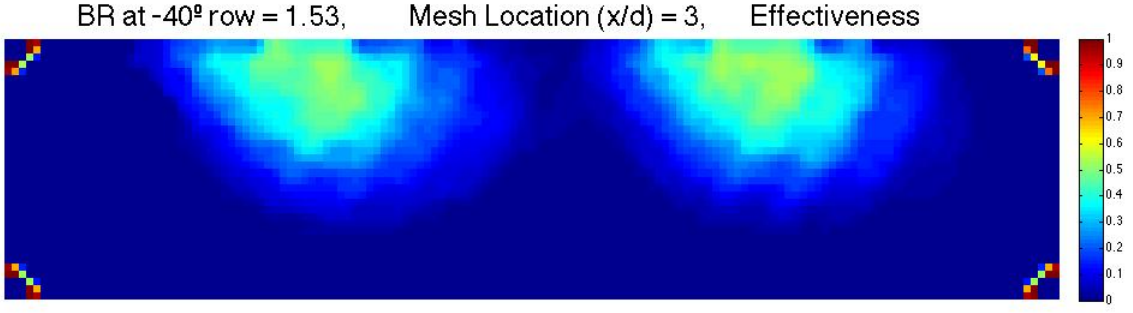

Figure 4-53 – Mesh at (x/d) = 3, BR_{40}=1.53

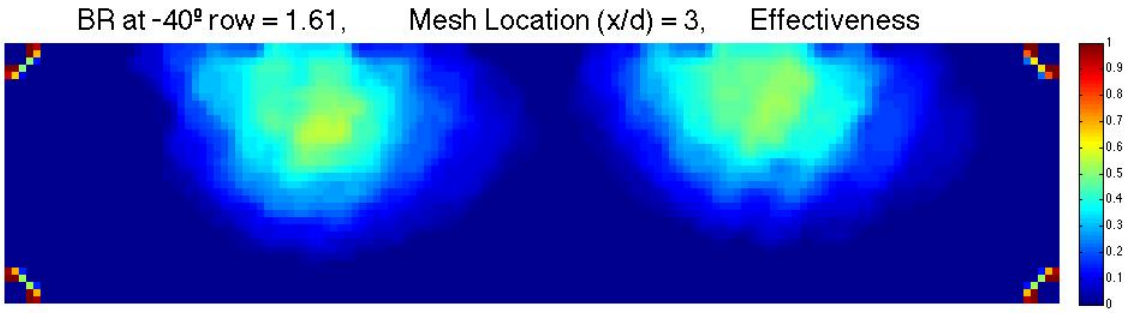

Figure 4-54 – Mesh at (x/d) = 3, BR_{40}=1.61

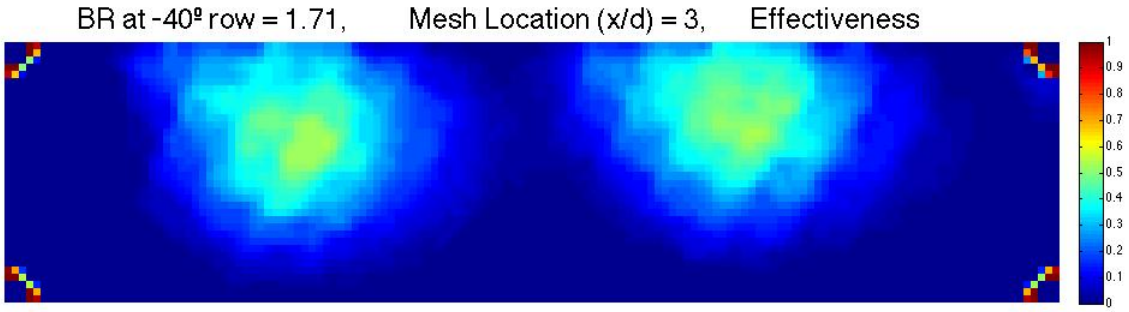

Figure 4-55 – Mesh at (x/d) = 3, BR_{40}=1.71

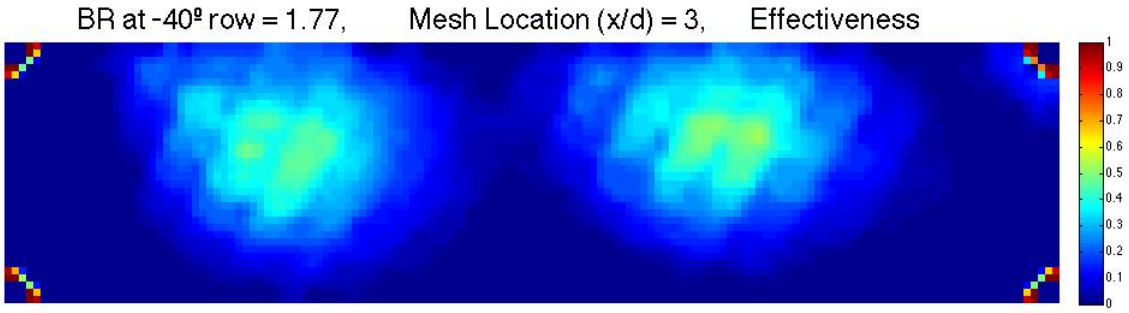

Figure 4-56 – Mesh at (x/d) = 3, BR_{40}=1.77

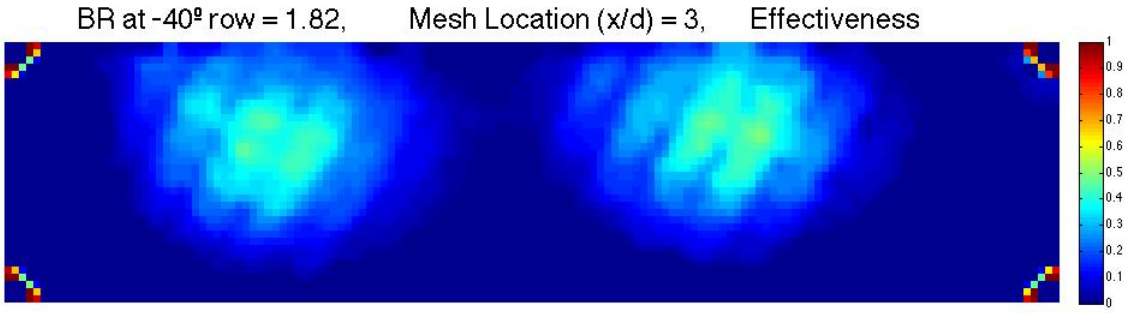

Figure 4-57 – Mesh at (x/d) = 3, BR_{40}=1.82

4.5.4 Discussion of the Mesh Images at x/d = 3

Analysing the CGE images of the mesh at x/d = 3 (figures 4-44 – 4-57) it can be seen that increasing the blowing ratio results in increased tendency of the coolant jets to lift-off higher above the cylinder surface. As the jets lift-off more, they tend to diffuse into the mainstream more, which leads to reduced core CGE values at higher blowing ratios.

At BR values between 1.01-1.05 (figures 4-44 – 4-45) the maximum CGE value that can be observed on the nylon mesh near the cylinder surface is in the region of 40%. At these BR values the jet remains largely attached to the cylinder surface. Hence the visible 40% CGE is observed at around 2mm above the cylinder wall and is not a representative of the jet core values.

The jet core CAWE at low BR - when the jet remains attached to the cylinder are approximately 70% at x/d = 3. At BR values between 1.23-1.44 (figures 4-49 – 4-52), core CGE values of around 70% can be observed on the mesh. The coolant jet core gradually moves vertically away from the cylinder wall with increasing BR and laterally to the side of the cylinder.

By analysis of the surface images, this hot core region is observed to detach from the cylinder surface at approximately BR = 1.53 (figure 4-11) (CAWE on the cylinder surface is around 50% at this BR value). From the corresponding mesh image (figure 4-53) it can be seen that although a 60% CGE core region is visible on the mesh, the CGE value observed on the image edge closest to the cylinder surface is also in the region of 50%.

Increasing BR further to 1.71-1.82 (figures 4-55 – 4-57) results in the core CGE gradually declining to 50% as the jet increasingly diffuses. The CGE values observed on the mesh nearest to the cylinder wall are in the region of 30%. This is lower, but close to the surface readings of 40% CAWE observed on the cylinder surface images (figure 4-13 – 4-15).

4.5.5 Nylon Mesh Images at x/d = 5

The following nylon mesh images have been taken for a mesh positioned at a non-dimensional distance of x/d = 5 aft of the $40°$ coolant ejection hole row. The scale is set between 0 and 1 units (0 and 100% CGE) as previously.

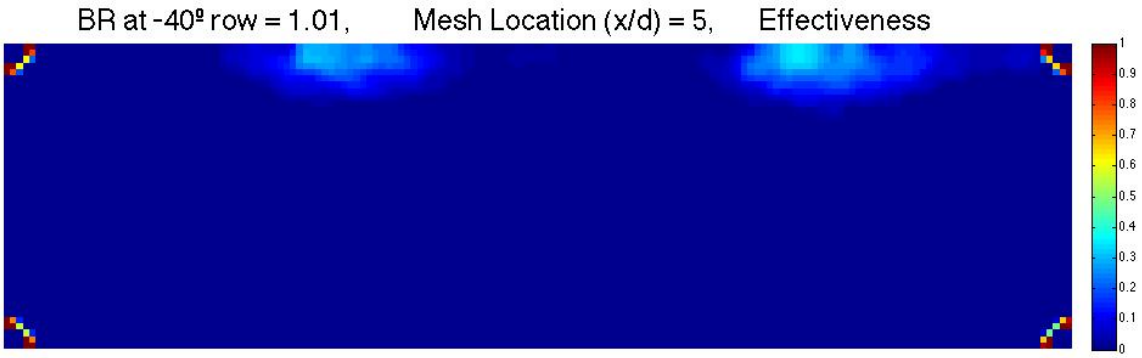

Figure 4-58 – Mesh at (x/d) = 5, BR_{40}=1.01

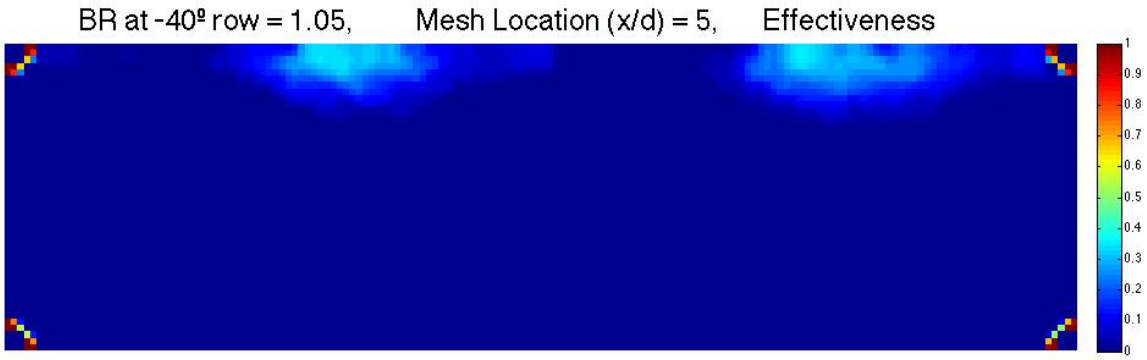

Figure 4-59 – Mesh at (x/d) = 5, BR_{40}=1.05

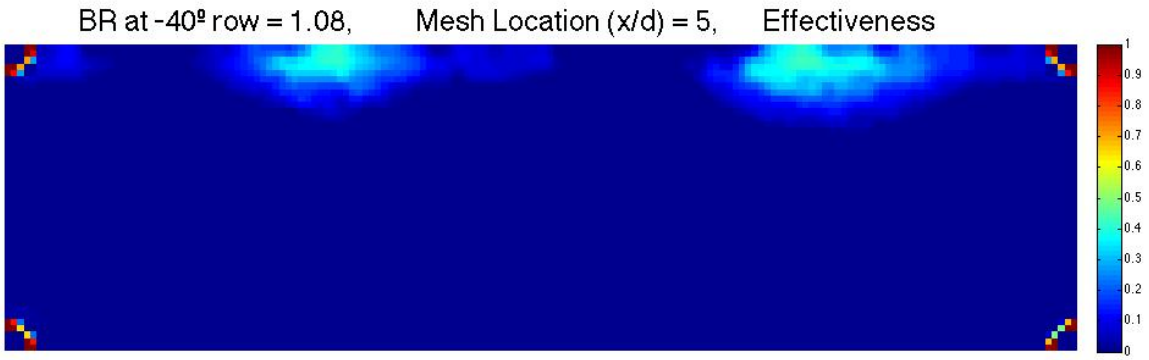

Figure 4-60 – Mesh at (x/d) = 5, BR_{40}=1.08

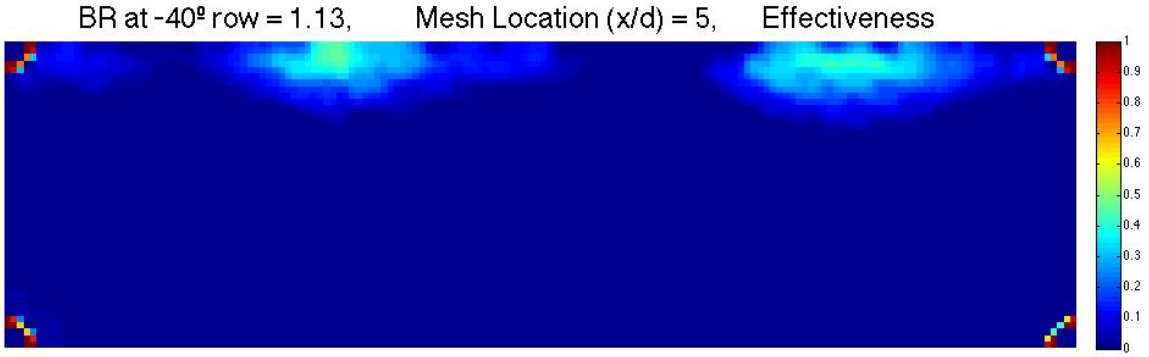

Figure 4-61 – Mesh at (x/d) = 5, BR_{40}=1.13

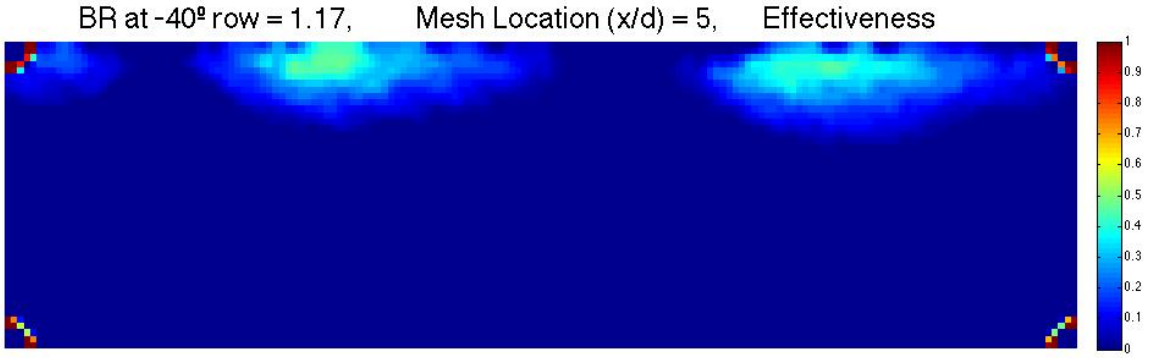

Figure 4-62 – Mesh at (x/d) = 5, BR_{40}=1.17

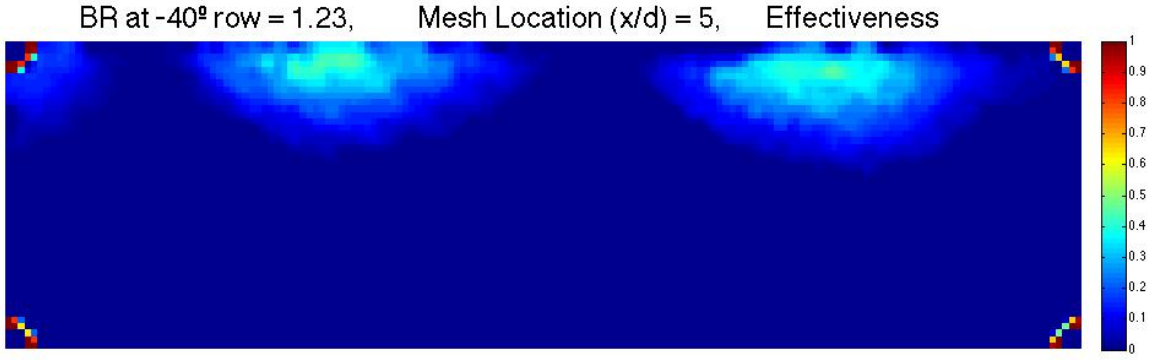

Figure 4-63 – Mesh at (x/d) = 5, BR_{40}=1.23

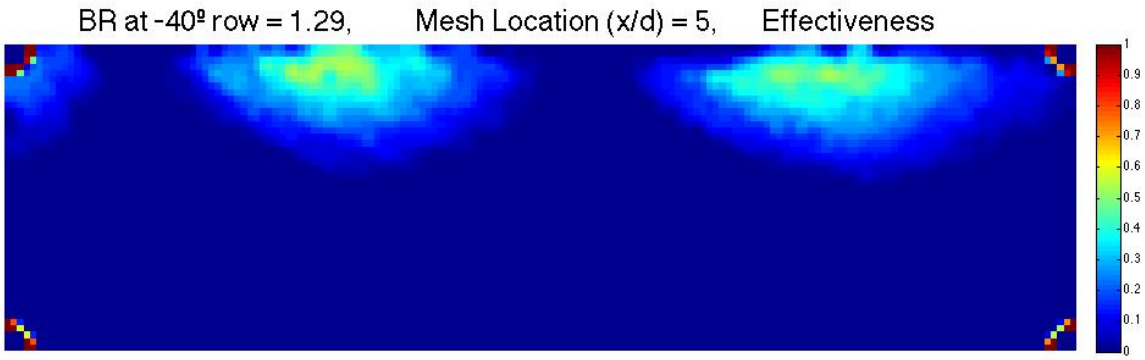

Figure 4-64 – Mesh at (x/d) = 5, BR_{40}=1.29

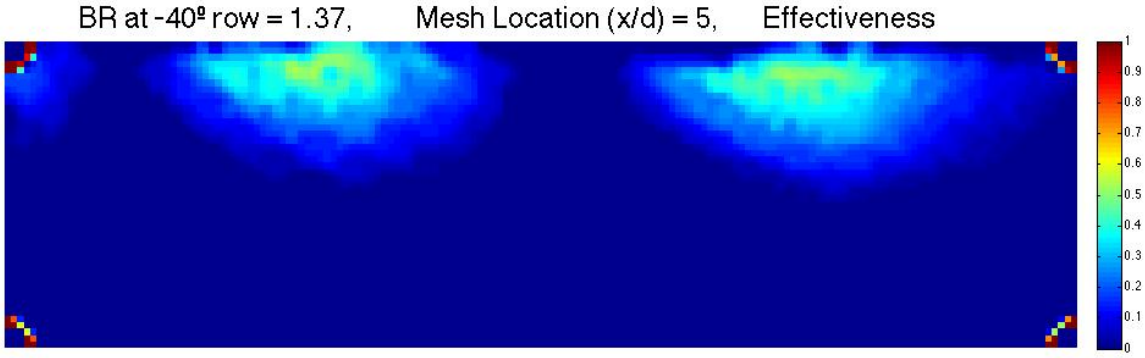

Figure 4-65 – Mesh at (x/d) = 5, BR_{40}=1.37

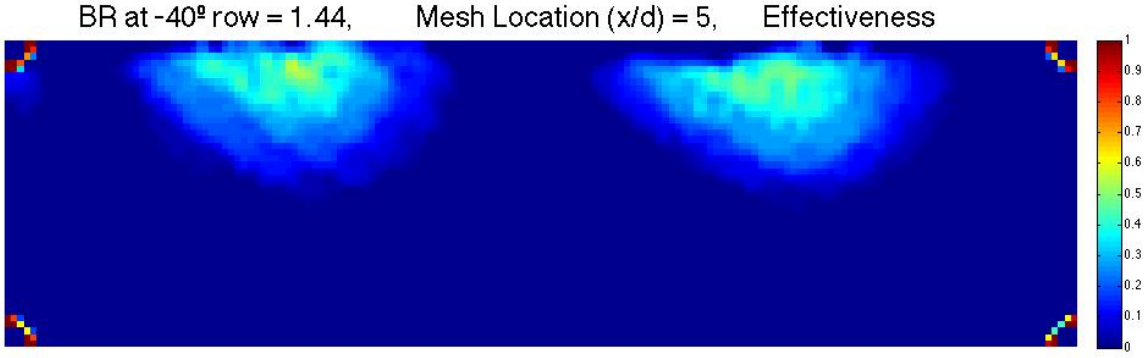

Figure 4-66 – Mesh at (x/d) = 5, BR_{40}=1.44

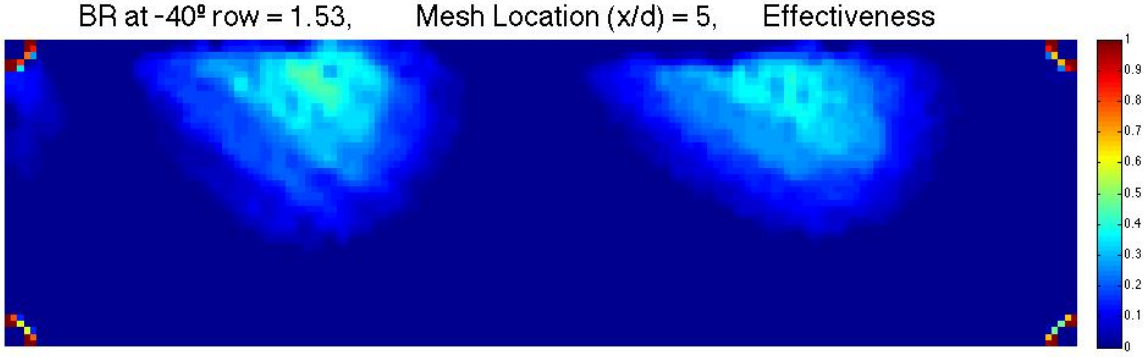

Figure 4-67 – Mesh at (x/d) = 5, BR_{40}=1.53

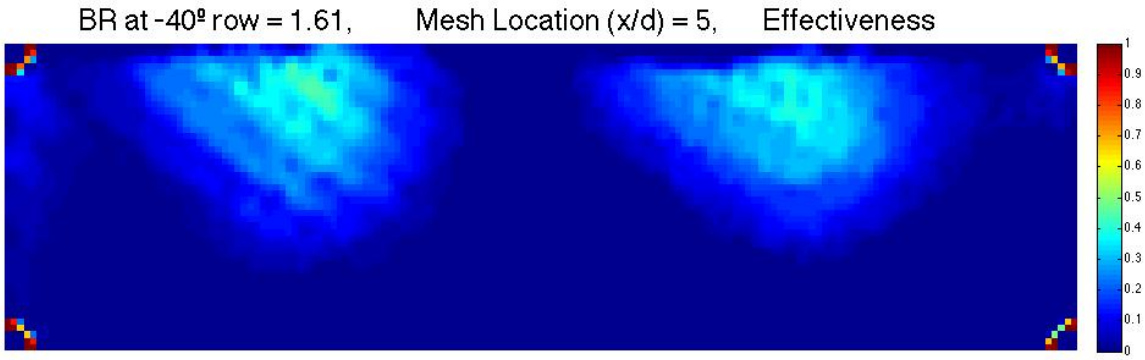

Figure 4-68 – Mesh at (x/d) = 5, BR_{40}=1.61

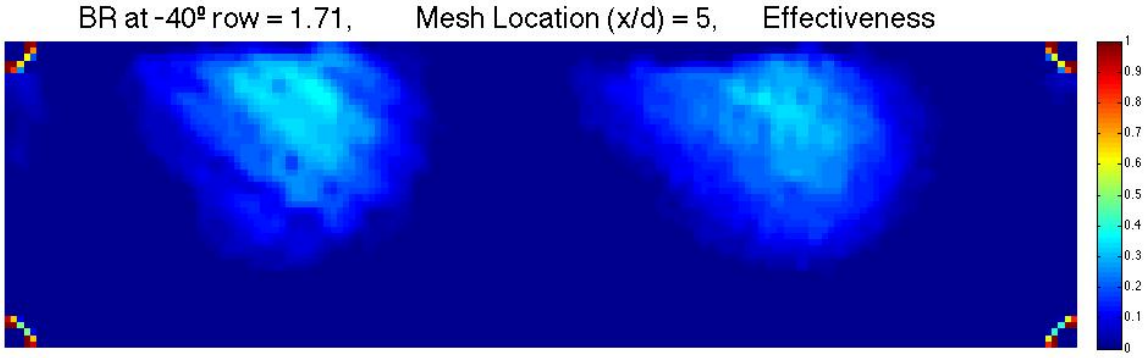

Figure 4-69 – Mesh at (x/d) = 5, BR_{40}=1.71

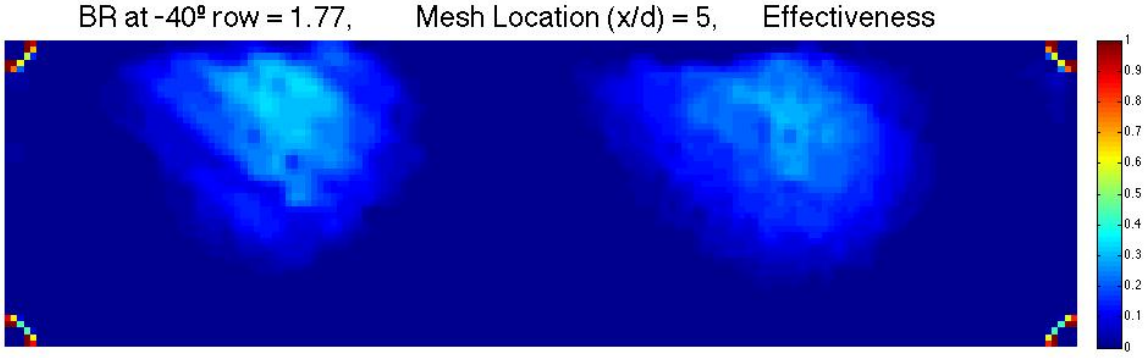

Figure 4-70 – Mesh at (x/d) = 5, BR_{40}=1.77

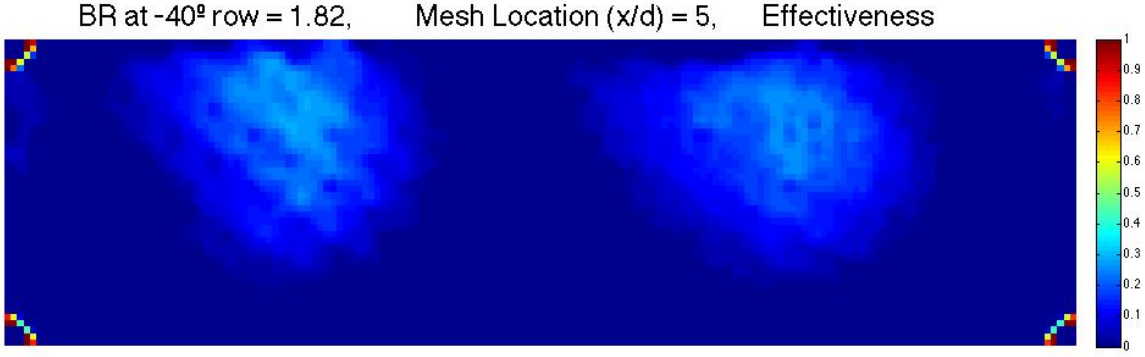

Figure 4-71 – Mesh at (x/d) = 5, BR_{40}=1.82

4.5.6 Discussion of the Mesh Images at x/d = 5

From figures 4-58 – 4-71, it can be seen that with increasing BR, the coolant jets tend to lift-off higher above the cylinder surface. As the jets lift-off more - they tend to diffuse more into the mainstream, which leads to reduced core CGE values at higher BR.

At BR values 1.01-1.05 (figures 4-58 – 4-59) the maximum CGE that can be observed on the nylon mesh near the cylinder surface is in the region of 30%. At these BR values the jet remains largely attached to the cylinder surface. Hence the visible 30% CGE is observed at around 2mm above the cylinder wall and is not a representative of the jet core values.

The CAWE at low BR - when the jet remains attached to the cylinder wall are approximately 60% at x/d = 5.

At BR values 1.29-1.44 (figures 4-64 – 4-66), core CGE of around 60% can be observed on the mesh. The coolant jet core gradually moves vertically away from the image edge (cylinder wall) and laterally to one side of the cylinder with increasing BR.

By analysis of the surface images, this hot core region is observed to detach from the cylinder surface at approximately BR = 1.23 (figure 4-7), as CAWE is around 50% at this BR value and x/d location. From the mesh images it can be seen that although the 60% core CGE is visible on the mesh, the CGE observed on the image edge closest to the cylinder surface is also in the region of 50%.

Increasing BR further to 1.71-1.82 (figures 4-69 – 4-71) results in core CGE values gradually declining down to 30% as the jet increasingly diffuses. CGE values observed on the mesh nearest to the cylinder wall are in the region of 20-30%. This is reasonably close to CAWE readings of 25-35% observed on the cylinder surface images (figures 4-13 – 4-15).

4.6 Comparison of Nylon Mesh Images

4.6.1 Comparison of Positive x/d Locations (1, 3, and 5)

The following section describes and compares how the coolant jet cross-section varies on a nylon mesh across the positive x/d locations (1, 3, and 5). Significant similarities can be observed for the three mesh locations:

- Increasing the Blowing Ratio results in increased jet lift-off
- The jets move both vertically and laterally away from the ejection holes with increasing BR values
- At low BR values (approximately 1.01 – 1.08) only the cooler part of the jet cross-section is visible on the mesh, as the central hot core with maximum CGE remains attached to the cylinder surface
- At mid-tested BR values (approximately 1.13 – 1.61) the hot core lifts off the cylinder surface sufficiently to be visible on the nylon mesh
- Increasing BR value further (approximately 1.71 – 1.82) increases the lift-off more, which leads to greater mixing with the mainstream flow and associated diffusion of the coolant jets

Diffusion is evident by the growth of their cross-sectional area and their boundaries becoming closer to each other with increasing BR. A similar effect is observed (for each BR value) with increasing x/d (displacement of the mesh further downstream of the ejection holes). The jet cross-sectional area increases and changes in geometry due to increased mixing with the mainstream. While these observations are generally expected, the consistency in flow pattern observations demonstrates the IRT's ability to visualise flow.

Table 2 illustrates how the maximum jet core CGE value that can be observed on the nylon mesh, changes with BR value for different x/d locations.

	Maximum observed core CGE values (%)				
Mesh x/d	5	3	1	-1	
BR40					BR20
1.01	30	40	50	X	X
1.05	35	50	55	35	1.04
1.08	40	55	60	X	X
1.13	50	60	65	45	1.15
1.17	55	60	70	X	X
1.23	55	65	70	55	1.23
1.29	60	70	70	X	X
1.37	60	70	70	65	1.39
1.44	55	70	70	65	1.48
1.53	50	60	70	X	X
1.61	45	60	65	65	1.64
1.71	35	60	60	X	X
1.77	30	55	55	65	1.78
1.82	25	50	55	X	X
X	X	X	X	65	1.98
X	X	X	X	65	2.12
X	X	X	X	60	2.32
X	X	X	X	60	2.49
X	X	X	X	55	2.7
X	X	X	X	55	2.83
X	X	X	X	55	2.92

Table 2 - A table of the maximum observed core calculated gas effectiveness values on a nylon mesh at different x/d locations

It can be seen that the maximum observed core CGE values fall with increasing x/d number. That is to say that the coolant jet diffuses with circumferential displacement from the coolant ejection hole. This has been expected, as stated previously. The fact that IR images can display this effect positively shows Infrared imaging as an effective tool for flow visualisation.

4.6.2 Comparison of Positive x/d Locations with x/d = -1

The upstream coolant jets (from the $20°$ hole row) blend into the downstream jets (from the $40°$ hole row). Images taken on the nylon mesh at positive x/d locations (1,3, and 5) therefore represent flow structures, which have higher CGE values and different shapes than if no upstream coolant jets were present.

In addition to this, cross flow at $\phi = 20°$ from SL of the cylinder model interacts with ejecting coolant at a different angle from interaction at $\phi = 40°$. The trajectory and cross-section of the coolant jets ejected from the two circumferential locations are expected to differ as a result. As the coolant jet interacts with mainstream at a sharper angle at $\phi = 20°$, it is expected to have a smaller tendency to lift-off than coolant at $\phi = 40°$ at the same BR value.

Figures 4-22, 4-42, and 4-56 show mesh images at approximately equal BR values (1.78-1.77) for (x/d) locations -1, 1, and 3 respectively (2d, 1d, and 3d separation from ejection hole trailing edge respectively). Since BR is nearly constant, displacement of the mesh circumferentially downstream is expected to govern the extent of lift-off. Mesh at (x/d=3) does show greater lift-off than the mesh at (x/d=1), however contrary to expectations lift-off is the smallest at 2d from ejection hole (x/d = -1). This effect can be attributed to the difference described above and is visualised by the IRT technique for other BR values.

The average CGE values at x/d = 1 (1d downstream of $\phi = 40°$), are greater than at x/d = -1 (2d downstream of $\phi = 20°$), which are greater than at x/d = 3 (3d downstream of $\phi = 40°$). IRT technique shows that average CGE values fall with increasing distance from an ejection hole, which is expected due to increasing mixing with mainstream flow (and subsequent jet diffusion).

Across all x/d locations - increasing BR results in increased jet momentum. As the ejection hole is cut at a compound angle, increasing BR causes increased vertical and lateral momentum, which results in vertical lift-off and lateral shift across the mesh.

Peak CGE values are visible on the mesh when the jet core begins to separate from cylinder surface (mid-tested BR values), further increasing BR results in jet diffusion, causing this peak value to fall and the jet to expand.

All imprints at high BR exhibit asymmetrical jet cross-sections. At x/d = -1 this is attributed to the formation of evident kidney vortices. These vortices cause the jet to lift asymmetrically (shift both vertically and laterally) and rotate with increasing blowing ratio. Asymmetry in jets at positive x/d locations can be attributed both to mixing of a coolant jet (from $40°$ hole) with an upstream jet (from $20°$ hole), as well as formation of kidney vortices.

The change in jet cross-section geometry with increasing x/d location can be attributed to rotation influenced by kidney vortices, as well as diffusion due to mixing with the mainstream flow.

The fact that these flow patterns can be positively identified and visualised with the aid of Infrared Thermography demonstrates its potential in turbine cooling visualisation applications.

4.7 Comparison of Results with Previous Studies

As discussed in Chapter 2, several research groups have used flow visualisation techniques to study turbine blade film cooling effectiveness on and above a solid surface. A comparison of the experimental results has therefore been made between this and earlier studies.

4.7.1 Comparison with a study by Sangan *et al.*

Sangan *et al.* have conducted flow-visualisation experiments related to turbine film cooling under very similar conditions [7]. Their cylindrical test-piece was also a scaled replica of that used by Reiss and Bölcs, who based the model on a Rolls-Royce turbine blade [20]. The same Reynolds number $\sim 1.5 \times 10^5$ (based on the cylinder diameter and similar to the engine-representative conditions) was reported. The coolant temperature has been heated to an elevated level between 30°C and 60°C [7]. TLC has been used to obtain coolant plume temperature distributions on two different perpendicular mesh types, while visualisation of cylinder surface temperature distribution plots have not been attempted. The coolant-to-mainstream momentum-flux ratio (*MFR*) was varied over a range stated to be typical for a turbine blade or nozzle guide vane leading edge (1.4, 2.9, and 7.3) [7]. The MFR values can be approximated by Blowing Ratios of 1.18, 1.70, and 2.70 respectively (conversion detailed in section 2.3.4). Mesh images were taken with a high-resolution CCD camera, positioned upstream and to the side of the mesh (not perpendicular to its surface).

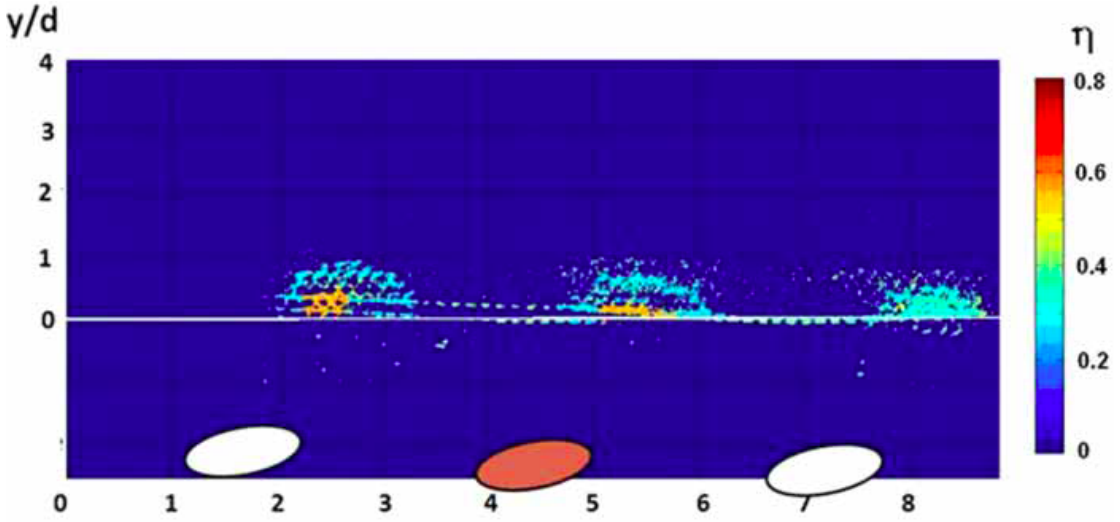

Figure 4-72 – Sangan *et al.* – Data processing difficulties

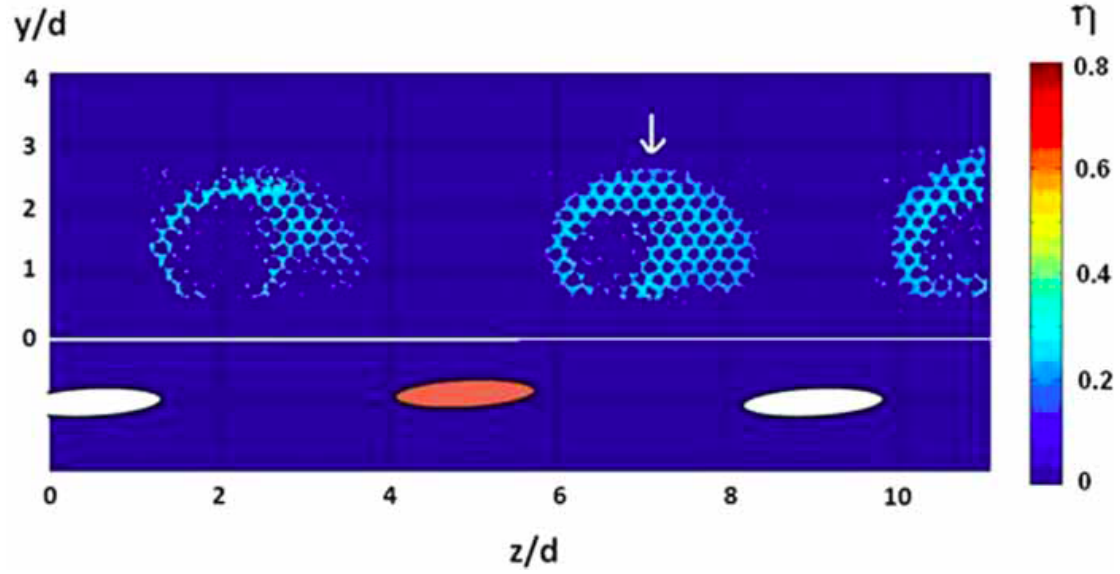

Figure 4-73 – Sangan *et al.* – Incomplete contours

Difficulties arising in processing of images (figure 4-72), as well as coolant contours that appear to be incomplete (figure 4-73) have been reported [7]. The former was attributed to activation of a 30°C crystal beyond its clearing point, while the coolant temperature was not high enough to activate the 40°C crystal. This highlights the immediate advantage of IRT technique over the TLC, as the IR camera is able to visualise a much larger temperature range, even with no heating present. However the images made with a CCD camera do show much better resolution than IR images, as the background can be easily distinguished from the mesh surface.

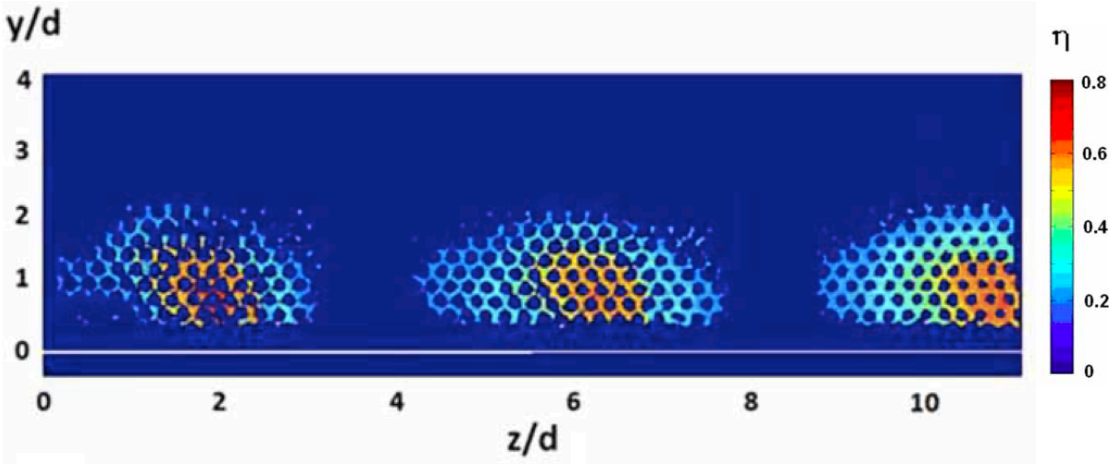

Figure 4-74 – Sangan *et al.* MFR = 2.90, mesh at x/d =1 aft 40° hole row

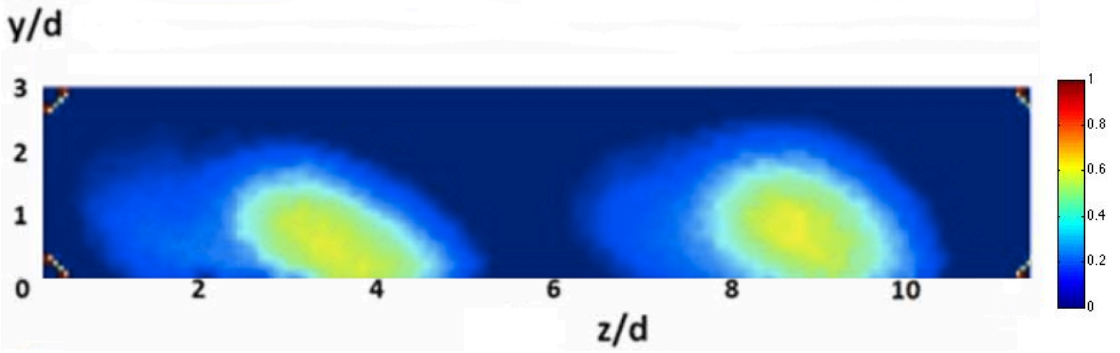

Figure 4-75 – MFR = 2.92, mesh CGE at x/d =1 aft 40° hole row

Figures 4-74 and 4-75 above represent a mesh at x/d=1 aft of the 40° hole row for a study by Sangan *et al.* and this thesis respectively (the image has been rotated to represent a like-for-like orientation). The MFR value is approximately equal in both cases (2.90 and 2.92 respectively) and the image imprint is taken approximately 2mm above the cylinder surface in both studies (marked as white solid line in figure 4-74, cropped out as discussed previously in figure 4-75). Coolant jet imprints of similar shapes, and height-to-width ratio can be observed on both images. Peak gas effectiveness values of approximately (0.6-0.7) and peak CGE values of 0.6 can be observed in figures 4-74 and 4-75 respectively. Better image resolution can be observed in figure 4-74, as the mesh can be clearly differentiated from the background. It is suggested that lower peak values of effectiveness seen in figure 4-75 are due to difficulties in image processing (background IRI readings being falsely taken for mesh IRI readings due to poor image resolution – hence lowering the average CGE distribution). The asymmetry of the jets observed in figures 4-74 and 4-75 has been attributed to the effect of kidney-shaped vortices.

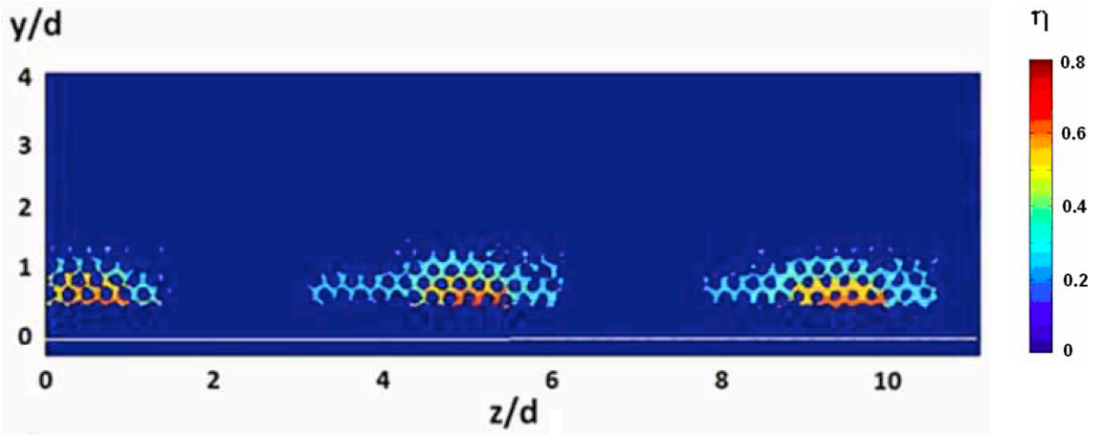

Figure 4-76 – Sangan *et al.* MFR = 1.40, mesh at x/d =1 aft 40° hole row

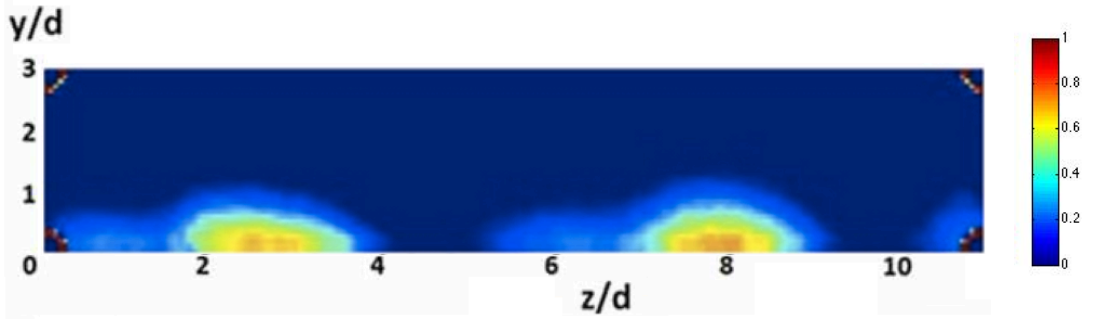

Figure 4-77 – MFR = 1.37, mesh GCE at x/d =1 aft 40° hole row

Similarly, figures 4-76 and 4-77 above represent a mesh at x/d=1 aft 40° hole row. The MFR values are close in the two cases (1.40 and 1.37 respectively). Contrary to images 4-74 and 4-75, the region of peak effectiveness has not separated from cylinder surface and is only partially seen on the mesh. The extent of mesh separation from the surface therefore influences the observed peak gas effectiveness values (the closer a mesh is to the surface – the greater gas effectiveness values of the attached jets can be observed). The mesh separation was estimated to be 2mm in both studies. Coolant jet imprints of similar shapes, height-to-width ratio, as well as approximately equal peak gas effectiveness and peak CGE values (0.7) can be observed in both figures. The jet structures captured in both studies appear to be in qualitative agreement, and to some extent illustrate similar quantitative effectiveness values. The mismatch in quantitative data has been attributed mainly to processing difficulties associated with poor image resolution of IR camera. Some advantages (complete jet imprints) and disadvantages (reduced image resolution) of IRT over TLC technique are also evident from this comparison.

4.7.2 Comparison with a study by Reiss and Bölcs

Reiss and Bölcs have conducted flow visualisation experiments on a TLC-covered cylinder model in hot mainstream. One of their experiments included visualisation of ejecting coolant from a cylinder with circular holes at Reynolds number 1.55×10^5 (based on cylinder diameter) [20]. As the model in this study was scaled on that used by Reiss and Bölcs, the surface images can be compared. An exact comparison is difficult, as "bulk Blowing Ratio (*G*)", and "bulk momentum-flux-ratio (I)", (which have been taken as averaged values over the entire showerhead) have been used in the study by Reiss and Bölcs. This is opposing to the local BR and local MFR (calculated separately for each coolant hole row) used in this study.

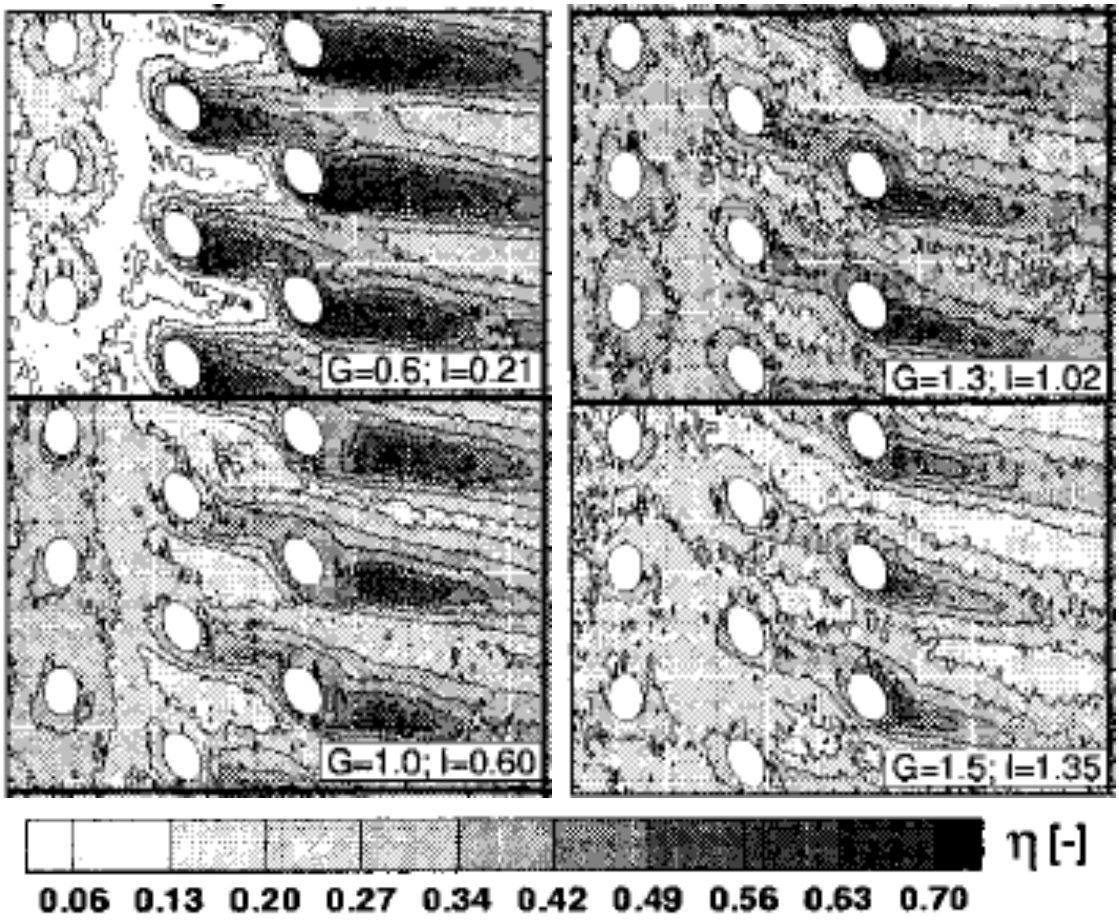

Figure 4-78 – Reiss and Bölcs – detailed film cooling effectiveness

Figure 4-78 demonstrates the experimental results of detailed film cooling effectiveness for cylindrical holes [20]. The “bulk BR” is seen to increase from 0.6 to 1.5 in the four presented images. While it is difficult to assess the local BR value (e.g. BR_{40}) on the images, they are stated to be engine-representative (i.e. are approximately in the region of 0.5-2.0 [21]).

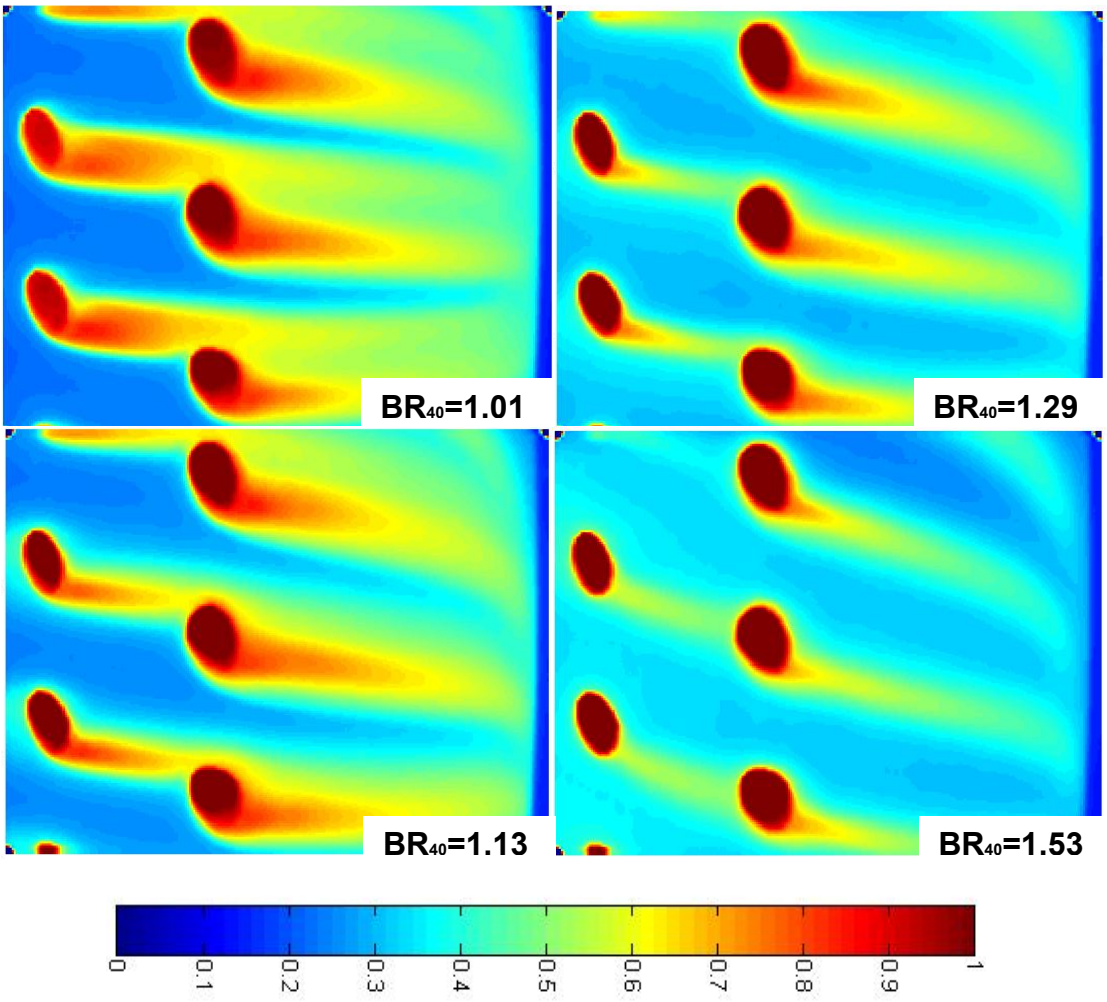

Figure 4-79 – CAWE distribution over cylinder surface

Figure 4-79 demonstrates four experimental results samples taken from this study, with BR_{40} ranging between 1.01 (minimum value) and 1.53 units. While the images in figure 4-79 do not represent “bulk BR” values as images in figure 4-78, it is still possible to make qualitative comparisons between them.

In particular it can be seen that increasing the BR value results in increased lateral shift of coolant jets across the surface, as well as jet lift-off (effectiveness values decrease on the surface) in both studies. It can be seen both on figures 4-78 and 4-79 that the coolant jet from the $20°$ hole row has lower effectiveness values than coolant jet from the $40°$ hole row in each of the separate images. This can be explained by the fact that the upstream jet blends with the downstream jet. The net effect of this is the increased cooling effectiveness values of the downstream jet. Qualitatively the coolant jets seem to behave similarly, which demonstrates the potential of IR thermography in turbine cooling flow visualisation.

Contours in figure 4-78 have been reported as instructive, and allowing qualitative interpretation, in terms of behaviour of individual jets, rather than quantitative analysis. They were therefore only used for qualitative comparison with this study.

4.7.3 Comparison with a study by Coat and Lock

Coat and Lock have conducted flow visualisation experiments on a TLC-covered flat plate with one row of hot coolant ejecting holes, as well as a perpendicular fine nylon TLC-covered mesh in cold mainstream. The Reynolds number of 3.6×10^4 (based on the hole diameter), and MFR between 3 and 12 has been reported (and stated to be typical of values representative of the leading edge of a turbine blade or vane) [19].

As temperature of the coolant varied only over a modest range $(30℃ - 60℃)$, the coolant-to-mainstream density ratio was assumed to be unity, and hence the representative BR values can be approximated as 1.87 and 3.46 respectively for the stated MFR values. Two cylindrical ejection hole geometries were assessed – stream-wise and cross-stream inclined (as opposing to cylindrical holes with a compound inclination angle in this study). The Reynolds number (based on the hole diameter) used in this study was 0.64×10^4 and differed significantly from that used by Coat and Lock.

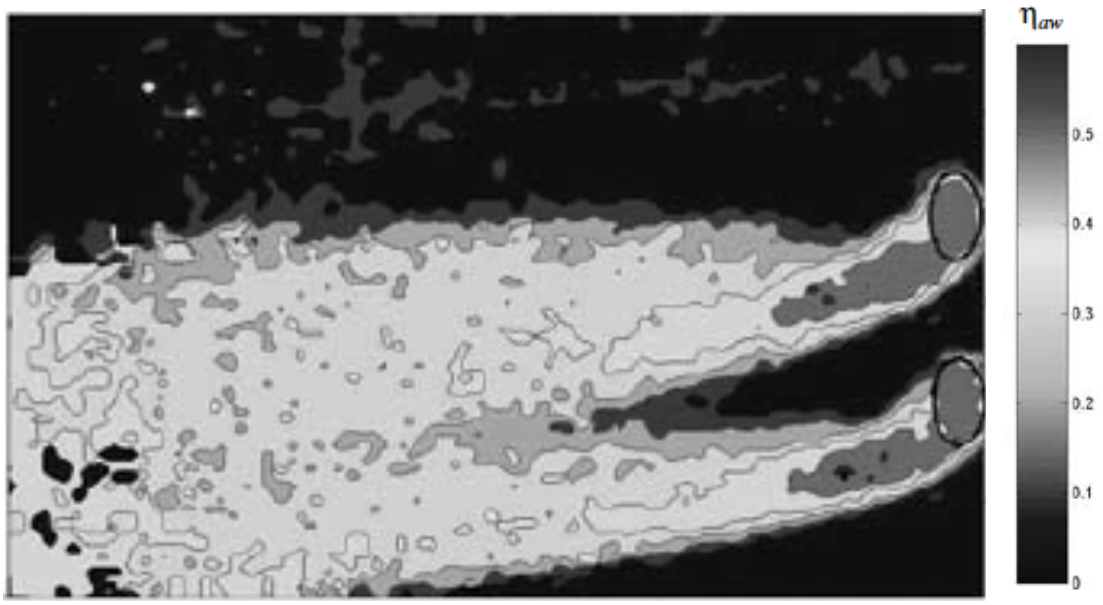

Figure 4-80 – Coat and Lock – cross-stream injection

Figure 4-80 demonstrates effectiveness contours on the surface downstream of injection for cross-stream cylindrical holes at MFR=3.5 (BR=1.87) [19].

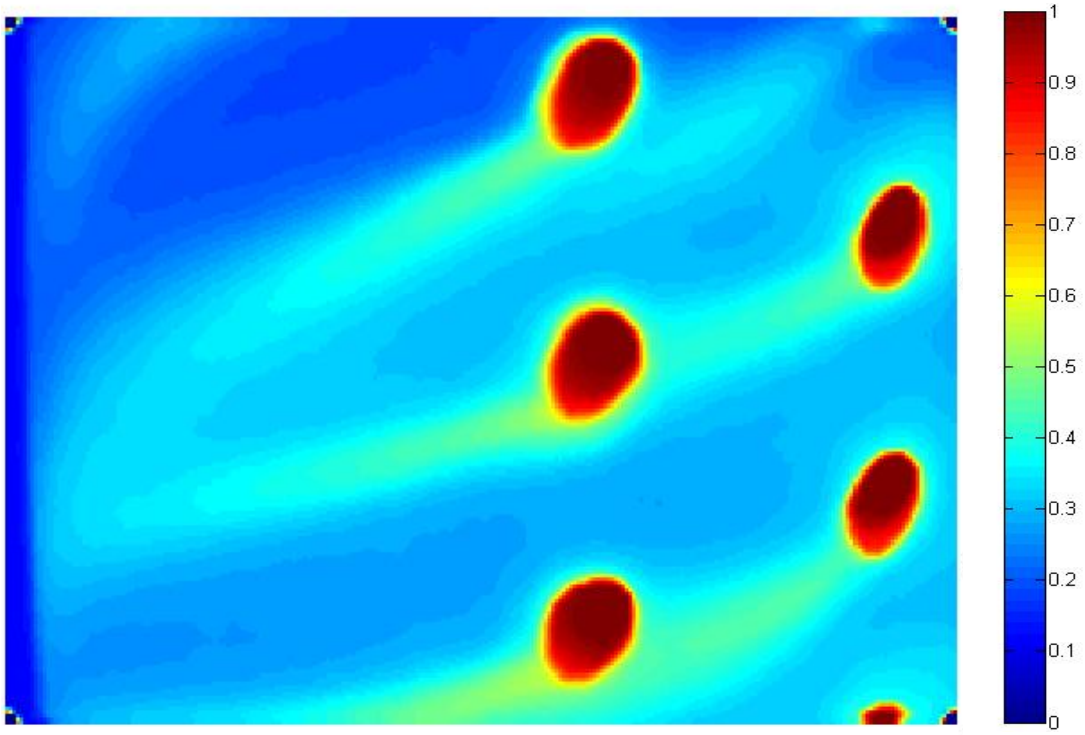

Figure 4-81 – Cylinder Surface CAWE at BR_{40}=1.82

MFR value in figure 4-80 approximately corresponds to a BR value of 1.87 and can be compared with the coolant jet from the $40°$ row at $BR_{40} = 1.82$ (figure 4-81). Lateral shift, encouraged by cross-stream and compound angle inclination can be observed respectively in both figures. The coolant jet is largely separated from the surfaces in both figures. This is represented by a short and narrow (2-3 hole diameters in length) region of approximately 50% effectiveness in both images (with steep temperature gradient on the sides of the coolant jet plumes). The effectiveness values fall to approximately 30-35% at around 5d away from ejection in both figures. At approximately 5d downstream from ejection in figure 4-80, the coolant plumes seem to begin to merge with each other, as the extent of their diffusion increases. A similar pattern can be observed in figure 4-81, where central and top plumes seem to begin to merge at approximately 5d downstream of ejection.

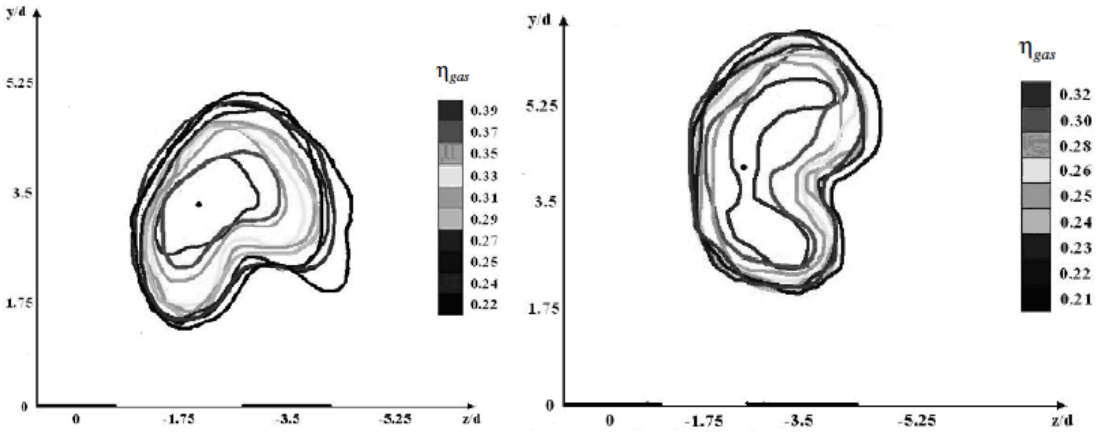

Figure 4-82 – Coat and Lock – cross-stream injection at MFR=11 for x/d =1 (left) and x/d=3 (right)

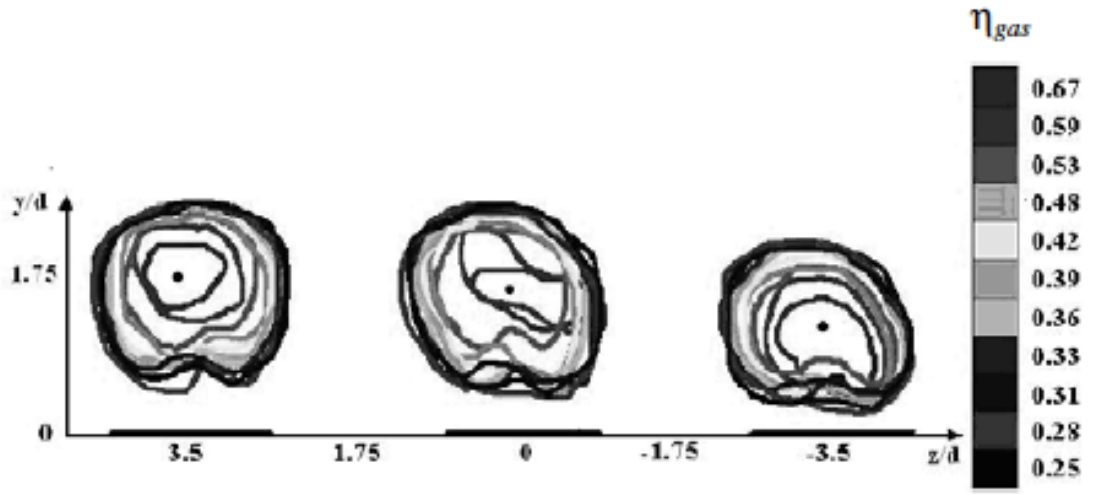

Figure 4-83 – Coat and Lock – stream-wise injection at MFR=11 for x/d =1

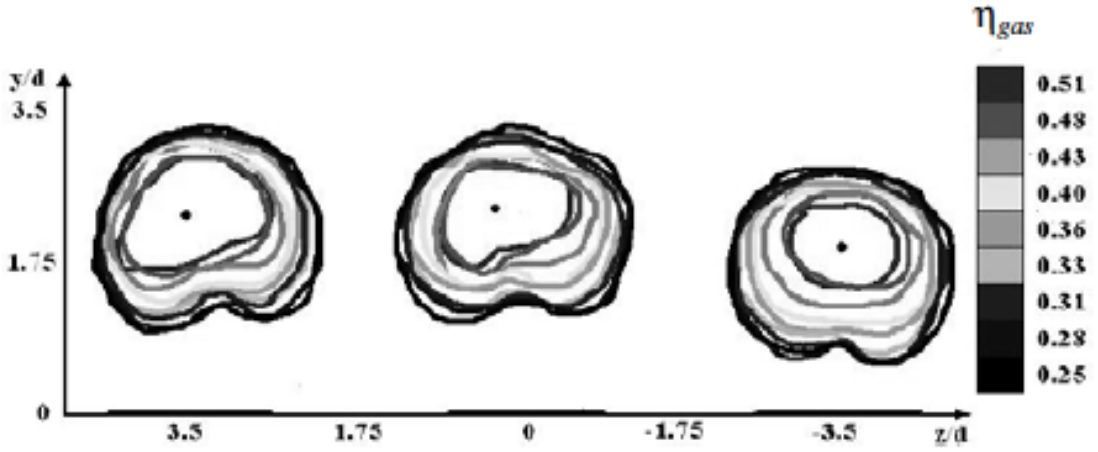

Figure 4-84 – Coat and Lock – stream-wise injection at MFR=11 for x/d =3

Figure 4-82 demonstrates gas effectiveness contours of the coolant jets ejected from cylindrical holes with cross-stream inclination at high MFR value of 11 (approximately BR=3.31), for mesh locations x/d=1 (left) and x/d=3 (right). The asymmetric jet has lifted off the surface and is seen to rotate with increasing distance downstream of ejection hole. The apparent lack of further lift-off as the jet travels from x/d=1 to x/d=3 has been attributed to the jet rotation (and hence the lifting force changing from vertical to horizontal direction).

Figures 4-82 – 4-84 demonstrate asymmetric coolant jet structure (attributed to effect of kidney vortices). Figures 4-83 – 4-84 illustrate gas effectiveness contours of the coolant jets ejected from cylindrical holes (at the same high MFR value of 11 – approximately BR=3.31), but with stream-wise inclination. Evident rotation of the jet cannot be observed as it travels from x/d=1 (figure 4-83) to x/d=3 (figure 4-84), however there is an increasing lift-off, which has been attributed to the lack of jet rotation that can be seen in figure 4-82. The kidney shapes are more noticeable for cross-stream injection (figure 4-82).

A mismatch between adiabatic effectiveness (at the wall) and gas effectiveness on the mesh (near the wall) has been reported by Coat and Lock. This has been attributed to the gap between the wall and the mesh (and associated limit of how close mesh measurements could be taken near the wall). The mismatch has also been observed and discussed in this study in earlier sections and partially attributed to the same effect.

Since the coolant holes in this study are orientated both at a vertical and a lateral angle to the mainstream, the mesh imprint images would be expected to qualitatively resemble shapes which are a compromise between those in figure 4-82 (cross-stream) and figures 4-83 – 4-84 (stream-wise). Quantitatively the gas effectiveness values are expected to differ, as the studies have been conducted at different Reynolds numbers.

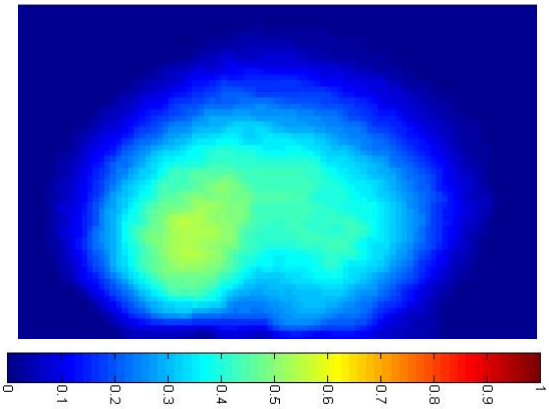

Figure 4-85 – CGE at x/d=-1, BR_{20}=2.92

While the range of MFR and hence Blowing Ratios tested in this study was not as high as that used by Coat and Lock, distinct kidney shaped vortices can be observed in figure 4-85 at $BR_{20} = 2.92\ (MFR \approx 8.53)$. This image represents a jet from a singular $20°$ hole and was taken at x/d=-1 (which is 2d downstream of ejection), compared to the jet from a singular hole seen in figure 4-82 (left) for an identical mesh at 1d downstream of ejection and MFR = 11. The images seem to share qualitative similarities: shape, lift-off, rotation (the right edge of the vortex is lifting further away from the surface than the left one), vortex structure (effectiveness distribution is not symmetrical with peak values skewed to the left side of the vortex – closest to the surface).

The extent of lift-off and rotation, as observed in figure 4-85 is closer to that seen for stream-wise ejection in figures 4-83 – 4-84. The shape and extent of asymmetry is close both to images of stream-wise and cross-stream ejection. However, this was expected and mentioned previously as the coolant is ejected at compound angles in this study.

4.8 Flow Separation Visualisation Experiments

Experiments beyond the original scope have been conducted during this study. The ability of IRT to identify the exact location of flow separation from the cylinder model surface in mainstream flow was assessed. For this purpose a hot air gun was fixed in a stable position levelled with cylinder centreline and facing the trailing edge ($\phi = 180°$ from SL). The IR camera was fixed above the cylinder so that good resolution images could be obtained without interfering with the flow over the cylinder surface. Cold laminar mainstream flow over the circular cylinder was generated by the wind tunnel (coolant flow was not switched-on). The hot air gun generated hot air flow over the cylinder surface in the opposite direction to the mainstream flow.

For Reynolds number in the order of 10^5, the separation point (*SP*) of the laminar boundary layer (*BL*) is expected at $\phi \approx 80^\circ$. For a turbulent BL $(3\times10^5 > \mathrm{Re} > 3\times10^6)$, the SP moves to $\phi \approx 120^\circ$ (as turbulence delays separation) [74]. In this particular experiment the Reynolds number (based on the cylinder diameter) was approximately 1.5×10^5. As the cylinder was positioned in laminar flow, the SP was expected to be at approximately $\phi = 80°$ from the SL.

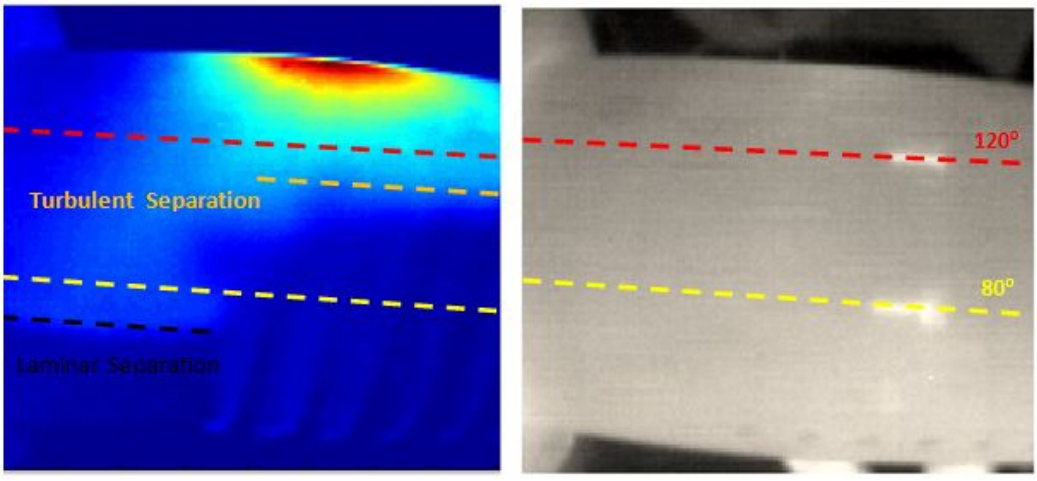

Figure 4-86 – IR image of opposing airflows (left), IR image with no flow over the cylinder (right)

Figure 4-86 illustrates the plan view of the cylinder with the two opposing airflows over its surface (left), and no flow over the cylinder when the wind tunnel and air gun are powered-off (right). Two pieces of pre-heated wire have been taped onto the cylinder at $\phi = 80°$ and $\phi = 120°$ from the cylinder SL and can be seen in figure 4-86 (right). An IRI image of the pre-heated wires on the cold cylinder surface was taken to identify the circumferential positions on the images (marked with yellow and red broken lines respectively). The wires were then removed before the wind tunnel airflow was powered-on.

Figure 4-86 (left) shows red-yellow-green region on the cylinder where its surface is heated by the dominating hot air flow. The dark blue colour represents the cold cylinder region where mainstream flow remains attached to the surface. The light blue colour represents the warm cylinder region where mainstream flow has separated from the surface, which is being heated by the opposing hot air. A frontline, similar to that reported by Desideri *et al.* [71] can be seen between the dark-blue and light-blue region, which represents the line at which mainstream flow detaches from the cylinder surface. It can be seen that where the mainstream passes over the smooth side of the cylinder (with no ejection holes), this frontline is at approximately $\phi = 70°$ from SL. This is consistent with experimental results demonstrated in figure 4-1. Likewise where mainstream passes over the surface with ejection holes, this frontline is at approximately $\phi = 110°$ from SL. This is because coolant ejection holes act as a step, which trip-up the laminar flow, causing it to become turbulent. Essentially therefore two types of flow can be seen over cylinder surface in this image (laminar and turbulent).

Laminar flow separates significantly sooner than turbulent flow (turbulence delays separation), which is consistent with expectations described earlier in this section. The images illustrate that IRT can be exploited as a non-intrusive visualisation tool not only to analyse temperature distributions, but also to study and analyse flow separation locations across bodies of various geometries. This technique is therefore applicable to wing design, or aerodynamically optimised vehicle body shape design (to reduce drag).

4.9 Infrared Thermography Limitations & Recommendations

The following section discusses the limitations of Infrared Thermography in gas turbine cooling visualisation that have been identified in this study.

4.9.1 Effect of Experimental Uncertainties

The accuracy of thermal distribution images depends on careful calibration of IR camera for the specific test surface, as well as image noise (background noise of the camera – NETD). As it has been previously discussed, in order to calibrate the infrared camera, it is necessary to observe how:

i) Perceived IRI changes with internal camera temperature (acquired by the camera software to an accuracy of $\pm 0.1℃$).

ii) Perceived IRI changes with temperature of the visualisaed body (recorded by a thermocouple to an accuracy of $\pm 0.1℃$).

Camera case temperature is recorded by the camera software and is limited to this accuracy of measurement (for this particular camera model). NETD of $\pm 0.085℃$ for the camera further increases the measurement uncertainty. Temperature of the visualised body temperature can be measured to a higher accuracy of $\pm 0.01℃$, resulting in more accurate calibration and thermal images. This could be achieved with a more sensitive thermocouple. Same accuracy improvement could be implemented for mainstream and coolant thermocouple temperature measurements in order to reduce the uncertainty in conversion of thermal distributions into CAWE and CGE images.

The estimated overall experimental uncertainty in determining the calculated adiabatic wall effectiveness is $\pm 4.5\%$, and the calculated gas effectiveness is $\pm 9\%$. Which is less accurate than the lowest reported uncertainty in film-cooling effectiveness calculation in previous studies ($\pm 7\%$) [67].

As the prime objective of this study is an assessment of applications and limitations of IRT, rather than quantitative assessment in turbine blade cooling, this accuracy is deemed acceptable however.

4.9.2 Effect of Mesh Temperature Measurement

It is more difficult to calibrate the camera over the nylon mesh, than performing the same task for a copper block, as steadily raising the nylon mesh temperature is more challenging. In order to raise the mesh temperature a hot air gun was used in this study. The gun air outlet has structural features that result in flow turbulence even at the minimal power output and when the power output is held constant. The jet's centre therefore moves around the mesh, causing fluctuations in measured temperature by the stationary thermocouple.

A more reliable method of calibrating the camera on the mesh for a future study would be to position the mesh in a sealed transparent container. The temperature within the container could be regulated to a constant value for a sufficiently long period of time to allow the nylon mesh temperature to achieve thermal equilibrium with its environment. The mesh temperature (air temperature in the container) would then be measured using thermocouples).

The suggested calibration method could also use a sheet of nylon (rather than a mesh) to take perceived IRI images over a larger surface area than thin mesh fibres. This would eliminate the chance of background IRI (which can be seen through a mesh) being falsely taken for nylon IRI values. In addition the IRI could be observed over a large area and averaged to minimise uncertainties (similarly to the current block calibration method).

The camera could similarly be calibrated on a block of black-painted Rohacell (cylinder surface material), rather than black-painted copper block. This would potentially increase calibration accuracy, as Rohacell and copper have different emissivities.

4.9.3 Effects of Background during Mesh Visualisation

During this study it was found that the temperature values of the mesh, as observed by the camera, could at times be lower than anticipated. This could be due to the average IRI value of the mesh being lowered by IRI value of the background. Initially it was considered that numerical filters (while filtering noise and improving spatial resolution) can reduce mesh IRI by averaging it with adjacent image pixels, representative of the background.

A data segmentation technique was applied to the images in an attempt to filter-out the pixels representative of the background and only leave the pixels representative of the mesh in an image. This process would have allowed calculation of IRI value over a larger area of the mesh around the thermocouple during calibration. In addition it would potentially have reduced the above-mentioned effect during processing of experimental data. However due to poor image resolution this technique was found to be ineffective. The fine nylon mesh appears very pixelated with a width of only one pixel. This means that this image pixel could in fact be representative of a portion of the mesh fibre and a portion of the background. The background inherently lowers the displayed value of IRI of the mesh as a result.

In order to improve experimental accuracy in a potential future study, the possibility of acquiring images closer to the mesh surface should be assessed, especially if the camera was not subjected to a hot jet flow over its surface (being in a sealed environment, which would allow it being placed closer to a test surface without affecting the case temperature, or experimental results). A series of external lenses and/or magnification mirrors could be used to observe a body with increased resolution. Alternatively a different camera with a higher resolution could potentially be selected for future studies in order to produce clearer mesh images. A mesh with thicker fibres would increase the mesh visibility with the current camera, but this is not advised, as thicker fibres would have a greater influence on the flow through the mesh and may therefore affect experimental results.

4.9.4 Effect of Camera Case Temperature Oscillation

It has been discussed that the camera case temperature tends to oscillate during operation, if the camera works in an uncooled environment. This effect can be limited in the wind tunnel, although it was not entirely eliminated for the operational mainstream flow velocities used during this experimentation.

In order to achieve best resolution images of the observed bodies (particularly important for observation of the fine nylon mesh – to differentiate the mesh from the background) – it is necessary to position the camera closer to the object, which in case of downstream position from the mesh would result in hot air flow over the camera thus increasing its case temperature further.

It is therefore suggested that in order to limit the camera case temperature oscillation (and hence improve the accuracy of calibration codes) – the camera should be cooled. In order to be able to position it closer to a hot source without increasing the case temperature – the camera could also be shielded from the environment.

Protective casings for infrared cameras with special lenses for optical access are commercially available for use in environments where the cameras may be exposed to extreme temperatures. However these casings do not have integrated cooling systems to regulate camera case temperature. A camera container may however be designed for the camera to be cooled within inside it by a circulation of gas set to a necessarily low temperature, while shielding it from the outer environment at the same time.

4.9.5 Effect of Indirect View of the Camera

As has been described in the previous sections, the camera (both during calibration and data acquisition stages), as well as nylon (during calibration), or Rohacell may be placed into transparent containers for increased experimental accuracy. As such the IR camera would be observing a test

body from an indirect view (described in detail in chapter 2) through the container wall. The camera would be operated from within the same container both during calibration and data acquisition experiments.

If the mesh is also isolated in a container during calibration – then the camera has to observe the experimental set-up through a small additional lens of the same transparent material to ensure identical conditions of an indirect view during the experimental data acquisition. This would be technically feasible, but as it has been described in chapter 2 in detail, there is a limited range of expensive transparent materials that allow the infrared camera to visualise hot bodies through them. The entire container does not have to be manufactured of this same material (as only a small window would be required to allow transmittance of IR radiation to the camera).

4.9.6 Effect of Processing Code Accuracy

It has been shown that experimentation with different mathematical approximation models has yielded different levels of accuracy of raw data processing. Of the models investigated, a second order polynomial has provided the greatest accuracy, but higher order polynomials could be tested in future studies and may yield improved results.

Barrel distortion, caused by magnification tendency of camera lens can be observed in the experimental results. A filter could be integrated into the data processing code to move the distorted image coordinates in place of ideal image coordinates in a future study.

A future study could also implement data processing technique used by Cardonne *et al.* [62] (described in chapter 2). A 2D image array of the cylinder model could be plotted on a representative 3D cylinder mesh, calculating the viewing angle variation and making an adjustment for respective change in directional emissivity of each mesh segment.

4.10 Applications of Infrared Thermography

Having performed analysis of experimental results, it can be concluded that IRT is an effective flow visualisation tool. It can be applied to the study of film cooling effectiveness by analysis of turbine component models such as that used in this study. Limitations of this technique have been discussed and potential improvements have been suggested. Upon their completion, it should be possible to achieve more accurate camera calibration and effectiveness images. This would provide grounds for more reliable quantitative analysis using IRT. The current experimental set-up however was successful at identifying some qualitative features of turbine blade model cooling.

4.10.1 Comparison of Film-Cooling Configurations

The experimental technique described in this work could be used to investigate optimum BR values for turbine blades of different designs. It is possible to extend this study and investigate optimum film-cooling features for other turbine components (e.g. NGVs, stator and rotor discs). This could include comparing:

- Different coolant ejection hole geometries
- Different angles of inclination and orientation of the coolant channels
- Different ejection hole arrangements (e.g. circumferential separation between ejection hole rows, or spanwise separation between ejection holes in a specific row.
- Different turbine blade geometries

4.10.2 Heat Transfer Measurements

The experimental technique used in this study could potentially be extended to acquiring Heat Transfer measurements through a test body. Thermochromic Liquid crystals are often used to obtain thermal distribution

plots and calculate Heat Transfer coefficients through models of turbine components (e.g. turbine discs and blades). TLC technique currently provides readings of a greater accuracy ($\pm 0.1℃$) than IRT ($\pm 1.0℃$ – estimated for a copper block), but IRT is easier to set-up and simpler (as well as more economical) to operate over a prolonged period of time. IRT can also provide temperature distribution maps over a larger area and a higher temperature range (even when no heating occurs, which is difficult with TLC). After implementing the suggested improvements to accuracy of the current IRT technique, it may appear as a more appealing option, but further experimentation is required to prove this.

4.10.3 Jet Structure Visualisation

Visualisation of coolant jet imprints on a fine nylon mesh has demonstrated the ability of IR cameras to analyse jet structure. Feautures such as kidney vortices, the extent of lift-off, lateral shift and diffusion have been visualised at various circumferential locations around the cylinder. Calculated Gas Effectiveness values have been obtained using the current experimental technique. IRT could therefore aid in preforming a 3D analysis of film-coolant interaction with the mainstream flow after ejection.

4.10.4 Flow Separation Visualisation

The IRT has been used as a visualisation tool for determining locations of flow separation over a test surface. This process (described in section 4.8) can be described as non-intrusive, as a mesh was not used for surface visualisation. The technique could potentially be extended to various models, and find applications outside of gas turbine cooling visualisation (e.g. aircraft wing or vehicle body shape design).

4.11 Conclusions on Experimental Findings

Analysis of the experimental results has illustrated the ability of IRT to visualise film coolant distributions both over the turbine blade leading edge model and above its surface. The IR camera has been used to visualise coolant trajectories, cylinder surface coverage, as well as CAWE values for a range of Blowing Ratios. Consistent qualitative data, as well as Calculated Gas Effectiveness and Calculated Adiabatic Wall Effectiveness values have been observed between the mesh and cylinder surface images respectively. This illustrates the application of IRT in qualitative assessment of turbine cooling effectiveness and identifies the potential (subject to reducing experimental uncertainty) for quantitative analysis in the future. Various flow features, such as formation of kidney vortices and flow separation locations have been analysed in this study and demonstrate further application of IRT in flow visualisation both on and above a test surface. Work conducted outside the original scope has also illustrated the application of IRT in visualisation of flow separation locations on surfaces of various shapes (e.g. turbine blade, wing or vehicle body models).

The main limitations of the technique have been identified as the difficulty in control of internal camera temperature (leading to reduced camera calibration accuracy), image resolution (leading to reduced measurement accuracy), as well as the necessity to calibrate the camera separately for every different test surface material (due to the difference in their emissivity values). Potential solutions that can reduce effects of limitations have been discussed in this chapter.

4.11.1 Optimum Turbine Blade Model Cooling Parameters

The results obtained indicate highest observed $CAWE$ values at BR_{40} of approximately 1.05 – 1.08. The most efficient film cooling method must produce high local surface cooling effectiveness, and lead to an even distribution of cooling effectiveness across the turbine blade surface. Therefore the coolant plumes should blend into a single coolant film and stay attached to the entire surface as much as possible, ensuring highest HT rates.

Analysis of the coolant jet structure both on and above the turbine blade model leads to the conclusion that the coolant jets remain attached to the cylinder surface for longest at the lowest tested blowing ratios (BR_{40} = 1.01). The plumes also seem to be the closest to blending together into a single shield of coolant at BR_{40} = 1.01. The optimum BR value for maximum surface coverage by the coolant may be below those tested within this project.

Increasing the quantity of air that is bled from the compressor reduces the pressure and quantity of air that reaches combustion chamber (and hence limits the power output of the working cycle). Coolant air that mixes with hot mainstream in the turbine stages also reduces the engine thrust and efficiency. Thus the minimum amount of coolant should be used, which would be achieved at the lowest acceptable BR (subject to a compromise between the factors stated in this section). It is therefore suggested that lower BR values should be analysed in further potential studies, where identifying the optimum BR value is an important objective. The objective of this study however has been in assessing the feasibility of IRT in turbine blade film cooling visualisation and it can be concluded that this technique can be used for the purposes of identification of optimum turbine blade model cooling parameters.

5 Conclusions and Recommendations

The following chapter draws a final conclusion to the author's work and summarises the suitability, as well as limitations of IRT as a flow visualisation tool for gas turbine cooling studies. Potential improvements and recommendations for further research are also summarised in this chapter.

5.1 A Review of Initial Objectives

The initial objectives of conducting the experimental study of turbine blade model film cooling effectiveness using IRT, have been identified as:

i) Assessing the limitations and the suitability of IRT in turbine cooling visualisation, particularly in comparison with other traditionally used thermal imaging methods, such as Thermochromic Liquid Crystals
ii) Assessing the limitations of IRT in qualitative and quantitative assessment of cooling effectiveness
iii) Identifying the applications of this technique

At this stage it can be concluded that these objectives have been fulfilled.

5.2 Experimental Results

Experimental results show that Infrared Imaging is capable of producing calculated effectiveness distribution plots for analysis of film cooling both on and above the turbine blade model surface:

i) A three-dimensional model of coolant jet interaction with mainstream after ejection can therefore be built.

ii) Surface images can be used to observe qualitative flow patterns (e.g. coolant geometry, trajectory and surface coverage).

iii) Jet structure (e.g. formation of Kidney-shaped vortices), as well as the extent of diffusion, lift-off and lateral shift can be assessed from nylon mesh images.

iv) Over the tested range of BR, it can be generally concluded that increasing BR value results in cooling jet separation from the cylinder surface and is detrimental to film-cooling effectiveness.

v) Peak values of Calculated Adiabatic Wall Effectiveness were observed for BR_{40} values in the region of 1.05 – 1.08.

vi) The coolant plumes appear to be closest to forming a single shield of coolant at the lowest tested BR_{40}=1.01, suggesting that optimum BR for maximum coolant coverage may be below the tested range.

The results show qualitative and quantitative (CAWE and CGE) similarities between cylinder surface and nylon mesh images. This indicates that IR camera produces coherent results. Observed mismatch in data may arise from uncertainties in calibration and experimentation process.

5.3 Recommendations

The following section summarises improvements that could potentially be implemented into the experimental technique to increase its accuracy.

i) Acquiring case temperatures to an increased accuracy of $\pm 0.01℃$ (this may be achieved by changing the camera to an alternative model).

ii) Measuring test body, mainstream and coolant temperatures to an increased accuracy of $\pm 0.01℃$ with more sensitive thermocouples.

iii) Positioning the nylon for calibration into a sealed container with a Zinc Selenide (ZnSe) screen and controllable internal temperature.

iv) This technique could be extended to calibrate the camera on a painted Rohacell (cylinder surface material), rather than painted Copper block (to account for the difference in thermal emissivity).

v) The camera could be enclosed in a separate case of controllable internal temperature with ZnSe lens and cooled with circulating gas to maintain a constant case temperature.

vi) Enclosing the camera would also permit it to be located closer to the mesh for acquisition of mesh images with better resolution.

vii) A magnification lens and/or magnification mirrors could be considered as an alternative method of improving image resolution.

viii) A camera with higher image resolution (and/or internal cooling) may be considered for a further study to provide better image data.

ix) Higher orders of polynomial could be used for construction of the raw data processing algorithm, which may yield more accurate approximations of IRI image conversion into thermal distribution.

x) A pump capable of producing Blowing Ratios of smaller values should be used for further studies, as the BR for optimum cooling effectiveness may lie below those BR values tested in this study.

5.4 Final Conclusions

An experimental assessment of IRT applications and limitations in turbine cooling visualisation has been conducted. The technique proved to be

suitable for qualitative analysis of coolant jets on and above a turbine blade leading edge model.

In addition to the applications assessed in this study, the outlined experimental technique could be used in further studies to compare effects of various coolant ejection hole geometries; angles of inclination and orientation of the coolant channels; coolant ejection hole arrangements (such as circumferential and spanwise separation between the holes). The study could be extended to assess different turbine blade geometries and other turbine components (NGVs, stator and rotor disc) cooling effectiveness. The technique could therefore be useful in gas turbine research and development.

Quantitative thermal distribution maps can be plotted using this technique, but further improvement of accuracy is advised before this data could be successfully used for quantitative analysis, such as accurate film cooling effectiveness distribution plots and Heat Transfer measurements. Upon development and implementation of the suggested accuracy improvements, Infrared Imaging appears to be potentially more effective than other traditional Thermal Imaging techniques, such as TLC (due to faster set-up, simpler and more economical operation, larger operating temperature range, as well as other factors outlined in this thesis).

The ability of IRT to determine exact locations of flow separation over a surface has been demonstrated. The technique could potentially be extended to various different test surfaces, and be useful in wing or vehicle body design.

Applications and limitations of IRT in turbine cooling visualisation have thus been identified and discussed. Recommendations for improvements, as well as areas for further work have been outlined.

6 Appendix

6.1 Calibration block preparation

i) A copper block was prepared (machined, cleaned and polished on all surfaces to a high surface smoothness) with length x width x thickness dimensions of 67mm x 67mm x 5mm

ii) One of the block faces was covered with a thin layer of black paint to enhance TLC visibility. *Hallcrest BB-G1 Sprayable Black Coating* was used. The block was placed at approximately 75 degrees to the horizontal for spraying

iii) A clean syringe was used to extract 2.5ml of water. The insertion orifice was upwards and air bubbles were gently pushed out

iv) A separate clean syringe was used to extract 2.5ml of black paint. Black paint is not transparent and more viscous than water, hence more care was taken to excrete the air slower while retaining paint

v) The combined 5ml mixture was inserted into a clean pot and gently swirled. Equal water-to-paint ratio ensured best quality spraying

vi) A clean syringe was used to insert the mixture into a compressed-air-powered spray paint gun

vii) The spraying rate was kept low to ensure the paint was applied in very thin layers (taking around 40 minutes to spray 5ml) and dried quickly. This eliminated formation of droplets and visible paint irregularities on the block surface

viii) The paint was applied in alternating directions (covering the surface completely in vertical lines, followed by horizontal, then diagonal, vertical again, etc.) to ensure even distribution across the block

ix) The block was allowed to dry for 2-3 hours after spraying.

The black-painted face was later covered with a thicker TLC layer. The spray gun was often clogged during TLC application by the crystal mixture (which is difficult to notice due to its transparency and colourlessness).

Farina *et al.*, 1994 [51], used a double filtration method for easier crystal application methods. The liquid TLC was mixed with a hand blender for 15minutes to break-up large lumps of raw microencapsulated TLC. It was then mixed with distilled water to dilute the mixture blended further with a magnetic mixer and spin bar for 25 minutes prior to filtration through a polyester filter. Filtration methods were not used in this study, but may be used to improve TLC application process in a future potential study.

x) Approximately 9ml of crystal mixture must was mixed with 9ml of water prior to spraying. Different crystals can be mixed together (e.g. 3ml of a 30℃ crystal, 3ml of a 35℃ crystal and 3ml of a 40℃ crystal must be mixed with 9ml of water)

xi) The spraying process took approximately 60-90 minutes and formed. The block was allowed to dry for 2-3 hours in darkness, as UV light is detrimental to the crystal colour displaying properties.

6.2 MATLAB Codes

6.2.1 Calibration Code

This MATLAB code produces an image, which uses a colour code to convey the numerical values of infrared intensity for each pixel of the raw image acquired by the infrared camera.

```
function calibration_code (~, ~)
%% ------------------insert appropriate data here-------------------------
% Specify the file folder location:
%filepath = 'H:\dos\My Work\Ilya Gribanov\Calibration\'; %for Windows
filepath = '/Users/ilyagribanov/Desktop/Calibration/'; %for Mac
% Specify the name of file series:
fileseries = 'Mesh 49'; % (preceeds _fileNum.raw)
% Specify the file number:
filenumber = '24';       %(follows after 'rootname_')
%--------------------------------------------------------------------------

%% This part of the m-file opens a selected .raw IRI file
% create file name out of its sub-components
filename = [filepath, fileseries, '_', filenumber, '.raw'];
% the image "height" has this number of pixels:
NUM_OF_COLS = 164;
% the image "width" has this number of pixels:
NUM_OF_ROWS = 129;
% open the file
fid = fopen(filename, 'r');
% check whether the file has adequate data and inform if not
fseek(fid,0,'eof');
if ftell(fid)~=NUM_OF_COLS*NUM_OF_ROWS*2
    disp('This .raw file contains insufficient data')
 %  continue
end
fseek(fid,0,'bof'); %return to the start of the file

% read-in data
    Data = fread(fid, [NUM_OF_COLS, NUM_OF_ROWS], 'uint16')';
    fclose(fid); % close the file
```

```
%% Image adjustment tools
Data = Data(:,1:end-5); %chops the landscape image

%% Resizing the image and applying Filters to reduce image noise:
%MedFiltData = medfilt2(Data);
%ResizedThenFilteredData = imresize(MedFiltData, 2);
%% Alternative filter that could be applied:
                %ResizedData = imresize(Data, 2);
                %FilteredThenResizedData = medfilt2(ResizedData);

%% Calculate mean centrepoint IRI (within 5x5 pixel square)
%note:
%x-axis pixel co-ordinates are 0:164
%y-axis pixel co-ordinates are 0:128
%take a 10x10 array (5x5 pixel square) and calculate mean IRI:
%take full block size and calculate standard deviation:
%input values below

%% ============== MANUALLY INPUT VALUES HERE ========================
%5x5 pixel square coordinate values:
%xm = 45; %xm = x-axis minimum
%xx = 55; %xx = x-axis maximum
%ym = 75; %ym = y-axis minimum
%yx = 85; %yx = y-axis maximum

% ====================================================================
%% ================= MANUALLY INPUT VALUES HERE ====================
%for standard deviation (entire block)
%EntireMedFiltData = MedFiltData(55:84, 60:89); %co-ordinates
%EntireMedFiltData = MedFiltData(Xm:Xx, Ym:Yx); %in this format
%pixel coordinate values are:

%Xm = 35; %Xm = x-axis minimum
%Xx = 65; %Xx = x-axis maximum
%Ym = 65; %Ym = y-axis minimum
%Yx = 95; %Yx = y-axis maximum
%====================================================================
```

```
%% ========== FOR COORDINATES WITHOUT FILTER=======================
%% ================== MANUALLY INPUT VALUES HERE====================
%5x5 pixel square coordinate values:
xm = 23; %xm = x-axis minimum
xx = 24; %xx = x-axis maximum
ym = 47; %ym = y-axis minimum
yx = 48; %yx = y-axis maximum

% ================================================================
%% ================== MANUALLY INPUT VALUES HERE====================
%for standard deviation (entire block)
%EntireMedFiltData = MedFiltData(55:84, 60:89); %co-ordinates
%EntireMedFiltData = MedFiltData(Xm:Xx, Ym:Yx); %in this format
%pixel coordinate values are:
Xm = 12; %Xm = x-axis minimum
Xx = 42; %Xx = x-axis maximum
Ym = 1; %Ym = y-axis minimum
Yx = 57; %Yx = y-axis maximum
%================================================================

%% Use the coordinate values to calculate and display mean IRI and S.D.
%CentralMedFiltData = MedFiltData(xm:xx, ym:yx);
%EntireMedFiltData = MedFiltData(Xm:Xx, Ym:Yx);
%CentralMean = mean(CentralMedFiltData(:));
%EntireSTD = std(EntireMedFiltData(:));

%% Mean IRI and S.D. without image filters:
%CentralMedFiltData = MedFiltData(xm:xx, ym:yx);
%EntireMedFiltData = MedFiltData(Xm:Xx, Ym:Yx);
%CentralMean = mean(CentralMedFiltData(:));
%EntireSTD = std(EntireMedFiltData(:));

%% display mean IRI and Standard Deviation of IR on screen:
whos Data
%CentralMean; %EntireSTD; %image_time, image_name, case_temperature

%% Produce the image:
figure('Position', [50 70 1200 650]) %sets constant figure dimensions
% Display image (scale min and max values are set in square brackets)
```

```
%with filters
%imagesc(ResizedThenFilteredData,[8080, 8140])
%without filters:
imagesc(Data,[8150, 8350])
axis('image') %include axis on the figure
%colorbar %display scale as a colour bar

%=========================================================================
%% ======== A CODE FOR AREA VERIFICATION PURPOSES ONLY ==============
%=========================================================================
% This code addition superimposes white lines onto the
% generated image in order to check the area which is covered for
% CentralMedFiltData and EntireMedFiltData calculations
hold on %hold the generated image
% This is for MiddleArray
% CentralMedFiltData = MedFiltData(xm:xx, ym:yx);
% CentralMedFiltData = MedFiltData(70:71, 92:93);

%% This part of the code plots a small square in the block centre
%spatial coordinate values conversion:
a = ((xm)*2)-2;
A = ((xx)*2);
b = ((ym)*2)-2;
B = ((yx)*2);
%OR input here:
% a =   %x-axis minimum
% A =   %x-axis maximum
% b =   %y-axis minimum
% B =   %y-axis maximum
% for 5x5 pixel array, plot the rectangle
%set the four rectangle corner coordinates:
p1 = [a, B];
p2 = [a, b];
p3 = [A, B];
p4 = [A, b];
%draw the four rectangle walls:
plot([p1(2),p2(2)],[p1(1),p2(1)], 'w', 'Linewidth', 1);
plot([p3(2),p4(2)],[p3(1),p4(1)], 'w', 'Linewidth', 1);
plot([p1(2),p3(2)],[p1(1),p3(1)], 'w', 'Linewidth', 1);
plot([p2(2),p4(2)],[p2(1),p4(1)], 'w', 'Linewidth', 1);
```

```
hold on %hold the generated image

%% This part of the code plots the white visual boarder over the block
%spatial coordinate values conversion:
c = ((Xm)*2)-2;
C = ((Xx)*2);
d = ((Ym)*2)-2;
D = ((Yx)*2);
%plot rectangle covering the entire copper block area:
%set the four rectangle corner coordinates:
P1 = [c, D];
P2 = [c, d];
P3 = [C, D];
P4 = [C, d];
%draw the four rectangle walls:
plot([P1(2),P2(2)],[P1(1),P2(1)], 'w', 'Linewidth', 1);
plot([P3(2),P4(2)],[P3(1),P4(1)], 'w', 'Linewidth', 1);
plot([P1(2),P3(2)],[P1(1),P3(1)], 'w', 'Linewidth', 1);
plot([P2(2),P4(2)],[P2(1),P4(1)], 'w', 'Linewidth', 1);
```

6.2.2 Temperature Plotting Code

This MATLAB code uses a value of IRI and camera case temperature in an algorithm in order to convert a raw infrared intensity image into a temperature distribution image.

```
function temperature_code (~, ~)
%% Used for producing temperature images
%% ------------------insert appropriate data here-------------------------
% Specify the file folder location:
%filepath = 'H:\dos\My Work\MeshLocation\-1d\';              % for Windows
filepath = '/Users/ilyagribanov/Desktop/MeshLocation/-1d/'; % for Mac
% Specify the name of file series:
fileseries = 'set 9 rev 2d from -20'; % (preceeds _fileNum.raw)
% Specify the file number:
filenumber = '4';       %(follows after 'rootname_')
%--------------------------------------------------------------------------
```

```
%% This part of the m-file opens a selected raw file
% create file name out of its sub-components
filename = [filepath, fileseries, '_', filenumber, '.raw'];
% the image "height" has this number of pixels:
NUM_OF_COLS = 164;
% the image "width" has this number of pixels:
NUM_OF_ROWS = 129;
%% Scan .csv file for file time and case temperature

fid_csv = fopen([filepath, fileseries, '.csv'], 'r');
%scan and read-in the time at which the sample is taken and its
%corresponding Camera Case Temperature and closes file:
M = textscan(fid_csv, '%s %s %f', 'Delimiter', ',');
fclose(fid_csv);
image_time = M{:,1};
image_name = M{:,2};
case_temperature = M{:,3}; % camera case temperature (deg C)

if exist (filename)==0
end

%=============================================================

% open the file
fid = fopen(filename, 'r');
% check whether the file has adequate data and inform if not
fseek(fid,0,'eof');
if ftell(fid)~=NUM_OF_COLS*NUM_OF_ROWS*2
    disp('This .raw file contains insufficient data')
 %  continue
end
fseek(fid,0,'bof'); %return to the start of the file

% read-in data
    Data = fread(fid, [NUM_OF_COLS, NUM_OF_ROWS], 'uint16')';
    fclose(fid); % close the file
```

```
%% Image adjustment and manipulation tools
Data = Data(:,1:end-5); %chops the landscape image

%% Resizing the image and applying filters to reduce image noise:

MedFilteredData = medfilt2(Data);
ResizedThenFilteredData = imresize(MedFilteredData, 2);

%% Applying filter and resizing the image to reduce noise:

                ResizedData = imresize(Data, 2);
                FilteredThenResizedData = medfilt2(ResizedData);

%% Converting IR intensity values into temperature (deg C)

[rows, columns] = size(FilteredThenResizedData);
temperatureImage = zeros(size(FilteredThenResizedData));

if (18.2 < case_temperature(str2num(filenumber)) < 21.2)
   for i = 1:1:columns
      column = i;
      for j = 1:1:rows
         row = j;

%% (Polyfit generated) 2nd degree polynomial approximation
% Tb                    = (sqrt((10 * IRI) - 73832.75 - 10*(-50)*(Tc -18.4)    )) - 75.5
%temperatureImage(row, column) = ( sqrt(  (10*(ResizedThenFilteredData(row,
column)))   - 73832.75 - 10*(-50)*(case_temperature(str2num(filenumber))-18.4)  ) ) -
75.5;

%temperatureImage(row, column) = (sqrt((10 *(ResizedThenFilteredData(row,
column))) - 73832.75 - 10*(-50)*((case_temperature(str2num(filenumber)))-18.4))) -
75.5;

 %% Old Algorithms:
%% Linear Approximation Algorithm with filter
```

```
temperatureImage(row, column) = (((ResizedThenFilteredData(row, column))/23.49)
+ (50/23.49)*((case_temperature(str2num(filenumber)))-18.4) - (7784/23.49));

%% Linear Approximation Algorithm without filters
%
% Tb                    =    IRI / mTb              + ((-mTc)/mTb)*Tc                    -
18.4  -  IRI[at Tb=0]/mTb
%temperatureImage(row, column) = (((Data(row, column))/23.49) +
(50/23.49)*((case_temperature(str2num(filenumber)))-18.4) - (7784/23.49));
 %% Least squares regression - OLS calibration algorithm (Eviews 7):

 %Tblock = (I)*0.043103 + (Tcamera)*1.267930 - 358.9872

 %temperatureImage(row, column) = (((ResizedThenFilteredData(row,
column))*0.043103) + ((case_temperature(str2num(filenumber)))*1.267930) -
358.9872);

%% Differential Algorithm - Trapezium Approximation
% Tb                    =    IRI / mTb              + ((-mTc)/mTb)*Tc                    -
18.4  -  IRI[at Tb=0]/mTb
          %Region III
%           if 8675 < Data(row, column) < 8950
%temperatureImage(row, column) = (((Data(row, column))/25) +
(50/25)*((case_temperature(str2num(filenumber)))-18.4) - (7784/25));
          %Region IIa
%           elseif 8501 < Data(row, column) < 8674
%temperatureImage(row, column) = (((Data(row, column))/23.49) +
(50/23.49)*((case_temperature(str2num(filenumber)))-18.4) - (7784/23.49));
          %Region IIb
%           elseif 8951 < Data(row, column) < 9150
%temperatureImage(row, column) = (((Data(row, column))/23.49) +
(50/23.49)*((case_temperature(str2num(filenumber)))-18.4) - (7784/23.49));
%           else % Region I
%              temperatureImage(row, column) = (((Data(row, column))/22) +
(50/22)*((case_temperature(str2num(filenumber)))-18.4) - (7784/22));
%           end
```

```
        end
    end
else % If case temperature is outside the calibration range - display the message:
    disp('Invalid Internal Camera Temperature')
    return;
end

%% Produce figure
figure('Position', [50 70 1200 650]) % set constant figure parameters

imagesc(temperatureImage,[10, 65]) %set colourbar boundaries 10 to 65 deg C
axis('image')
%colorbar() % display colorbar

%% Add title to the figure
%title(['Image Name=',num2str(fileseries),'File Number =',filenumber, 'Time =',
image_time(str2num(filenumber)), 'Case Temperature =',
num2str(case_temperature(str2num(filenumber)))])
title(['Image Name=',num2str(fileseries),'File Number =',filenumber, 'Time =',
image_time(str2num(filenumber)), 'Case Temperature =',
num2str(case_temperature(str2num(filenumber)))])

%% Calculate mean central temperature (within a 5x5 pixel square)
%note:
%x-axis pixel co-ordinates are 0:164
%y-axis pixel co-ordinates are 0:128
%take a 10x10 array (5x5 pixel square) and calculate mean IRI:
%% ========== MANUALLY INPUT VALUES HERE==============
%5x5 pixel square coordinate values:
xm = 45; %xm = x-axis minimum
xx = 55; %xx = x-axis maximum
ym = 75; %ym = y-axis minimum
yx = 85; %yx = y-axis maximum

% ============================================================
%% ==========FOR COORDINATES WITHOUT FILTERS ===========
%% ========== MANUALLY INPUT VALUES HERE ==============
```

```
%5x5 pixel square coordinate values:
%xm = 23; %xm = x-axis minimum
%xx = 24; %xx = x-axis maximum
%ym = 47; %ym = y-axis minimum
%yx = 48; %yx = y-axis maximum

%% Use the coordinate values to calculate and display mean temperature
%CentralMedFiltData = MedFiltData(xm:xx, ym:yx);
%CentralMean = mean(CentralMedFiltData(:));

%% Mean temperature without image filters:
%temperatureImage = Data(xm:xx, ym:yx);
%MeanTemperature = mean(temperatureImage(:));
temperatureImage = Data(xm:xx, ym:yx);
MeanTemperatureData = mean(temperatureImage(:));
%whos
MeanTemperatureData;

%% display mean temperature on screen:
%whos ResizedData %- displays details
%MeanTemperature %, image_time, image_name, case_temperature

%================================================================
%% ======== A CODE FOR AREA VERIFICATION PURPOSES ONLY ========
%================================================================
% This code addition superimposes white lines onto the
% generated image to visualise the area covered for
% mean temperature calculations
hold on %hold the generated image

%% This part of the code plots a small square in the block centre
%spatial coordinate values conversion:
a = ((xm)*2)-2;
A = ((xx)*2);
b = ((ym)*2)-2;
B = ((yx)*2);
%OR input here:
```

```
% a =   %x-axis minimum
% A =   %x-axis maximum
% b =   %y-axis minimum
% B =   %y-axis maximum
% for 5x5 pixel array, plot the rectangle
%set the four rectangle corner coordinates:
p1 = [a, B];
p2 = [a, b];
p3 = [A, B];
p4 = [A, b];
%draw the four rectangle walls:
plot([p1(2),p2(2)],[p1(1),p2(1)], 'w', 'Linewidth', 1);
plot([p3(2),p4(2)],[p3(1),p4(1)], 'w', 'Linewidth', 1);
plot([p1(2),p3(2)],[p1(1),p3(1)], 'w', 'Linewidth', 1);
plot([p2(2),p4(2)],[p2(1),p4(1)], 'w', 'Linewidth', 1);

end
```

6.2.3 Effectiveness Code

Converts a temperature distribution image into an effectiveness image.

```
function effectiveness_code(~, ~)
%% Used for producing adiabatic wall and gas effectiveness images
%% ------------------------------insert appropriate data here----------------------------------
Tm = 20.3; %mainstream temperature (deg C)
Tc = 40.8; %coolant gas temperature (deg C)

% Specify the file folder location:
filepath = '/Users/ilyagribanov/Desktop/MeshLocation/-1d/';
% Specify the name of file series:
fileseries = 'set 9 rev 2d from -20'; % (preceeds _fileNum.raw)
% Specify pump power scale setting:
setting = 9;
% Specify the file number:
filenumber = '4';       %(follows after 'rootname_')
```

```
%% Additionally please specify the following for figure plotting purposes
% Specify observed material - please type 'mesh', or 'cylinder':
material = 'mesh';
% If observing mesh - specify its (x/d) position, otherwise ignore:
position = '-1';

%% BR values (at 40deg and 20deg from cylinder SL) for a given pump setting
if setting == 10;
BR40 = '1.82';
BR20 = '2.92';
   elseif setting == 9.5;
   BR40 = '1.77';
   BR20 = '2.83';
   elseif setting == 9;
   BR40 = '1.71';
   BR20 = '2.70';
   elseif setting == 8.5;
   BR40 = '1.61';
   BR20 = '2.49';
   elseif setting == 8;
   BR40 = '1.53';
   BR20 = '2.32';
   elseif setting == 7.5;
   BR40 = '1.44';
   BR20 = '2.12';
   elseif setting == 7;
   BR40 = '1.37';
   BR20 = '1.98';
   elseif setting == 6.5;
   BR40 = '1.29';
   BR20 = '1.78';
   elseif setting == 6;
   BR40 = '1.23';
   BR20 = '1.64';
   elseif setting == 5.5;
   BR40 = '1.17';
   BR20 = '1.48';
```

```
    elseif setting == 5;
    BR40 = '1.13';
    BR20 = '1.39';
    elseif setting == 4.5;
    BR40 = '1.08';
    BR20 = '1.23';
    elseif setting == 4;
    BR40 = '1.05';
    BR20 = '1.15';
    elseif setting == 3.5;
    BR40 = '1.01';
    BR20 = '1.04';
    else display 'Invalid Pump Setting Entered';
end

%% This part of the m-file opens a selected raw file
% create file name out of its sub-components
filename = [filepath, fileseries, '_', filenumber, '.raw'];
% the image "height" has this number of pixels:
NUM_OF_COLS = 164;
% the image "width" has this number of pixels:
NUM_OF_ROWS = 129;

%% Scan the file series .csv file for time, name and camera case temperature,
representative of the specific raw file
fid_csv = fopen([filepath, fileseries, '.csv'], 'r');
%scan and read-in the time at which the sample is taken and its
%corresponding Camera Case Temperature and closes file:
M = textscan(fid_csv, '%s %s %f', 'Delimiter', ',');
fclose(fid_csv);
%image_time = M{:,1};
%image_name = M{:,2};
case_temperature = M{:,3}; % camera case temperature (deg C)

if exist (filename, 'file')==0;
end
```

```
%%=============================================================
% open the file
fid = fopen(filename, 'r');
% check whether the file has adequate data and inform if not
fseek(fid,0,'eof');
if ftell(fid)~=NUM_OF_COLS*NUM_OF_ROWS*2
   disp('This .raw file contains insufficient data')
 %  continue
end
fseek(fid,0,'bof'); %return to the start of the file
% read-in data
   Data = fread(fid, [NUM_OF_COLS, NUM_OF_ROWS], 'uint16')';
   fclose(fid); % close the file

%% Image adjustment and manipulation tools
% For x/d = -1 use:
Data = Data(32:end-69,20:end-45); %chop the image
% For x/d = 3 use:
%Data = imrotate(Data,180); %rotates clockwise by 180 deg
%Data = fliplr(Data); %mirror reflects about y-axis
%Data = Data(47:end-65,35:end-57);
% For x/d = 1 use:
%Data = Data(30:end-81,32:end-35); %chops mirror landscape image
%For x/d = 5 use:
%Data = Data(92:end-14,1:end-80);
%Data = Data(60:83,38:end-62); %chops the landscape image
%Data = imrotate(Data,180); %rotates clockwise by 180 deg
%Data = fliplr(Data); %mirror reflects about y-axis

%% Resizing the image and applying Filters to reduce image noise:
MedFilteredData = medfilt2(Data);
ResizedThenFilteredData = imresize(MedFilteredData, 2);

%% Alternative filter that could be applied:
                ResizedData = imresize(Data, 2);
                FilteredThenResizedData = medfilt2(ResizedData);
```

```
%% Converting IR intensity values into cooling effectiveness
[rows, columns] = size(FilteredThenResizedData);
effectivenessImage = zeros(size(ResizedThenFilteredData));
% check if the camera case temperature is within the calibration
% temperature range
% If case temperature is within the calibrated range - apply the algorithm
if (18.2 < case_temperature(str2double(filenumber)) < 21.2)
   for i = 1:1:columns
      column = i;
      for j = 1:1:rows
         row = j;

%% Second order polynomial approximation algorithm with filters
% effectiveness = ( Tm - Tb / Tm - Tc )
%effectivenessImage(row, column) = (Tm - (((ResizedThenFilteredData(row,
column))/9.091) + (19.35/9.091)*((case_temperature(str2double(filenumber)))-18.4) -
(8173.6/9.091)))/(Tm - Tc);

effectivenessImage(row, column) = (Tm - (((ResizedThenFilteredData(row,
column))/23.49) + (50/23.49)*((case_temperature(str2double(filenumber)))-18.4) -
(7784/23.49)))/(Tm - Tc);

%% Previous (less accurate approximation) algorithms
%% Linear Approximation Algorithm without filters
% Tb                    =    IRI / mTb              + ((-mTc)/mTb)*Tc                    -
18.4  -  IRI[at Tb=0]/mTb
%temperatureImage(row, column) = (((Data(row, column))/9.091) +
(19.35/9.091)*((case_temperature(str2num(filenumber)))-18.4) - (8173.6/9.091));
%% least squares regression without filters
%effectivenessImage(row, column) = (Tm - (((Data(row, column))*0.092893) +
((case_temperatures(str2num(filenumber)))*2.072446) - 788.1734))/(Tm - Tc);
%% least squares regression - OLS block calibration algorithm:
%Tblock = (I)*0.043103 + (Tcamera)*1.267930 - 358.9872
%temperatureImage(row, column) = (((ResizedThenFilteredData(row,
column))*0.043103) + ((case_temperatures(str2num(filenumber)))*1.267930) -
358.9872);
%effectivenessImage(row, column) = (Tm - (((ResizedThenFilteredData(row,
```

```
column))/23.49) + (50/23.49)*((case_temperature(str2num(filenumber)))-18.4) -
(7784/23.49)))/(Tm - Tc);
%% least squares regression - OLS mesh calibration algorithm:
%Tmesh = (I)*0.092893 + (Tcamera)*2.072446 - 788.1734
%temperatureImage(row, column) = (((ResizedThenFilteredData(row,
column))*0.092893) + ((case_temperatures(str2num(filenumber)))*2.072446) -
788.1734);
%effectivenessImage(row, column) = (Tm - (((ResizedThenFilteredData(row,
column))*0.092893) + ((case_temperatures(str2num(filenumber)))*2.072446) -
788.1734))/(Tm - Tc);


      end
   end
else % If case temperature is outside the calibration range - display the message:
   disp('Invalid Internal Camera Temperature')
   return;
end
%% Produce figure
figure('Position', [50 70 1200 650]) % set constant figure parameters
imagesc(effectivenessImage, [0, 1]); %set colourbar boundaries 0 to 1
axis('off', 'image') %remove axis
%colorbar %display colorbar

%% add a title to the produced figure
 if material == 'mesh';  % For mesh images
   if position == '-1'; % for x/d = -1
   title(['BR at -20∫ row = ', BR20,',        Mesh Location (x/d) = ', position, ',
Effectiveness'], 'FontSize', 24)
   else % For all other x/d mesh locations
   title(['BR at -40∫ row = ', BR40,',        Mesh Location (x/d) = ', position, ',
Effectiveness'], 'FontSize', 24)
   end
 else % For cylinder surface images
   title(['BR at -20∫ row = ', BR20, '      BR at -40∫ row = ', BR40,',      Effectiveness'],
'FontSize', 24)
 end
end
```

List of References

[1] D. Shukman, BBC news. (2013, June 14). *A350 marks new phase in aero-engines*. [Online]. Available: http://www.bbc.co.uk/news/science-environment-22889969

[2] R. Parker, Rolls-Royce plc. (2011, October). *Engine Technology: The key to reducing aviation's climate impact,* Royal Aeronautical Society. [Online]. Available: http://aerosociety.com/Assets/Docs/Events/668/668_Naresh_Kumar.pdf

[3] N.A. Cumpsty, *Jet propulsion*, Cambridge University Press, Cambridge, 2nd edn., 2003.

[4] S.M. Ragan. (2012, January 16). *Increasing resistance to creep deformation* [Online]. Available: http://blog.makezine.com/2012/01/16/single-crystal-superalloys/

[5] Rolls-Royce, *The Jet Engine*, Rolls-Royce plc., London, 5th edn., 2005.

[6] G.D. Lock, *Aircraft Propulsion*, University of Bath ME30218 Course, 2008

[7] C.M. Sangan, K. Zhou, K. Litherland, R. Lam and G.D. Lock, "Thermal imaging as flow visualization for gas-turbine film cooling", *J. Aerosp. Eng.*, vol. 225, no. 4, pp. 417-431, April 2011.

[8] D.G. Bogard and K.A. Thole, "Gas turbine film cooling". *J. Propul. Power,* vol. 22, no. 2, pp. 249-270, March-April 2006.

[9] H.I.H. Saravanamuttoo, G.F.C. Rogers, H. Cohen and P.V. Straznicky, *Gas Turbine Theory*, FT Prentice Hall: Pearson Education Ltd., Edinburgh. 6th edn., 2009.

[10] R. Holl, "*Means of cooling turbine blades by liquid jets*", U.S. Patent 2866313, December 30, 1958 [Online]. Available: http://www.google.co.uk/patents?hl=en&lr=&vid=USPAT2866313&id=vH5sAAAAEBAJ&oi=fnd&dq=Liquid+cooling+of+turbine+blades&printsec=abstract#v=onepage&q=Liquid%20cooling%20of%20turbine%20blades&f=false

[11] National Renewable Energy Laboratory (2009, November 11). *Modeling cooling technologies – jet impingement* [Online]. Available: http://www.nrel.gov/vehiclesandfuels/powerelectronics/thermal_mangement.html

[12] C.J.M. Lasance and R.E. Simons. (2005, November 1). *Advances in high-performance cooling for electronics* [Online]. Available: http://www.electronics-cooling.com/2005/11/advances-in-high-performance-cooling-for-electronics/

[13] M. Wilson. (2008, October 23). *Intel licensing laptop cooling systems based on jet engine tech* [Online]. Available:http://gizmodo.com/5067948/intel-licensing-laptop-cooling-systems-based-upon-jet-engine-tech?tag=jet-engine

[14] M.A. Ricklick, *Characterization of an inline row impingement channel for turbine blade cooling applications*, Doctoral Thesis, American University of Central Asia, 2009.

[15] C. Emmerson, J. Steinbarger and G. Meginnis, *"Cooled turbine blade and its manufacture"*, U.S. Patent 3810711, May 14, 1974 [Online]. Available: http://www.google.co.uk/patents?id=cVR9AAAAEBAJ&printsec=abstract&zoom=4#v=onepage&q&f=false

[16] R.J. Bratton and C.A. Andersson, *"Transpiration cooled ceramic blade for a gas turbine*", U.S. Patent 4311433, January 19, 1982 [Online]. Available: http://www.docstoc.com/docs/44621681/Transpiration-Cooled-Ceramic-Blade-For-A-Gas-Turbine---Patent-4311433

[17] C. Falcoz, B. Weigand and P. Ott, “Experimental investigations on showerhead cooling on a blunt body”. *Int J. Heat Mass Tran.,* vol. 49, no. 7-8, pp. 1287-1298, April 2006.

[18] R.J. Goldstein, E.R.G. Eckert and F. Burggraf, “Effects of hole geometry and density on three-dimensional film cooling”, *Int. J. Heat Mass Tran.*, vol. 17, no. 5, pp.595-607, May 1974.

[19] C.A. Coat and G.D. Lock, “Flow visualisation experiments for turbine film cooling”, *Aeronaut. J.*, vol. 108, no. 8, pp.403-409, August 2004.

[20] H. Reiss and A. Bölcs, “Experimental study of showerhead cooling on a cylinder comparing several configurations using cylindrical and shaped holes”, J. Turbomachinery, vol. 122, no. 1, pp. 161-169, January 2000.

[21] J.-C. Han, S. Dutta and S. Ekkad, *Gas Turbine Heat Transfer and Cooling Technology*, CRC Press, Boca Raton, FL, 2nd edn., 2013.

[22] D.J. Mee, P.T. Ireland and S. Bather, “Measurement of the temperature field downstream of simulated leading-edge film-cooling holes”. *Exp. Fluids*, vol. 27, no. 3, pp. 273-283, August 1999.

[23] B.A. Haven and M. Kurosaka, “Kidney and anti-kidney vortices in crossflow jets”, *J. Fluid Mech.*, vol. 352, no. 1, pp. 27-64, December 1997.

[24] P.T. Ireland, A.J. Neely, D.R.H. Gillespie and A.J. Robertson, “Turbulent heat transfer measurements using liquid crystals”. *Int. J. Heat Fluid Fl.,* vol. 20, no. 4, pp. 355-367, August 1999.

[25] P.T. Ireland and T.V. Jones, “Detailed measurements of heat transfer on and around a pedestal in fully developed passage flow”. *Proceedings of the 8th International Heat Transfer Conference,* vol. 3, pp. 975-980, August 1986.

[26] J.M. Cutbirth and D.G. Bogard, “Evaluation of pressure side film cooling with flow and thermal field measurements – part I: shoerhead effects”. *J. Turbomach.,* vol. 124, no. 4, pp. 670-677, October 2002.

[27] C.A. Martin and K.A. Thole, “A CFD benchmark study: leading edge flim-cooling with compound angle injection”. *International Gas Turbine & Aeroengine Congress & Exhibition,* Orlando, 2-5 June 1997.

[28] M.W. Cruse, U.M. Yuki and D.G. Bogard, “Investigation of various parametric influences on leading edge film cooling”. *International Gas Turbine & Aeroengine Congress & Exhibition,* Orlando, 2-5 June 1997.

[29] M.K. Harrington, M.A. McWaters, D.G. Bogard, C.A. Lemmon and K.A. Thole, “Full-coverage film cooling with short normal injection holes”. *J. Turbomach.,* vol. 123, no. 4, pp. 798-805, October 2001.

[30] M.L. Nathan, T.E. Dyson, D.G. Bogard and S.D. Bradshaw, “Adiabatic and overall effectiveness for the showerhead film cooling of a turbine vane”. *J. Turbomach.,* vol. 136, no. 3, 013005, March 2014.

[31] T.E. Dyson, D.G. Bogard, J.D. Piggush and A. Kohli, “Overall effectiveness for a film cooled turbine blade leading edge with varying hole pitch”. *J. Turbomach.*, vol. 135, no. 3, 031011, May 2013.

[32] J.E. Albert, D.G. Bogard and F. Cunha, “Adiabatic and overall effectiveness for a film cooled blade”. *Proceedings of ASME Turbo Expo 2004 Power for Land, Sea, and Air*, Vienna, Austria, June 14-17, 2004.

[33] A.B. Mehendale and J.C. Han, “Influence of high mainstream turbulence on leading edge film cooling heat transfer: effect of film hole spacing”. *Int. J. Heat Mass Tran.,* vol. 35, no. 10, pp. 2593-2604, October 1992.

[34] A.B. Mehendale and J.C. Han, “Reynolds number effect on leading edge film effectiveness and heat transfer coefficient”. *Int. J. Heat Mass Tran.,* vol. 36, no. 15, pp. 3723-3730, October 1993.

[35] S.-J. Li, S.-F. Yang and J.-C. Han, “Effect of coolant density on leading edge showerhead film cooling using the pressure sensitive paint measurement technique”. *J. Turbomach.,* vol. 136, no. 5, 051011, May 2014.

[36] J. Ahn, M.T. Schobeiri, J.-C. Han and H.-K. Moon, “Effect of rotation on leading edge region film cooling of a gas turbine blade with three rows of film cooling holes”. *Int. J. Heat Mass Tran.,* vol. 50, no. 1-2, pp. 15-25, January 2007.

[37] Y. Lu, D. Allison and S.V. Ekkad, “Turbine blade showerhead film cooling: influence of hole angle and shaping”. *Int. J. Heat Fluid Fl.,* vol. 28, no. 5, pp. 922-931, October 2007.

[38] C.L. Liu, H.R. Zhu, Z.W. Zhang and D.C. Xu, “Experimental investigation on the leading edge film cooling of cylindrical and laid-back holes with different hole pitches”. *Int. J. Heat Mass Tran.,* vol.55, no. 23-24, pp. 6832-6845, November 2012.

[39] A. Schulz, “Infrared thermography as applied to film cooling of gas turbine components”. *Meas. Sci. Technol.* vo. 11, no. 7, pp. 948-956, July 2000.

[40] C.H.N. Yuen and R.F. Martinez-Botas, “Film cooling characteristics of a single round hole at various streamwise angles in a crossflow: part I effectiveness”. *Int. J. Heat Mass Tran.*, vol. 46, no. 2, pp. 221-235, January 2003.

[41] C.H.N. Yuen and R.F. Martinez-Botas, “Film cooling characteristics of round holes at various streamwise angles in a crossflow: part I effectiveness”. *Int. J. Heat Mass Tran.*, vol. 48, no. 23-24, pp. 4995-5016, November 2005.

[42] J.M. Owen, K. Zhou, O.J. Pountney, M. Wilson and G.D. Lock, “Prediction of ingress through turbine rim seals. Part 1: Externally-induced ingress”, *J. Turbomach.,* vol. 134, no. 3, 031012, July 2011.

[43] J.M. Owen, “Theoretical modelling of hot gas ingestion through turbine rim seals”, *Propulsion and Power Research*, vol. 1, no. 1, pp. 1-11, December 2012.

[44] C.M. Sangan, O.J. Pountney, K. Zhou, M. Wilson, J.M. Owen and G.D. Lock, “Experimental measurements of ingestion through turbine rim seals. Part 1: Externally-induced ingress”. *J. Turbomach.*, vol. 135, no. 2, 021012, March 2013.

[45] U.P. Phadke and J.M. Owen, “Aerodynamic aspects of the sealing of gas-turbine rotor-stator systems. Part 1: The behaviour of simple shrouded rotating-disk systems in a quiescent environment”, *Int. J. Heat Fluid Fl.*, vol. 9, no. 2, pp. 98-105, June 1988.

[46] U.P. Phadke and J.M. Owen, “Aerodynamic aspects of the sealing of gas-turbine rotor-stator systems. Part 2: The performance of simple seals in a quasiaxisymmetric external flow”. Int. J. Heat Fluid Fl., vol. 9, no. 2, pp. 106-112, June 1988.

[47] C. Cao, J.W., Chew, P.R. Millington and S.I. Hogg, “Interaction of rim seal and annulus flows in an axial flow turbine”, *J. Eng. Gas Turb. Power*, vol. 126, no. 4, pp. 786-793, October 2004.

[48] M.R. Anderson and J.W. Baughn, “Hysteresis in liquid crystal thermography”, *J. Heat Trans.*, vol. 126, no. 3, pp. 339-346, June 2004.

[49] V.U. Kakade, G.D. Lock, M. Wilson, J.M. Owen and J.E. Mayhew, “Accurate heat transfer measurements using thermochromic liquid crystal. Part 1: Calibration and characteristics of crystals”, *Int. J. Heat Fluid Fl.*, vol. 30, no. 5, pp. 939-949, October 2009.

[50] J.L. Hay and D.K. Hollingsworth, “A Comparison of trichromic systems for use in the calibration of polymer-dispersed thermochromic liquid crystals”. *Exp. Therm. Fluid Sci.*, vol. 12, no. 1, pp. 1-12, January 1996.

[51] D.J. Farina, J.M. Hacker, R.J. Moffat and J.K. Eaton, “Illuminant invariant calibration of thermochromic liquid crystals”, *Exp. Therm. Fluid Sci.*, vol.9, no. 1, pp.1-12, July 1994.

[52] M.R. Anderson and J.W. Baughn, “Liquid-crystal thermography: illumination spectral effects. Part 1 – Experiments”, *J. Heat Transfer*, vol.127, no. 6, pp.581-587, June 2005.

[53] V.U. Kakade, G.D. Lock, M. Wilson, J.M. Owen and J.E. Mayhew, “Accurate heat transfer measurements using thermochromic liquid crystal. Part 2: Application to a rotating disc”, *Int. J. Heat Fluid Fl.,* vol. 30, no. 5, pp. 950-959, October 2009.

[54] J.W. Baughn, J.E. Mayhew, J.D. Wolf and M.R. Anderson, “Hysteresis of thermochromic liquid crystal temperature measurement based on hue”, *J. Heat Transfer*, vol. 121, no. 4, pp. 1067-1072, November 1999.

[55] M.R. Anderson and J.W. Baughn, “Liquid-crystal thermography: illumination spectral effects. Part 2 – Theory”, *J. Heat Transfer*, vol. 127, no.6, pp. 588-597, June 2005.

[56] A. Rogalski, “Infrared detectors: an overview*”, Infr. Phys.T.*, vol. 43, no. 3-5, pp. 187-210, June 2000.

[57] W. Herschel, “Experiments on the refrangibilty of the invisible rays of the Sun”, *Phil. Trans. R. Soc. Lond.*, vol. 90, no. 1, pp. 284-292, January 1800.

[58] R. Ambrosio, M. Moreno, J. Mireles, A. Torres, A. Kosarev and A. Heredia, “An overview of uncooled infrared sensors technology based on amorphous silicon and silicon germanium alloys”, *Phys. Status Solidi*, vol. 7, no. 3-4, pp. 1180-1183, February 2010.

[59] R.J. Boyle, C.M. Spuckler, B.L. Lucci and W.P. Camperchioli, “Infrared low-temperature turbine vane rough surface heat transfer measurements”, *J. Turbomach.*, vol. 123, no. 1, pp. 168-177, January 2001.

[60] T. Astarita, G. Cardone, G.M. Carlomango, C. Meola, “A survey on infrared thermography for convective heat transfer measurements”, *Opt. Laser T.*, vol. 32, no. 7-8, pp. 593-610, October 2000.

[61] M. Mori, L. Novak and M. Sekavcnik, “Measurements on rotating blades using IR thermography”, *Exp. Therm. Fluid Sci.*, vol. 32, no. 2, pp. 387-396, November 2007.

[62] G. Cardonne, A. Ianiro, G. dello Ioio and A. Passaro, “Temperature maps measurements on 3D surfaces with infrared thermography”, *Exp. Fluids*, vol.52, no. 2, pp. 375-385, February 2012.

[63] One Slide Photography. (2011). *Lens Distortion* [Online]. Available: http://oneslidephotography.com/what-are-good-camera-lenses-like/lens-distortion/

[64] J.S. Lee, “Digital image enhancement and noise filtering by use of local statistics”, *IEEE Trans. Pattern Anal. Mach. Intell.*, vol. PAMI-2, no. 2, pp. 165-168, March 1980.

[65] G.M. Carlomango, G. Cardone, C. Meola and T. Astarita, “Infrared thermography as a tool for thermal surface flow visualisation”, *J. Visual.*, vol. 1, no. 1, pp. 37-50, March 1998.

[66] P.C. Sweeney and J.F. Rhodes, “An infrared technique for evaluating turbine airfoil cooling designs”, *J. Turbomach.*, vol. 122, no. 1, pp. 170-177, January 2000.

[67] S.V. Ekkad, S. Ou, R.B. Rivir, “A transient infrared thermography method for simultaneous film cooling effectiveness and heat transfer coefficient measurements from a single test”, *J. Turbomach.*, vol. 126, no. 4, pp. 597-603, October 2004.

[68] G. Cardone, T. Astarita and G.M. Carlomagno, “Wall heat transfer in static and rotating 180d turn channels by quantitative infrared thermography”, *Rev. Gen. Therm.*, vol. 37, no. 8, pp. 644-652, September 1998.

[69] T. Astarita, G. Cardone and G.M. Carlomagno, “Infrared thermography: An optical method in heat transfer and fluid flow visualisation”, *Opt. Laser. Eng.*, vol. 44, no. 3-4, pp. 261-281, March-April 2006.

[70] L. De Luca, G.M. Carlomango and G. Buresti, “Boundary layer diagnostics by means of an infrared scanning radiometer”, *Exp. Fluids*, vol.9, no. 3, pp. 121-128, May 1990.

[71] U. Desideri, G. Rossi, A. Giovannozzi and P. Maggiorana, “High resolution infrared thermography for airfoils boundary layer inspection in passive mode”, *ASME Turbo Expo: Power for Land, Sea and Air*, vol. 2, pp. 579-583, Vienna, 14-17 June 2004.

[72] G. Caciolli, B. Facchini, A. Picchi and L. Tarchi, “Comparison between PSP and TLC steady state techniques for adiabatic effectiveness measurement on a multiperforated plate”. *Exp. Therm. Fluid Sci.,* vol. 48, pp. 122-133, July 2013.

[73] FLIR Systems Inc., *ThermoVision Micron/A10 Camera User's Guide (Version 130)* [Online]. Available: http://www.flir.com/uploadedFiles/CVS_Americas/Cores_and_Components_NEW/Products/Legacy_Products/Micron130.pdf [Accessed 4 February 2013]

[74] J.D. Anderson, *Fundamentals of Aerodynamics*, McGraw-Hill, Singapore, 4th edn., pp.278-279, 2007.